Experiments on nonlocal processes in NS devices

Inauguraldissertation

zur
Erlangung der Würde eines Doktors der Philosophie
vorgelegt der
Philosophisch-Naturwissenschaftlichen Fakultät
der Universität Basel

von

Andreas Kleine
aus Bremen (D)

UNI
BASEL

Basel, 2010

Genehmigt von der Philosophisch-Naturwissenschaftlichen Fakultät
auf Antrag von
Prof. Dr. C. Schönenberger
Prof. Dr. A. Morpurgo
Prof. Dr. H. von Löhneysen

Basel, den 15. September 2009

Prof. Dr. Eberhard Parlow
Dekan

To Vali

Contents

Introduction

The invention of the first transistor in 1947 was a milestone depicting the beginning of the information era. As the information technology evolved rapidly during the decades obeying Moore's law[1], the impact on the society grew steadily and thus the demand for faster, smaller and cheaper devices. As the average transistors in standard processors have a size below $40\,\mathrm{nm}$, a further miniaturization will come to a natural end once the atomic level is reached. Thus, new ways of information processing are needed. One approach is spintronics which uses in addition to the charge of the electrons also their spin and the associated magnetic moment for data processing. Another possible future building block of information technology is molecular electronics where it is tried to integrate molecular structures in electronic circuits, which could lead to further downsizing of electronic devices.

A completely new way of data processing represents quantum computing which does not use the classical bits 0 and 1, but quantum bits (qubits), a coherent superposition of both classical bits allowing a quantum computer to perform some tasks much faster than ordinary computers. As the name "quantum computer" suggests, it exploits quantum mechanical phenomena such as superposition or entanglement. The latter has no counterpart in the macroscopic world and involves, as Einstein said, a "spooky action at a distance" [2] between quantum states of different objects. If two objects have entangled quantum states, these objects cannot be fully described individually anymore. As entanglement involves a nonlocal correlation, these entangled objects can be spatially separated. An example of entanglement are two electrons in a spin singlet state. This spin-entanglement is naturally found in superconductors where two electrons with spin-up and spin-down form a so-called Cooper pair. It was proposed [3; 4] that it is possible to split these Cooper pairs and spatially separate them while retaining their spin entanglement. For these proposals one makes use of the spatial extent

---

[1]Moore [1] predicted in 1965 that the number of transistors implemented on an integrated circuit will double every two years.

of hundreds of nanometers of a Cooper pair. Nowadays the microfabrication techniques have developed such that it is feasible to implement two individual metal contacts within the spatial extent of a Cooper pair. In theory these contacts are necessary for the spatial separation of the entangled electrons after splitting the Cooper pair. It was proposed [3; 4; 5] that the fundamental mechanism for splitting and separating Cooper pairs is the nonlocal, coherent process crossed Andreev reflection (CAR). Experimentally only a few studies [6; 7; 8; 9; 10; 11] were performed showing that it is possible to obtain CAR in devices with at least two metal contacts separated only 100-200 nm in contact with a superconductor. However, these experiments show as well that there are also two other nonlocal processes present, namely elastic cotunneling and nonlocal charge imbalance, which do not split Cooper pairs and mostly mask CAR. It was theoretically predicted and experimentally shown that high transparent contacts to the superconductor lead to masking of CAR [7; 9; 12] and low transparent contacts only allow a dominant CAR process in certain energy ranges [8; 10]. For the development and realistic success of a solid-state entangler based on superconductors it is necessary to understand and control the properties of the competing nonlocal processes.

Thus, this thesis studies the dependence of CAR on the contact resistance. We will present a characteristic change in the dominance of the competing nonlocal processes depending on the contact resistance for which we will suggest a qualitative explanation. As low- and high-transparent devices have already been studied [7; 8; 9; 10; 11], we will focus on the intermediate transparency regime and find that a CAR domination is possible in the maximum energy range. Besides the contact dependence we also investigate the dependence of CAR on temperature and magnetic field. In a second part we study one of the processes masking CAR, namely nonlocal charge imbalance. As for CAR we examine its contact resistance dependence, but also the influence of applied magnetic fields and find that the classical theory on this non-equilibrium effect of superconductivity only partly holds for our measurements.

Chapter 1

Superconductivity

1.1 Superconductivity - an introduction

In the macroscopic phenomenon "superconductivity" the electrical resistance R vanishes below a critical temperature T_{C}. Besides perfect conductivity, a material in the superconducting state is also an ideal diamagnet below a critical applied magnetic field H_{C}[1], a fact commonly referred to as Meissner-Ochsenfeld effect [13]. It took nearly 40 years after the discovery of superconductivity in 1911 by Kammerlingh Onnes [14] until in 1950 Ginzburg and Landau proposed a phenomenological theory [15]. Some years later, in 1957, Bardeen, Cooper and Schrieffer (BCS) published their ground-breaking work on explaining superconductivity in a microscopic theory [16].

The Ginzburg-Landau (GL) theory is a phenomenological approach describing superconductivity as a second order phase transition. Ginzburg and Landau introduced the complex order parameter $\Psi(\mathbf{r})$ which makes it possible to describe how "deeply" a material is in the superconducting state while $n_s = |\Psi(\mathbf{r})|^2$ accounts for the local density of superconducting electrons. The strength of the GL theory is the easier applicability to spatially inhomogeneous systems like normal metal/superconductor interfaces compared to the BCS theory described below. In 1959 Gor'kov united both theories by showing that the GL theory can be extracted from the BCS theory for temperatures close to T_{C} [17].

The BCS theory is a microscopic description of superconductivity, in

---

[1] We restrict ourselves to Typ I superconductors.

which the conduction electrons condense into a macroscopic quantum mechanical many-body ground state similar to a Bose-Einstein condensate. This is possible because the ground state of a Fermi sea of electrons is unstable with respect to attractive interactions [18]. Such an interaction can occur, for example, if an electron passing through a solid deforms the lattice by attracting the positive ion cores leading to an accumulation of positive ion cores which themselves attract a second electron. The lattice deformation can de described by phonons. These two electrons are then coupled via an electron-phonon interaction. Superconductivity occurs if this attractive force is larger than the Coulomb repulsion between the two electrons. The two coupled electrons then form the so-called Cooper pair (CP), which has opposite spin ($\uparrow\downarrow$) and equal, but opposite momenta ($\mathbf{k}, -\mathbf{k}$). The spatial extent of the pair correlation exchanged via the lattice is given by the BCS coherence length $\xi_0 = \hbar v_F / \pi \Delta(0)$ with Fermi velocity v_F and the superconducting energy gap $\Delta(0)$ at $T = 0$, which can be thought of as the average size of a CP [19].

Within the BCS theory a temperature dependent energy gap $\Delta(T)$ can be deduced from the excitation spectrum of a superconductor exhibiting its largest value at $T = 0$. With rising temperature, the energy gap shrinks and vanishes at $T = T_C$. The energy gap $2\Delta(T)$ corresponds to the energy which is necessary to split up a Cooper pair and create two single quasiparticles in the superconductor. These quasiparticles exist above the gap as exited states. The size of the energy gap at $T = 0$ is related to T_C via $\Delta(0) = 1.764 k T_C$. Close to T_C the temperature dependence of the energy gap is [19]

$$\Delta(T) \approx 1.74 \Delta(0) \sqrt{1 - \frac{T}{T_C}}. \tag{1.1}$$

The transition from normal to superconducting state leads to a change of the density of states N as a direct consequence of the emergence of the energy gap. The superconducting density of states N_s for quasiparticles at energy E reads [20]

$$N_s(E) = \begin{cases} N_n(E_F) \cdot \dfrac{|E - E_F|}{\sqrt{(E - E_F)^2 - \Delta^2}} & \text{for } |E - E_F| \geq \Delta \\ 0 & \text{for } |E - E_F| \leq \Delta \end{cases} \tag{1.2}$$

where N_n is the normal metal density of states at $T > T_C$ and E_F the Fermi energy. It follows from eq. (1.2) that no single particle states exist in the energy interval $E_F \pm \Delta$, whereas N_s exhibits a singularity at the gap edges and reduces to N_n at larger energies, see Fig. 1.1(a). A powerful technique to examine N_s and Δ is superconducting tunneling spectroscopy described in the next chapter.

1.2 Superconducting tunneling spectroscopy

Superconducting tunneling spectroscopy (STS) was established by Giaver in 1960 [21] and is now a valuable method to examine properties of a superconductor [22], like the energy gap Δ and the density of states of the superconductor. STS involves tunneling of single quasiparticles from a normal metal (electrode) through a thin insulating layer (barrier) into a superconductor (electrode). Since the tunneling probability decreases exponentially with thickness and height of the barrier, STS gives the opportunity to gain information on the barrier and its quality, e.g. its homogeneity.

Single particle tunneling can be described by the tunneling hamiltonian [19]

$$H_T = \sum_{\sigma \mathbf{kq}} T_{\mathbf{kq}} c_{\mathbf{q}\sigma}^* c_{\mathbf{k}\sigma} + h.c. \,. \tag{1.3}$$

In eq. (1.3) the specific details of the tunneling barrier are included in the phenomenological tunneling matrix element $T_{\mathbf{kq}}$ with wavevectors $\mathbf{k}$ and $\mathbf{q}$ of the electrons of one of the electrodes. The tunneling process itself is described by the annihilator $c_{\mathbf{k}\sigma}$ which removes an electron with wavevector $\mathbf{k}$ and spin σ, and the creator $c_{\mathbf{q}\sigma}^*$ generating an electron with $\mathbf{q}$ on the other electrode.

Besides the tunneling probability given by $|T_{\mathbf{kq}}|^2$, the tunneling current is governed by the number of quasiparticles trying to tunnel and on the available states into which they can tunnel. This is accounted for by the density of states of both electrodes $N_{1,2}$ and their occupation given by the Fermi function $f(E)$. Multiplying this with the tunneling probability leads to the following expression for the tunneling current

$$I(U) = A \left| T_{\mathbf{kq}} \right|^2 \int_{-\infty}^{\infty} N_1(E) N_2(E + eU) \left[f(E) - f(E + eU) \right] dE \tag{1.4}$$

with A as a constant of proportionality [19].

In the case of a normal metal/insulator/normal metal (NIN) tunnel junction applying a voltage shifts the Fermi energy of the electrodes by eU with respect to each other, which results in a net tunneling current and a normal state conductance $G_{nn} \neq 0$. This current increases with bias since on the one hand more quasiparticles can participate in tunneling and on the other hand more empty states are available. Therefore, as long as the barrier is not affected by the bias, eq. (1.4) gives a linear current vs. bias (I-U) characteristic in NIN systems with $I(U) = U/R_\mathrm{T}$. R_T is called tunneling resistance and is proportional to $1/|T_{\mathbf{kq}}|^2$.

In superconducting tunneling spectroscopy one mostly deals with normal metal/insulator/superconductor (NIS) tunnel junctions which exhibit non-

linear I-U-characteristics. For an applied bias $|U| < \Delta/e$ and $T = 0$ no single particle tunneling is possible, because no available excitation states do exist in the superconductor ($N_s = 0$), see eq. (1.2). The characteristic strong increase of the tunneling current at $|U| = \Delta/e$ is due to the singularity in N_s and the resulting large number of unoccupied states, see Fig. 1.1(a). For $|U| >> \Delta/e$ the I-U-characteristic resembles the one of an NIN junction since N_s is similar to N_n in this energy range. With eq. (1.4) the bias dependence of the tunneling current of an NIS junction is described by

$$I(U) = A \left|T_{\mathbf{kq}}\right|^2 N_1(0) \int_{-\infty}^{\infty} N_{2s}(E) \left[f(E) - f(E + eU)\right] dE. \qquad (1.5)$$

When taking the derivative of eq. (1.5) with respect to the applied voltage, one gains the following expression for the differential conductance [19]

$$G_{ns} = \frac{dI_{ns}}{dU} = G_{nn} \int_{-\infty}^{\infty} \frac{N_{2s}(E)}{N_2(0)} \left[-\frac{\partial f(E + eU)}{\partial(eU)}\right] dE \qquad (1.6)$$

which directly gives N_s for $T = 0$. Temperature dependent STS measurements, as shown in Fig. 1.1(b), exhibit smeared features with increasing T, because the energy gap shrinks with T and even with an applied bias $|U| < \Delta/e$ some quasiparticles can tunnel due to thermal energy.
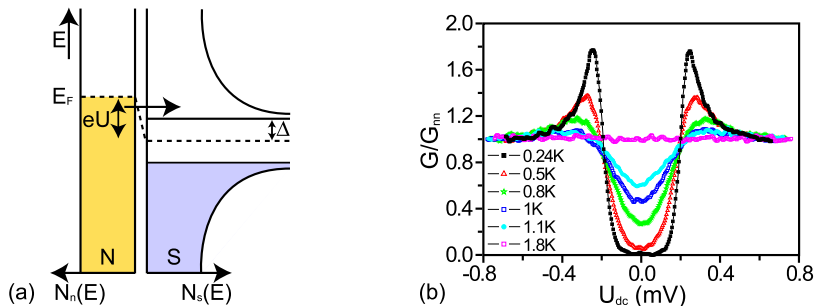
Figure 1.1: (a) Excitation schematic of an NIS tunnel junction with an applied bias U at $T = 0$. (b) Temperature dependent STS measurements of an Au(35 nm)/Ti(5 nm)/AlO$_x$/Al(25 nm tunnel junction normalized to the normal state conductance G_{nn}. As can be seen G/G_{nn} vs. bias resembles $N_s(E)$ of the superconductor at base temperature shown in (a), while increasing T leads to smeared features due to thermally excited tunneling quasiparticles.

Chapter 2

Transport at normal metal/superconductor interfaces

When a superconductor (S) and a normal metal (N) are in electrical contact and form an NS interface, a variety of different phenomena and transport processes can happen. In a device containing multiple NS interfaces, both local and nonlocal processes can occur which will be described in this chapter. We first will explain the local process Andreev reflection (AR) and introduce the model of Blonder, Tinkham and Klapwijk (BTK) describing the transport across an NS junction of arbitrary transparency. Subsequently, we discuss three competing nonlocal processes being of importance for the understanding of our measurements. We introduce crossed Andreev reflection (CAR), elastic cotunneling (EC) and nonlocal charge imbalance (CI).

2.1 Andreev reflection

To begin we consider a perfect single normal metal/superconductor (NS) interface with maximum transparency $t = 1$. If a potential is applied across the junction, the local process Andreev reflection (AR) describes the conversion of a dissipative current in N carried by single electrons into a dissipationless supercurrent in S carried by Cooper pairs. AR is only possible for bias potentials $|U| < \Delta/e$, making this process a local *subgap* transport mechanism. In the AR process two electrons in the normal metal pair and enter the superconductor as a Cooper pair (CP) while simultaneously retro-reflecting a hole, see Fig. 2.1(a).
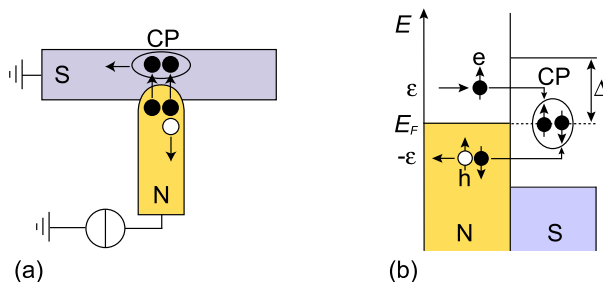
Figure 2.1: (a) Schematic of Andreev reflection in a normal metal/superconductor (NS) device. Two electrons (black circles) in N pair and form a Cooper pair (CP) in S, while simultaneously retro-reflecting a hole (white circle). (b) A detailed schematic of the subgap ($\epsilon < \Delta$) process Andreev reflection at an NS interface.

We can understand this process as follows: An electron from N impinging on S with an energy $\epsilon < \Delta$ (ϵ is the excitation energy relative to E_F) can only enter the superconductor as evanescent quasiparticle wave on a characteristic length scale of $\approx \hbar v_F/2\Delta$. This implies that the incident electron should be reflected at the NS interface as the superconducting energy gap denotes a potential barrier of height Δ. As the energy of the electron ($\approx E_F$) is typically much larger than Δ, the potential barrier and thus the force of the superconductor acting on the electron is too small to change its momentum significantly. Hence, the probability for normal reflection in the Andreev approximation ($\Delta, \epsilon << E_F$) is exceedingly small. As the electron with initial energy ϵ, momentum $\mathbf{k}$ and say spin up ($\uparrow$) cannot get reflected, it enters the superconductor by pairing with a second electron from N with energy $-\epsilon$, opposite momentum $-\mathbf{k}$ and spin down ($\downarrow$) to form a Cooper pair ($\mathbf{k}$,-$\mathbf{k}$;$\uparrow\downarrow$) and enter the superconductor. To conserve momentum a spin-up hole[1] with $\mathbf{k}$ is retro-reflected representing the missing spin down electron with $-\mathbf{k}$, see Fig. 2.1(b). For subgap energies AR is the only possible mechanism for charge transport across an NS interface.

As in AR two electrons enter the superconductor per electron impinging on the junction, the conductance of the NS interface G_{ns} for $|eU| < \Delta$ is twice the normal state conductance G_{nn}. This holds for an ideally transmitting interface. Lower transparent junctions, where electrons are reflected at a potential barrier, will be discussed below in the BTK model.

Inhomogeneous systems like NS junctions and the intimitally connected process of Andreev reflection are described by the Bogoliubov-de Gennes

---

[1]The hole has spin up as it is associated with a missing spin down electron [23].

(BdG) equations. They incorporate the spatially varying pair potential $\Delta(\mathbf{r})$ and the potential energy $U(\mathbf{r})$ which vary due to the proximity effect and impurities. The BdG equations are a set of coupled differential equations describing the superconducting excitation spectrum, namely the position dependent electron-like ($k > k_\text{F}$) and hole-like ($k < k_\text{F}$) quasiparticles $u(\mathbf{r})$ and $v(\mathbf{r})$ in terms of a two component wavefunction ($u(\mathbf{r})$,$v(\mathbf{r})$). The BdG equations read [24]

$$\begin{pmatrix} H_0 & \Delta(\mathbf{r}) \\ \Delta^*(\mathbf{r}) & -H_0^* \end{pmatrix} \begin{pmatrix} u(\mathbf{r}) \\ v(\mathbf{r}) \end{pmatrix} = \epsilon \begin{pmatrix} u(\mathbf{r}) \\ v(\mathbf{r}) \end{pmatrix} \tag{2.1}$$

with H_0 as single electron Hamiltonian. If the pairing potential $\Delta(\mathbf{r}) = 0$ (normal metal), then the BdG equations decouple and describe electrons and holes in a normal metal. For $\Delta(\mathbf{r}) \neq 0$ these equations describe that at an NS interface electron- and hole-like quasiparticles can enter the superconductor at subgap energies. Inside the superconductor these quasiparticle waves decay exponentially and get converted into a supercurrent on a characteristic length $\approx \hbar v_\text{F}/2\Delta$ [25; 26].

At an NS interface Cooper pairs from the superconductor can leak into the normal metal, a fact referred to as proximity effect. The BdG equations describe that the finite Cooper pair density n_s decays from the SN interface within the normal metal exponentially on a characteristic length $\sqrt{\hbar D/\epsilon}$ with D as diffusion constant of N [23]. However, the Cooper pair leakage into the normal metal also affects the superconductor. It reduces the superconducting order parameter Δ inside the superconductor and thus weakens the superconducting properties, commonly called inverse proximity effect. In experiments these proximity effects cause e.g. a change of T_C or an excitation spectrum in N.

That far we have discussed NS interfaces with transparency $t = 1$. By implementing a very thin insulator (I) in between N and S, a NIS junction, the transparency decreases. As AR is a second order process in transmission, AR and therefore the electron tunneling probability decreases with reduced transparency. The BdG equations are the starting point for the very successful Blonder-Tinkham-Klapwijk (BTK) model [26] which describes the I-U-characteristics of NIS junctions with arbitrary interface transparencies. In the context of a generalized AR model, the interface scattering is represented by a repulsive δ-function potential of strength Z. By using the BdG equations and matching the wavefunctions at the interface, the BTK model predicts probabilities of the different subgap processes namely AR, quasiparticle transmission or ordinary reflection [26]. Finally, the model allows the calculation of the I-U-characteristic and the normalized differential conductance G_{ns}/G_{nn} vs. bias for arbitrary barrier strengths Z, respectively.
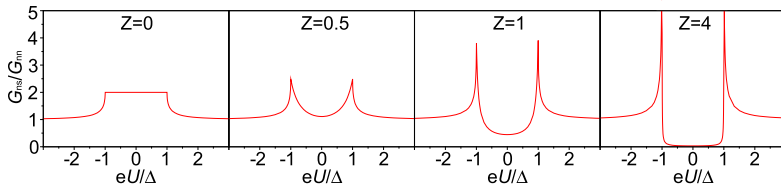
Figure 2.2: Normalized differential conductance as a function of bias energy for different barrier strengths Z of a NIS interface at $T = 0\,\mathrm{K}$. We calculated these curves on the basis of the BTK model [26].

The latter is shown in Fig. 2.2 for different values of Z at $T = 0$. The barrier strength Z indicates the electron tunneling probability and gives the normal state transmission coefficient t with $t = (1 + Z^2)^{-1}$. In the case of a metallic contact ($Z = 0$ and $t = 1$), all incident electrons are transferred across the junction due to AR, leading to an enhanced interface conductance $G_{ns} = 2G_{nn}$ in the subgap regime, see Fig. 2.2. With increasing Z, the transparency and the AR probability decrease, whereas ordinary reflection increases leading to a reduced G_{ns}. As $T = 0$, quasiparticle transmission does not occur for subgap energies. In Fig. 2.2 $Z = 4$ ($t = 0.06$) already denotes a strong tunnel contact with $G_{ns}/G_{nn} \approx 0$ inside the energy gap. A tunnel contact with $Z = \infty$ and $t = 0$ is the extreme case where AR is completely suppressed with $G_{ns} = 0$ inside the energy gap. The BTK model and Fig. 2.2 clearly show that the differential subgap conductance decreases with increasing Z.

2.2 Crossed Andreev reflection and elastic cotunneling

In the last chapter we introduced Andreev reflection, a mechanism describing subgap transport at a single NS junction. Furthermore, we know now that at subgap energies evanescent electron- and hole-like wavefunctions $\Psi(x)$ exist inside the superconductor. Thus, theory proposed that a quasiparticle entering the superconductor at subgap energies from a normal metal electrode N1 can interact coherently with a second, spatially separated normal metal electrode N2. A typical sample geometry is shown in Fig. 2.3. This is only possible if the distance d between N1 and N2 is such that there still exists a finite amplitude of the incident quasiparticle wavefunction at N2, see Fig. 2.3. For a clean 3D BCS superconductor the characteristic length is given by the BCS coherence length ξ_0, whereas for superconductors in the
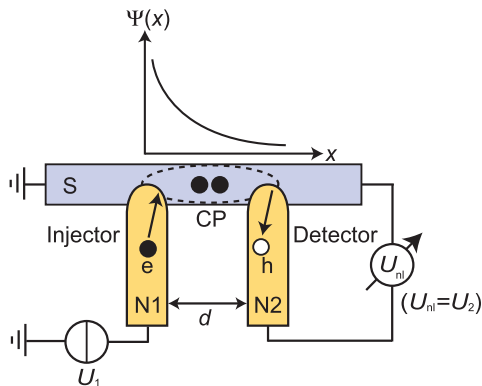
Figure 2.3: A sample and measurement schematics is shown with a crossed Andreev reflection process. An electron (e) enters from the injector the superconductor (S) by pairing with an electron from the detector to form a Cooper pair (CP) in S. To conserve momentum a hole (h) is reflected into the detector, thus causing a nonlocal voltage U_{nl}. For CAR (EC) to happen the amplitude of the quasiparticle wavefunction $\Psi(x)$ needs to be finite at the detector.

dirty limit $\xi \cong \sqrt{\ell_{\mathrm{el}}\xi_0}$ holds with ℓ_{el} as elastic mean free path.

If d is of the order of ξ, two possible processes can occur, namely elastic cotunneling (EC) and crossed Andreev reflection (CAR) with a probability proportional to $e^{-d/\xi}$. In case of EC, the incident electron tunnels elastically over a virtual state from N1 into N2, see Fig. 2.4(b). However, CAR is very similar to AR: If at subgap energies a spin up ($\uparrow$) electron[2] from N1 with momentum $\mathbf{k}$ tries to enter the superconductor, it forms a Cooper pair $(\mathbf{k}, -\mathbf{k}; \uparrow\downarrow)$ with an electron of opposite momentum and spin $(-\mathbf{k}, \downarrow)$, from the second, spatially separated normal metal electrode N2. As in AR a spin up ($\uparrow$) hole with momentum $\mathbf{k}$ is reflected to conserve momentum. In contrast to AR, this hole is reflected in N2. AR, CAR and EC are second order processes since all of them incorporate two coherent tunneling events.

In single NS junctions AR is the only transport process through the interface at subgap energies. In a multi-terminal NS device CAR and EC open new conduction channels. If we consider a two-terminal device with N1 and N2 as shown in Fig. 2.3, the current I_1 (I_2) through junction 1 (2) depends

---

[2]CAR is not limited to incident spin up electrons. For an incident spin down electron the spins of the other participating particles need to be reversed.
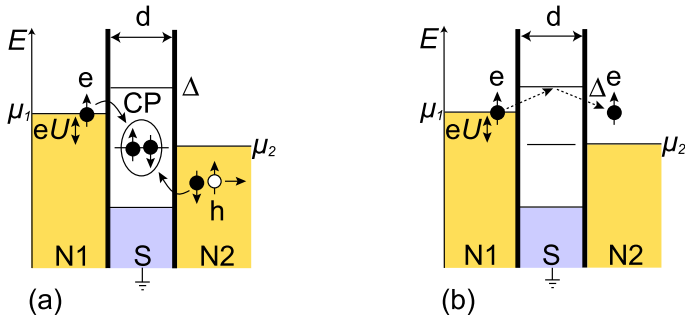
Figure 2.4: Schematics representing the nonlocal process (a) crossed Andreev reflection and (b) elastic cotunneling. Both second order processes only happen if d is of the order of ξ.

also on voltage $U_2{}^3$ (U_1) applied on N2 (N1) due to EC and CAR, making them nonlocal processes. Assuming linear transport one can write

$$\begin{pmatrix} I_1 \\ I_2 \end{pmatrix} = \begin{pmatrix} G_{11} & G_{12} \\ G_{21} & G_{22} \end{pmatrix} \begin{pmatrix} U_1 \\ U_2 \end{pmatrix}. \tag{2.2}$$

In a more detailed description the possible transport mechanisms are assigned to the different conduction elements G_{ij} in the tunneling limit and for clean superconductors [27]. To the local conductances G_{11} and G_{22} all three processes AR, CAR and EC contribute, whereas the nonlocal conductances G_{12} and G_{21} only depend on the nonlocal processes CAR and EC. These two processes tend to cancel each other, because with an applied voltage U_1 CAR and EC create particles of opposite charge in the detector, see Fig. 2.4, and therefore nonlocal bias potentials U_{nl} (U_2) of opposite sign. This is the reason for opposite contributions to the nonlocal conductance elements G_{ij} ($i \neq j$). Thus, on the basis of [27] eq. (2.2) can be written in the following form

$$\begin{pmatrix} I_1 \\ I_2 \end{pmatrix} = \begin{pmatrix} G_{\mathrm{AR,N1}} + G_{\mathrm{CAR}} + G_{\mathrm{EC}} & G_{\mathrm{CAR}} - G_{\mathrm{EC}} \\ G_{\mathrm{CAR}} - G_{\mathrm{EC}} & G_{\mathrm{AR,N2}} + G_{\mathrm{CAR}} + G_{\mathrm{EC}} \end{pmatrix} \begin{pmatrix} U_1 \\ U_2 \end{pmatrix}. \tag{2.3}$$

For an NIS junction in the tunneling limit and at low T and bias, theory predicts to lowest order in the tunneling rates that $G_{\mathrm{CAR}} = G_{\mathrm{EC}}$. Thus the off-diagonal (nonlocal) elements of eq. (2.3) vanish leaving only a CAR

---

^{3}In Fig. 2.3 U_2 is depicted as the nonlocal voltage U_{nl}.

and EC contribution to the local conductance as long as $d \leq \xi$. The spatial decay of G_{CAR} and G_{EC} is $\propto (k_F d)^{-2} e^{-2d/\pi\xi_0}$ [27].

2.2.1 Crossed Andreev reflection - application and modification

As was discussed in the previous chapter, perturbation theory predicts for NIS junctions in the tunneling limit and lowest order transmission an exact cancellation of the CAR and EC contribution to the nonlocal process $(G_{\mathrm{CAR}} = G_{\mathrm{EC}})$ [27]. This is an undesired result since the goal for applications is a dominance of CAR over EC (with $G_{\mathrm{CAR}} > G_{\mathrm{EC}}$). Why is a dominant CAR process so valuable?

For the development of quantum information technology the electron spin is a possible candidate for the realization of quantum bits in a solid state environment [28]. In this context the creation of spatially separated, entangled electron spins is important [29; 30], which was already successfully tested in quantum optics for entangled, spatially separated photons [31].

The two electrons of Cooper pairs in s-wave superconductors naturally form entangled spin singlet states with representation $|S\rangle = \frac{1}{\sqrt{2}} (|{\uparrow}{\downarrow}\rangle - |{\downarrow}{\uparrow}\rangle)$. It was theoretically proposed that it is possible to split a Cooper pair and spatially separate the electron spins [3; 4]. As long as the electron spins preserve their nonlocal correlation (entanglement), this state is inseparable, which means that it cannot be represented by a product of the single particle states. The inverse process of CAR was proposed as the basis for such a solid-state entangler with the superconductor acting as a source of spin-entangled electrons. In an inverse CAR process the Cooper pairs from S split between the two N leads while retaining their spin-entanglement.

Since the nonlocal correlation is destroyed easily by the strongly interacting solid-state environment, it is necessary to probe the entanglement. Noise measurements promise to be a solution because entangled spin-1/2 particles exhibit "bunching" behavior and a specific, unique noise power enhancement [29].

A solid-state entangler must fulfill certain requirements for application. The amount of spatially separated, entangled electrons injected into the leads should be considerably larger than the injected number of uncorrelated ones e.g. quasiparticles. Furthermore the entangled electron pairs should be individually addressable. The time $\hbar/\Delta$ between two electrons of one Cooper pair should be much smaller than the time $2e/I_{\mathrm{inj}}$ between subsequent Cooper pairs. Making use for example of Coulomb interaction is theoretically a feasible way to fulfill the requirements. Either by including quantum dots in-between S and N [4] or by generally having a high resistive environment [32], which leads to dynamical Coulomb blockade discussed in

chapter 3, it is energetically unfavorable for the electrons of a Cooper pair to enter the same lead (ordinary Andreev reflection) as they have to pay charging energy. As this is not the case for a CAR process with spatially separated electrons, Cooper pair splitting into different leads is favored.

CAR is a possible candidate for the realization of a solid state entangler and thus important for the development of quantum computing, quantum cryptography and quantum teleportation [33; 34]. Hence, it is necessary to lift the predicted balance between CAR and EC. What parameters influence this balance?

Recently, a large number of theories were published modeling these non-local processes in hybrid systems [5; 12; 27; 35; 36; 37; 38; 39; 40; 41; 42; 43; 44; 45]. By including higher order tunneling terms, electron-electron inter-actions or disorder, the cancellation between CAR and EC can be lifted. A general tendency in these models is that in NSN junctions (e.g. like the one of Fig. 2.3) EC dominates over CAR. However, two theories suggest that an external AC signal or the electromagnetic environment can lead to a situation where CAR is dominant [46; 47]. The latter is based on a model in which the two normal metal contacts are electromagnetically coupled. This coupling can favor CAR over EC, depending on the symmetry of the coupling [47]. This model contains dynamical Coulomb blockade, which will be discussed in chapter 3 and used for the interpretation of one part of the experimental results in this thesis.

It was proposed that the balance between EC and CAR can be lifted by using ferromagnets (F) with spin polarization P as electrodes instead of normal metals, as both processes are spin sensitive in a way that the relative alignment of the ferromagnetic electrodes decides which process is favored [5; 27; 42]. In the ideal case of full spin polarization of the contacts ($P = 1$), CAR is totally suppressed for parallel alignment. Since no electrons of opposite spin are available, an incident electron cannot pair with a second electron of opposite spin to form a CP, thus $G_{\mathrm{CAR}} = 0$. An antiparallel magnetization favors CAR and suppresses EC ($G_{\mathrm{EC}} = 0$), because of no available states for a tunneling electron, excluding possible spin flip processes. Nevertheless, the use ferromagnetic electrodes would also destroy the entanglement.

As the nonlocal signals of CAR and EC are very small and decay in a clean 3D BCS superconductor as $(k_F d)^{-2} e^{-2d/\pi\xi_0}$ [27], one can try to maximize the signal by optimizing geometry, dimensions and texture of the superconductor. By minimizing the contact distance d and increasing ξ with an improved evaporation process, the decay length is increased. Since in our samples $d < \xi$, the exponential factor $e^{-2d/\pi\xi_0}$ is not the limiting contribution for us, but the algebraic prefactor $(k_F d)^{-2}$. This prefactor reduces the nonlocal signal roughly by a factor of 10^4 since d is of the

order of 100 nm and the Fermi wavelength measures some Ångström. An improvement can be achieved by considering diffusive superconductors in the dirty limit ($\ell_{\mathrm{el}} < \xi_0$). In a 3D diffusive superconductor the prefactor changes to $(k_F d)^{-1}(k_F \ell_{\mathrm{el}})^{-1}$, which considerably enlarges G_{CAR} and G_{EC}[4] [44]. Reducing the dimensions of the superconductor[5] leads to a further reduction of the prefactor.

2.3 Charge imbalance

That far only crossed Andreev reflection and elastic cotunneling have been introduced as relevant for nonlocal charge transport at subgap energies in NSN and NISIN hybrid devices. Nonlocal charge imbalance is a third process, which can cause a measureable nonlocal voltage U_{nl} at the detector. It is important to discuss charge imbalance (CI) as we need to distinguish CAR, EC and CI in nonlocal transport measurements.

In the first part of this chapter we introduce local CI in a superconductor, whereas in the second part we derive a distance-dependent expression for the nonlocal resistance caused by CI, being necessary for the interpretation of results shown later in this thesis. In this derivation we mainly follow Tinkham [19], who describes "local" CI, whereas we extend Tinkham's approach to nonlocal CI.

Charge imbalance is a well-known non-equilibrium phenomenon of superconductivity studied extensively in the 1970s and 80s. It describes the spatial decay of quasiparticles (QP) within a superconductor and their decay with temperature. CI appears when the electron population of a superconductor is driven out of thermal equilibrium. In thermal equilibrium and $T = 0$ no quasiparticles and therefore no CI exists. However, CI can be generated e.g. by electron tunneling into a superconductor. This is not only possible for applied biases larger than Δ, but also for subgap biases at $T \neq 0$. A thermally smeared Fermi function and a thermally reduced superconducting energy gap allows electron tunneling at subgap energies, see Fig. 2.5(a). With increasing T this effect, and therefore CI, is more pronounced. The generation of QP is balanced by their diffusion and relaxation within S, which allows CI to be described by a steady-state dynamic equilibrium.

The first step for an understanding of CI is to describe the amount of quasiparticles being driven out of thermal equilibrium in a condensate of Cooper pairs (CP). A single particle excitation has an energy $E_k = (\Delta^2 + \xi_k^2)^{\frac{1}{2}}$ with Δ the BCS gap and ξ_k the one-electron energy of state k relative to

---

[4]Note that in the diffusive case not the BCS coherence length ξ_0, but the coherence length $\xi = \sqrt{\xi_0 \ell_{\mathrm{el}}}$ is the characteristic length scale.

[5]One dimension of the superconductor must be smaller than ℓ_{el}.
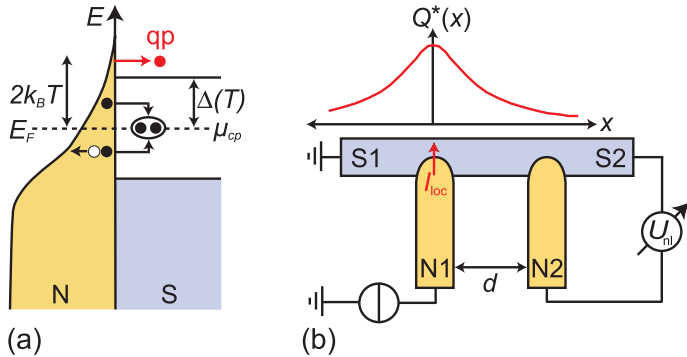
Figure 2.5: Schematics on charge imbalance (CI). (a) Current injection from a normal metal (N) into the superconductor (S). Due to thermal smearing of the Fermi function and a thermal reduction of the superconducting gap $\Delta(T)$ quasiparticles (qp) can enter S above $\Delta(T)$ and cause CI. Andreev reflection occurs at subgap energies that does not contribute to CI. (b) Schematic of the spatial decay of the effective charge $Q^*(x)$. At the injector N1 a current I_{loc} gets injected into S causing Q^*. These quasiparticles diffuse along S while decaying on a length scale of the CI length Λ^* causing a nonlocal voltage U_{nl} at the detector N2.

the Fermi energy E_F in the normal state. These excitations can be electron-like $(k > k_\mathrm{F})$ and hole-like $(k < k_\mathrm{F})$ with effective charge $q_k = \xi_k/E_k$. This charge changes continuously with k. Far inside the Fermi sphere the excitations are hole-like with effective charge $q_k \approx -1$ and $q_k \approx 0$ close to the Fermi surface. Far outside the Fermi sphere the excitations are electron-like with $q_k \approx +1$. In thermal equilibrium the occupation probability of single-particle excitations is given by the Fermi distribution function f_0. Out of equilibrium the Fermi function needs to be replaced by a function f_k. An expression for the QP disequilibrium is then given by

$$\delta f_k \equiv f_k - f_0(E_k/k_\mathrm{B}T). \tag{2.4}$$

One can distinguish between energy-mode and charge-mode disequilibrium. In the first case, also referred to as "even" or "longitudinal mode" [48], there exists an equal amount of hole-like and electron-like excitations in the QP spectrum, see Fig. 2.6(a). The even mode is mostly excited by phonons or photons which are charge neutral. A result of this type of disequilibrium is a reduction of Δ. To describe this reduction and therefore the strength of the even mode disequilibrium, an effective QP temperature T^*

is introduced[6].

For the results of this thesis, the second "charge-mode" disequilibrium is relevant, also known as "branch imbalance" and "odd" or "transverse mode" [48]. Therefore we focus on this part for the rest of the chapter. In the odd mode charged excitations from tunneling electrons or current conversion at NS interfaces lead to an inequality between hole- and electron-like excitations, see Fig. 2.6(b). This branch imbalance results in an effective charge Q^* inside the superconductor denoted by

$$Q^* = \sum q_k \delta f_k. \tag{2.5}$$

To maintain charge neutrality in the superconductor, the number of electrons in the BCS ground state is changed in this process. Consequently, the electrochemical potential of the Cooper pairs $\mu_{\rm cp}$ and the one of the quasiparticles $\mu_{\rm qp}$ are shifted in opposite directions relative to their equilibrium value $E_{\rm F}^0$, see Fig. 2.6(c). This shift in $\mu_{\rm qp}$ allows to measure a potential within the superconductor with a normal metal detector electrode coupled to the superconductor at a distance given by the charge imbalance length, the decay length of CI [9; 49; 50]. In contrast, by using a superconductor as detector electrode one probes $\mu_{\rm cp}$ of the Cooper pairs. The aim of this chapter is to find an expression for the potential $U(x)$ that can be measured at a second normal metal detector electrode 2 depending on the number of injected QP and the distance x to the QP injector.

First, we only consider one NS junction and discuss the generation of QP at the injector. The charge imbalance Q^* can be generated by the injection of quasiparticles from the normal contact 1 (injector) into S. Depending on temperature and bias voltage, the total injected and measured current $I_{\rm tot,1}$ at contact 1 consists of the injected quasiparticles $I_{Q^*,1}$ and the subgap current due to Andreev reflection $I_{\rm AR,1}$, $I_{\rm tot,1} = I_{Q^*,1} + I_{\rm AR,1}$, see Fig. 2.5(a). At $T = 0$ and $|eU| < \Delta$, $I_{\rm tot,1}$ is only driven by Andreev reflection processes as discussed in chapter 2.1. For biases above Δ/e, only quasiparticle injection is possible leading to $I_{\rm tot,1} = I_{Q^*,1}$ at $T = 0$. For subgap energies $|eU| < \Delta$ and $T \neq 0$ the total injected current $I_{\rm tot,1}$ consists of both, $I_{Q^*,1}$ and $I_{\rm AR,1}$, see Fig. 2.5(a). $I_{Q^*,1}$ is possible for subgap energies due to thermal smearing of the Fermi function. As the Andreev processes do not contribute to Q^*, it is necessary to define $F^* = I_{Q^*,1}/I_{\rm tot,1}$ giving the fraction of the total current causing charge imbalance[7]. Thus, the charge injection rate $\dot{Q}^*(0)$ at contact 1 and the injection current $I_{\rm tot,1}$ per unit volume Ω are related as

---

[6]T^* is not a thermodynamic temperature.

[7]The ratio F^* can range from zero for $eU = \Delta$ to unity for eU or $k_{\rm B}T >> \Delta$. For $eU = \Delta$ the full electronic charge contributes to the electrical current and not to Q^*. This changes for higher bias voltages or temperatures.
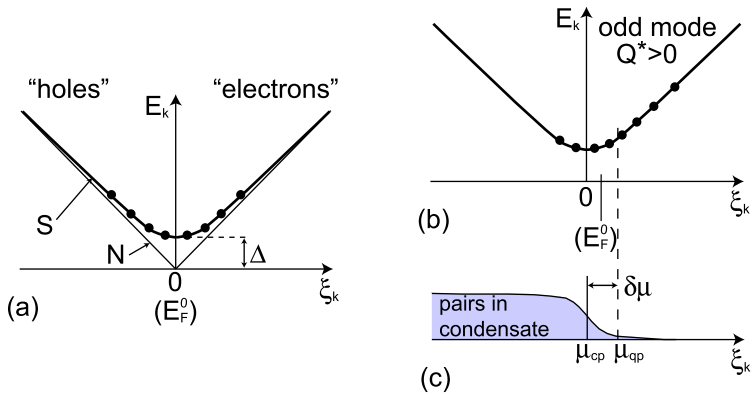
Figure 2.6: (a) Dispersion curves of single-particle excitations in thermal equilibrium in the normal (N) and superconducting (S) state. Indicated as black dots is the occupation of electron- and hole-like excitations. (b) Schematics of the occupation of single-particle excitations in the odd mode for $Q^* > 0$. (c) Shift of the Cooper pair and quasiparticle chemical potential μ_{cp} and μ_{qp} relative to the equilibrium Fermi energy E_{F}^0 in the case of branch imbalance [19].

follows

$$e\dot{Q}^*(0) = \frac{F^* I_{\mathrm{tot},1}}{\Omega}. \qquad (2.6)$$

In thermal equilibrium the amount of injected charge $Q^*(0)$ is given by the relaxation time τ_{Q^*} describing how fast the excitations decay into the Cooper pair (CP) condensate by inelastic energy relaxation processes like electron-phonon scattering. In steady state $\dot{Q}^*(0) = Q^*(0)/\tau_{Q^*}$ holds and one finds with eq. (2.6) the following expression for the total injected charge at x=0

$$Q^*(0) = \frac{\tau_{Q^*} F^* I_{\mathrm{tot},1}}{e\Omega}. \qquad (2.7)$$

Note that in the following we do not focus on I_{Q^*}, but on $I_{\mathrm{tot},1}$, as this is the experimentally determined quantity.

CI is distance dependent, because the injected quasiparticles $Q^*(0)$ at contact 1 diffuse away while relaxing into the CP condensate. With the assumption that S is quasi-1-dimensional and that the non-equilibrium population relaxes symmetrically around the injection point, CI decays in space as [19]

$$Q^*(x) = Q^*(0) e^{-\frac{|x|}{\Lambda_{Q^*}}} \qquad (2.8)$$

with the charge imbalance length $\Lambda_{Q^*} = \sqrt{D\tau_{Q^*}}$ as the characteristic diffusion length for a relaxation time τ_{Q^*} and a quasiparticle diffusion constant D, see Fig. 2.5(b).

As yet we have discussed the Q^* generation and its spatial decay within S. We now add a second normal metal electrode N2 as detector in distance x from the injector in order to measure the potential $U_2(x)$ caused by the excitations in S. In order to respect the boundary conditions of an ideal voltage measurement, no current flows into the detector and a voltage appears. The quasiparticle current from S to N2 equals $eG_{\mathrm{NN},2}Q^*(x)/2e^2N(0)$ [51; 52], where $N(0)$ denotes the density of states of the normal quasiparticles and $G_{\mathrm{NN},2}$ the normal state conductance of the NS junction 2. The term $e^2N(0)$ is the so-called electrochemical capacitance. The current back-flow from N2 to S is given by $U_2 G_{\mathrm{NS},2}$, where $G_{\mathrm{NS},2}$ is the conductance of the NS junction 2 and $U_2 << \Delta/e$. Equating these two currents leads to

$$U_2(x) = \frac{Q^*(x)}{2eN(0)g_{\mathrm{NS},2}} = \frac{Q^*(0)e^{-\frac{|x|}{\Lambda_{Q^*}}}}{2eN(0)g_{\mathrm{NS},2}} \qquad (2.9)$$

with $g_{\mathrm{NS},2} = G_{\mathrm{NS},2}/G_{\mathrm{NN},2}$ being the normalized tunneling conductance for the NS detector junction in the low-voltage limit. $U_2(x)$ can be identified with a nonlocal voltage $U_{\mathrm{nl},2}$ if the detector is not in the current path of the injecting circuit. CI is then called nonlocal CI. For the nonlocal geometry we define the nonlocal resistance as $R_{\mathrm{nl}} := U_{\mathrm{nl},2}/I_{\mathrm{tot},1}$ and obtain with eq. (2.7) and (2.9) the following distance dependent expression

$$R_{\mathrm{nl}}(x) = \frac{F^*\tau_{Q^*}e^{-\frac{|x|}{\Lambda_{Q^*}}}}{2e^2N(0)\Omega g_{\mathrm{NS},2}}. \qquad (2.10)$$

According to [48] the relaxation time for CI near T_{C} is given by

$$\tau_{Q^*} = \frac{4}{\pi}\tau_E\frac{k_{\mathrm{B}}T_{\mathrm{C}}}{\Delta(T)} = \frac{4}{\pi}\tau_E\frac{k_{\mathrm{B}}T_{\mathrm{C}}}{\Delta(0)\sqrt{1 - T/T_{\mathrm{C}}}} \qquad (2.11)$$

where τ_E is the inelastic scattering time [53]. With eq. (2.11) in (2.10) we find for the nonlocal resistance close to T_{C}:

$$R_{\mathrm{nl}}(x) = \underbrace{\frac{2\tau_E k_{\mathrm{B}}F^*}{e^2\pi\Omega N(0)}}_{=K} \cdot \frac{T_{\mathrm{C}}}{g_{\mathrm{NS},2}\Delta(0)\sqrt{1 - T/T_{\mathrm{C}}}} \cdot e^{-\frac{|x|}{\Lambda_{Q^*}}}. \qquad (2.12)$$

If the temperature approaches T_{C} the relaxation time diverges and the charge imbalance length gets very long. Because of $x << \Lambda_{Q^*}$ the exponential term

in eq. (2.12) can be neglected. For $R_{\mathrm{nl}}(x)$ follows

$$R_{\mathrm{nl}} \approx K \frac{T_{\mathrm{C}}}{g_{\mathrm{NS},2}\Delta(0)\sqrt{1 - T/T_{\mathrm{C}}}}. \tag{2.13}$$

Equation (2.13) shows that R_{nl} increases with T and diverges for $T = T_{\mathrm{C}}$. It is important to note that for the constant K in eq. (2.12) and (2.13) we assume F^* to be constant and independent of T. This is incorrect as $I_{Q^*,1}$ is temperature dependent.

However, on the basis of the "classical" CI theory we have derived the temperature- and distance-dependent behavior of R_{nl} caused by nonlocal CI (see eq. (2.12)).

Chapter 3

Dynamical Coulomb blockade

3.1 Introduction

This chapter deals with charging effects on ultra-small tunnel junctions, which have been observed in various different multi-junction devices [54; 55; 56; 57; 58; 59; 60]. In the case of a single ultra-small metal-insulator-metal tunnel junction [61; 62; 63; 64; 65; 66] these charging effects are commonly referred to as environmental or dynamical Coulomb blockade (DCB). Here we focus on single tunnel junctions in layered structures similar to those prepared in this thesis.

It has been shown theoretically and experimentally that for small tunnel junctions with capacitances of the order of 10^{-15} F or smaller [67] and at cryogenic temperatures the zero-bias differential resistance R_0 in metal/insulator/metal samples is enhanced compared to the high-voltage differential resistance R. This effect, often referred to as Coulomb blockade (CB), is due to the change of charge on the junction when an electron tunnels. This leads to charging effects with charging energy $E_C = e^2/2C$. Due to E_C the electron transport through the junction is blocked for bias voltages $U < |e|/2C$ [57; 68]. This is the so-called Coulomb gap and leads to a high-voltage offset of $|e|/2C$. To be able to observe CB effects thermal fluctuations need to be small which leads to the prerequisite $k_B T << E_C$.

This chapter is structured as follows: For a more intuitive picture the charging (DCB) effects are first introduced in a semiclassical picture. In a second step DCB is treated quantum-mechanically. Even though the results in both cases will be the same, we need the quantum-mechanical treatment to introduce the possibility of exciting electromagnetic modes, which will be

important for the interpretation of our results. For an excellent theoretical review we refer to [69].

3.2 Semiclassical picture

The understanding of charging effects on small tunnel junctions requires a description of the tunneling process and of the environment of the junction. This chapter describes a semiclassical picture, as it treats tunneling quantum-mechanically and the environment classically.

Metal/insulator/metal tunneling junctions connected to an ideal voltage source are discussed in chapter 2. It was shown that in this case the tunnel junctions can be described by the tunneling resistance R_T and that independent of the temperature the I-U-characteristics exhibits the same form as for an ohmic resistor R, namely

$$I(U) = \frac{U}{R_T}. \tag{3.1}$$

It should be noted that R_T and R have a different physical origin.

The capacitance C of a tunnel junction is usually modeled as a capacitance in parallel to R_T. In this case a tunneling electron changes the charge Q on the capacitance by e. This leads to a charging of the junction depending on its electromagnetic environment. If we assume the tunnel junction to be connected to an ideal voltage source with ideally conducting leads (environmental impedance $Z(\omega) = 0$), see Fig. 3.1(a), no charging effects occur since the junction capacitance is recharged immediately. If we assume a large environmental impedance ($Z(\omega) \neq 0$), see Fig. 3.1(b), which is large enough to avoid fast recharging after a tunneling event, the junction is charged by the tunneling event. As a consequence the energy gain of a tunneling electron is not eU (with $e > 0$ and U being the potential difference on the junction), but $eU - e^2/2C$ due to the charging energy $E_C = e^2/2C$ which needs to be provided by the tunneling electron when charging the capacitance. Consequently, for $eU < e^2/2C$, an electron cannot tunnel since it is energetically unfavorable which results into a bias regime of enhanced resistance, also called Coulomb gap. A consequence of this is a bias offset of $e/2C$ compared to the ohmic-like current-voltage characteristic of a tunnel junction embedded in a zero-impedance environment.

Experiments and theoretical predictions have shown that the Coulomb gap exhibits its sharpest features for very high-ohmic environmental impedances $Z(\omega)$ and junction tunneling resistances R_T well above the resistance quantum $R_Q = h/2e^2 = 12.9\,\text{k}\Omega$. If $Z(\omega)$ is of the order of R_Q, the zero-bias differential resistance decreases with lowering the environmental impedance
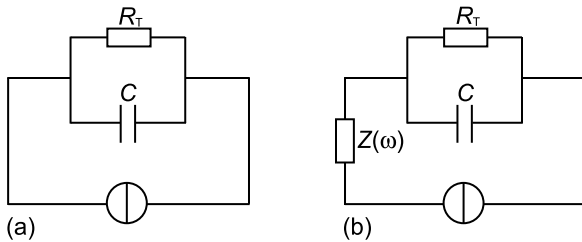
Figure 3.1: Model circuit of an ultra-small tunnel junction connected to an ideal voltage source. The junction is represented by R_T and C in parallel. (a) Tunnel junction without environmental impedance ($Z(\omega) = 0$). (b) Tunnel junction with environmental impedance ($Z(\omega) \neq 0$).

resulting in a smearing of the Coulomb gap [61; 70; 71]. To understand these features it is necessary to study the dependence of the environmental impedance $Z(\omega)$ on CB. Besides the intuitive picture of the charging time of a capacitance and its dependence on $Z(\omega)$, another intuitive explanation is possible when modeling the circuit.

As depicted in Fig. 3.1(b) the tunnel junction is modeled by R_T and C in parallel with an environmental impedance $Z(\omega)$ in series describing the external circuit. To determine the voltage over the tunneling element R_T one needs to know the total impedance $Z_t(\omega)$ as seen from R_T. $Z_t(\omega)$ results from C and $Z(\omega)$ in parallel to [69]

$$Z_t(\omega) = \frac{1}{i\omega C + Z^{-1}(\omega)}. \tag{3.2}$$

Examining the extreme cases of very low and very high $Z(\omega)$, we gain an intuitive understanding of the environment's influence on DCB. From eq. (3.2) we can conclude that for very low impedances $Z(\omega)$ the capacitance is shorted, leading to negligible charging effects, whereas in the high-impedance case the capacitance and therefore charging effects are important.

3.3 Quantum-mechanical picture

The semiclassical and quantum-mechanical picture describes the same physical effect and certainly obtains the same results. However, it is necessary to introduce and treat the environment besides the tunneling process quantum-mechanically too. In a complete quantum-mechanical treatment [70; 71], DCB is closely related to the possible excitation of environmental electro-

magnetic modes, which will be of importance for the interpretation of our results.

The Hamiltonian describing the complete system is the sum of each contribution

$$H_{\text{tot}} = H_{\text{qp}} + H_{\text{env}} + H_{\text{T}} \tag{3.3}$$

wherein H_{qp} describes the quasiparticles in the two metal electrodes, H_{env} the environment and H_{T} the tunneling.

The tunneling Hamiltonian is given by

$$H_{\text{T}} = \sum_{k,q,\sigma} T_{kq} c_{q\sigma}^* c_{k\sigma} e^{-i\varphi} + h.c. \tag{3.4}$$

and includes in contrast to the tunneling Hamiltonian of eq. (1.3) the possibility that a tunneling electron needs to pay energy depending on the environment. H_{T} of eq. (3.4) has the same form and parameters as the tunneling Hamiltonian of eq. (1.3), except the operator $e^{-i\varphi}$ with φ as the phase of the junction describing the voltage on the contacts[1]. This operator couples the electrodes with the electromagnetic environment. It reduces the charge of the junction by e from Q to $Q - e$, which includes possible charging effects. Without environment ($Z(\omega) = 0$) $e^{-i\varphi}$ is negligible and thus leads to no charging effects.

In a quantum-mechanical description of the environment, the environmental impedance is modeled in the simplest case with an inductance L by $Z(\omega) = i\omega L$. The resulting LC-circuit can be viewed as an harmonic oscillator of frequency $\omega = 1/\sqrt{LC}$. A large number of these harmonic oscillators in parallel with $\omega_n = 1/\sqrt{L_n C_n}$ can be used to model arbitrary $Z(\omega)$ (same principle as in Fourier transformation) and the dissipation of the environment. This approach leads to the necessary Hamiltonian H_{env} describing the environment. The whole set of harmonic oscillators with their frequencies result in modes which can be excited by a tunneling electron. Which modes are excited depends on the electromagnetic environment.

With higher external circuit impedance $Z(\omega)$ the junction can couple to modes with lower frequency. A tunneling electron which excites these low-energy modes is equivalent to inelastic tunneling. The electron dissipates energy into the environment. The probability for such an excitation is given by function $P(E)$ [70]. We can conclude that for DCB a tunneling electron needs to excite modes of the high impedance environment.

In contrary, for a low $Z(\omega)$ environment, the junction can only couple to high-frequent and therefore high-energy modes. For low bias the electrons tunnel elastically since they do not have enough energy to excite modes.

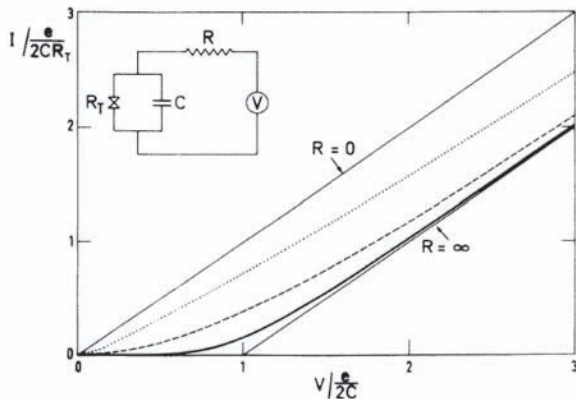[1]For more detailed information to φ, see [69].

Figure 3.2: *I-U*-characteristic of a tunnel junction at $T = 0$ coupled to an environment characterized by a resistance R (see inset) for $R/R_Q = 0, 0.1, 1, 10$ and ∞ [70].

For large bias the electrons have enough energy and inelastic tunneling can occur.

In this quantum-mechanical picture the determination of the *I-U*-characteristics can get very complicated even for simple systems. Therefore we only show the current-voltage characteristics for $T = 0$ and $U > 0$, which reads

$$I(U) = \frac{1}{eR_T} \int_0^{+eU} dE(eU - E)P(E). \tag{3.5}$$

Since $T = 0$, eU is the maximum energy a tunneling electron can provide to excite the environment. In order to calculate the *I-U*-characteristics one has to sum over all possible modes with energy E which can get excited with the probability $P(E)$ in an energy window from zero to eU. In the extreme case $Z(\omega) = 0$, the probability $P(E) = \delta(E)$ reduces eq. (3.5) to eq. (3.1), which is a linear *I-U*-characteristics. In case of a very high environmental impedance $(Re(Z(\omega)))$, $P(E) = \delta(E - E_C)$ and eq. (3.5) gives

$$I(U) = \frac{eU - E_C}{eR_T}\Theta(eU - E_C) \tag{3.6}$$

with $\Theta(E)$ being the unit step function. Due to the environment only modes with energy E_C are excited and no current flows for $eU < E_C$, which describes the Coulomb gap. For finite temperature $P(E) = \delta(E - E_C)$ is

replaced by a Gaussian distribution describing the smearing of the Coulomb gap with increasing T.

So far, we have only discussed the two extreme cases of very low and high environmental impedances. In Fig. 3.2 the calculated current-voltage-characteristics [70] of an ohmic environment ($Z(\omega) = R$) also show the intermediated cases for different values of R at $T = 0$. As was discussed above for a general impedance, an ohmic environment does reproduce the linear I-U-characteristics for $Z(\omega) = R = 0$ and the Coulomb gap for $Z(\omega) = R = \infty$. The Coulomb gap is washed out in the intermediate regime $0 < R < \infty$ with decreasing R.

To model real experiments it is necessary to describe the environment as a transmission line [69], a distribution of resistors, inductors and capacitances. Without going into detail, the current-voltage characteristic of a junction connected with an LC transmission line with external impedance $Z(\omega)$ is described by [69]

$$I(U) = \frac{1}{eR_{\mathrm{T}}} \left[eU + \int_{-\infty}^{+\infty} \frac{dE}{E} \frac{1}{1 - e^{-\beta E}} \frac{Re Z_{\mathrm{t}}(\omega)}{R_{\mathrm{Q}}} \right.$$
$$\left. \times \left(\frac{(eU - E)(1 - e^{-\beta eU})}{1 - e^{-\beta(eU-E)}} - eU \right) \right] \quad (3.7)$$

with $\beta = 1/k_{\mathrm{B}}T$. The results of a measurement on a Pd/AlO$_{\mathrm{x}}$/Al junction with a barrier resistance of $1.4\,\mathrm{k\Omega}$ and a junction capacitance $C \approx 0.5\,\mathrm{fF}$ are
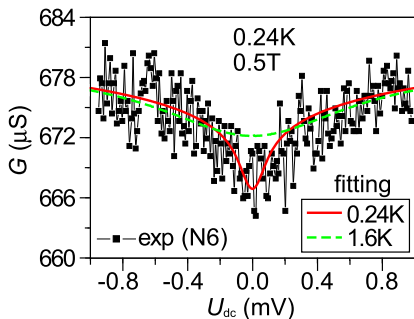
Figure 3.3: Differential conductance G vs. bias measurement of a Pd/AlO$_{\mathrm{x}}$/Al junction with a magnetic field of $0.5\,\mathrm{T} > H_{\mathrm{C}}$ applied in-plane at $0.24\,\mathrm{K}$. The fits are performed for $0.24\,\mathrm{K}$ and $1.6\,\mathrm{K}$ and assume an infinite LC transmission line with $Z(\omega) = 105\,\Omega$. For details see text.

shown in Fig. 3.3. For this junction the differential conductance G vs. bias characteristic is determined at $0.24\,\mathrm{K}$ with an applied magnetic field of $0.5\,\mathrm{T}$. As this magnetic field is larger than the critical field, superconductivity is suppressed which avoids features due to the superconducting gap. Due to DCB the experiment shows a decrease of conductance around zero bias (zero-bias anomaly). The experimental data can be modeled with eq. (3.7). Assuming an infinite LC transmission line[2] one obtains with $T = 0.24\,\mathrm{K}$, $Z(\omega) = 105\,\Omega$ and $R_\mathrm{T} = 1.4\,\mathrm{k\Omega}$ a good agreement between theory and experiment as shown in Fig. 3.3. Moreover, theory shows as expected a smearing of the zero bias anomaly with increasing T, see Fig. 3.3.

---

[2]For an infinite LC-transmission line the impedance is purely ohmic and reads $Z_\infty = \sqrt{L_0/C_0}$ with inductance L_0 and capacitance C_0 per unit length [69].

Chapter 4

Sample fabrication and measurement setup

In the first part of this chapter we will explain the main methods used for the sample preparation, namely electron-beam lithography and metal deposition with special emphasis on angle-evaporation. Closely related to angle-evaporation is on the one hand the mask design, which is constrained due to this special evaporation technique. On the other hand we installed a new molecular beam epitaxy (MBE) system. We give a short overview on this new system with special focus on problems with thermally evaporating aluminum. A complete fabrication cycle of an NIS hybrid device similar to the one shown in Fig. 2.3 is described at the end. In the second part of this chapter we introduce our four-terminal nonlocal measurement and the low temperature setup.

4.1 Electron-beam lithography

Electron beam lithography (EBL) is a standard method for the preparation of "top-down" fabricated nanoscale structures. The basic principle of this process is to write the desired nanostructure patterns with an electron beam into an electron-sensitive polymer film (mask) that was deposited beforehand onto the surface of the sample substrate. After writing the structure, the mask is developed by dissolving the written areas. Subsequently, in the metalization step a metal is deposited on the polymer, and where the polymer was removed, on the substrate. At the end in the lift-off process, the whole mask is removed leaving behind only the metalized pattern on the substrate written by the electron beam.
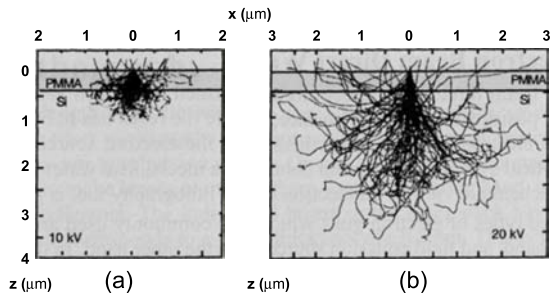
Figure 4.1: Monte Carlo simulation of the electron path in the PMMA and the Si substrate for (a) 10 kV and (b) 20 kV acceleration voltage. At lower voltage the electrons interact closer to the surface and therefore expose the resist more, leading to the proximity effect [72].

For the electron sensitive mask, commonly referred to as e-beam resist, we use polymethylmethacrylate (PMMA). By spinning this e-beam resist is spread over the substrate surface as a homogeneous flat film of several hundred nanometers thickness. Baking hardens the PMMA and removes the solvents. PMMA consists of long chains of polymers. In the lithography step their bonds break by bombarding them with accelerated electrons. Due to their reduced molecular weight, the shorter polymers can be more easily dissolved by the developer, a 1:3 mixture of 4-methyl-2-pentanone (MIBK) and isopropanol, leaving the exposed areas uncovered by the e-beam resist.

In EBL, an electron microscope acts as the source for accelerated electrons with kinetic energy of several keV. The resolution of the written patterns is not limited mainly by the focus of the electron beam, which is of the order of nm, but by the so-called proximity effect. This effect is due to electrons, which scatter in the substrate in a random way and interact with the PMMA leading to a broadening of the exposed areas, see Fig. 4.1. This is the reason why structures smaller than 40-50 nm are very hard to obtain.

4.2 Metalization

After the lithography process and the development of the written patterns, the surface needs to be metalized for which several different techniques exist [72]. We restrict ourselves to discuss only techniques used in this thesis. In the beginning we used an electron gun evaporation system. This system

consists of a vacuum chamber with a base pressure of 10^{-6}-10^{-7} mbar. An e-gun accelerates electrons to $10\,\text{keV}$ and bombards the source material. The material heats up and atoms are evaporated from the source into the vacuum and finally condense on the substrate forming a thin film. In this thesis we changed to a solid-source molecular beam epitaxy (MBE) system, which has, in contrast to the e-gun evaporation system, a base pressure of $< 5 \cdot 10^{-10}$ mbar, but slower deposition rates allowing the growth of epitaxial films. Due to the slow deposition rates an excellent vacuum is a prerequisite for MBE systems to ensure ultra-clean materials and surfaces. The source materials are thermally heated in effusion cells to temperatures just below the melting point T_m. Atoms of the source material are sublimated, move through the vacuum and condense on the substrate surface. Some materials have a very low vapor pressure leading to vanishingly small deposition rates. As a consequence, heating to temperatures above T_m is needed, which leads to complications as in the case of Al. This issue will be discussed in detail further below.

After metalization we rinse the samples for approximately one hour in $50\,°\text{C}$ warm acetone, which insures dissolving of the e-beam resist (lift-off process). The evaporated material only remains on the sample where it has direct contact to the substrate surface. Since this is only the case for the lithographically written pattern, the planned nanostructure is implemented on the substrate surface.

4.3 Angle-evaporation and sample design

With the angle-evaporation technique it is possible to prepare junctions of two or more materials in only one lithography step. This is necessary for obtaining clean interfaces as the sample stays in the same vacuum chamber during the whole process. As the name "angle-evaporation" suggests, different materials are evaporated under certain angles α relative to the normal of the substrate surface, see Fig. 4.2(a). Two or more structures are obtained with one mask, which consequently needs large undercuts in the e-beam resist as depicted in Fig. 4.2. A prerequisite for obtaining large undercuts with EBL are thick PMMA layers[1] (in our case $900\,\text{nm}$). Then, in the lithography step it is necessary to apply a high exposure dose of the electron beam on the PMMA in order to ensure that a large number of electrons are available to interact with the resist. Furthermore, rather low acceleration voltages are needed since this guarantees electron interaction with the substrate and

---

[1] Instead of using a single PMMA layer, it is possible to use a PMMA/MMA double layer with methylmethacrylate (MMA) as a higher electron sensitive material. We used single PMMA layers and therefore do not describe this approach.
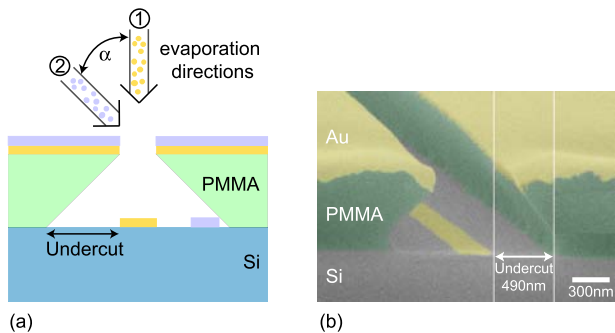
Figure 4.2: (a) Schematic of angle-evaporation (b) Artificially colored SEM image of a PMMA undercut on a Si substrate. For better contrast and to protect PMMA, Au was evaporated on top.

the PMMA closer to the surface as shown in a Monte Carlo simulation for 10 and 20 kV in Fig. 4.1.

The adjustment of the evaporation angle with the undercut is important, but time consuming. Besides, wrongly chosen angles, misaligned samples and not well adjusted distances L and d (Fig. 4.3(a)) can lead to a destruction of the structure during the lift-off process. Details for our angle-evaporation process are given in chapter 4.5.

The easiest structures to obtain with angle-evaporation are two parallel lines as shown in Fig. 4.2(a) since it only needs a well-adjusted evaporation angle α. However, angle evaporation and the sample design complicate when preparing junctions. In case of only one junction, α *and* the distance L need to be adjusted, see Fig. 4.3(a). If we include a second junction with adjacent, parallel contact lines, this adds the contact distance d to the adjustable parameters. As shown in Fig. 4.2(a) the parallel contact lines have an undercut limiting the minimum distance d between contacts. To minimize the overlap problem of the undercuts, we avoid parallel patterning of the Pd lines as much as possible, see Fig. 4.3(f). However, in our structures we are constraint to a minimum distance of $d \approx 300$ nm. For our experiments we need to decrease this distance. We solve this problem by designing shifted Pd contact lines on both sides of the central Al line, see Fig. 4.2(a), as this guarantees on the one hand less problems with undercut overlap of parallel lines and on the other hand a reduced distance between contacts. With this sample design we achieve injector-detector distances of 50 nm, but it complicates the sample fabrication considerably. First, this sample design
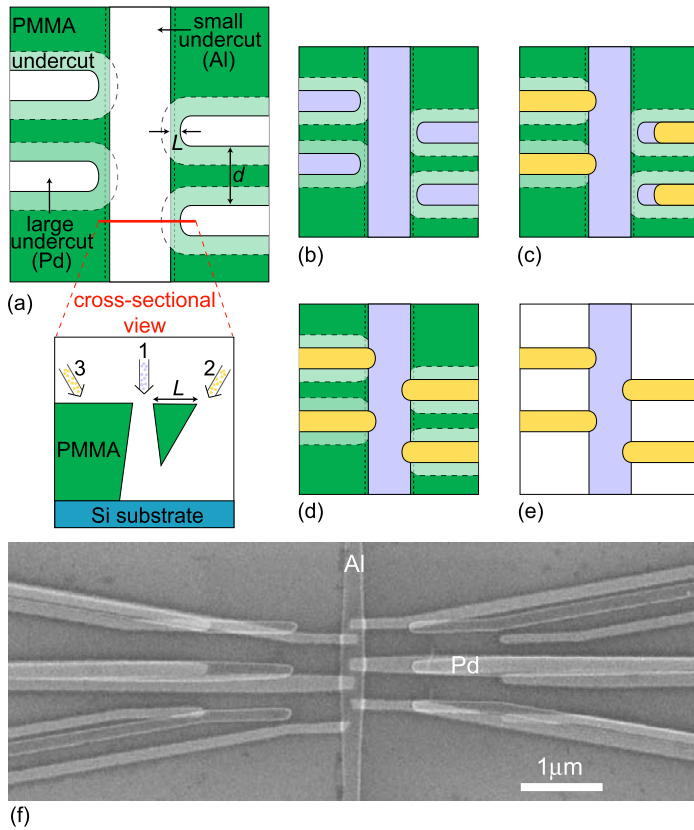
Figure 4.3: Schematics of the pattern written by e-beam lithography (a) before metalization (b) after evaporating Al with $\alpha = 0\,^\circ$ (c+d) after evaporating Pd twice with $\alpha = \pm 40\,^\circ$ and (e) after lift-off. (f) SEM image of a typical sample. The three different evaporation steps are clearly visible.

requires a second tilting angle. Second, we need to solve the general problem in angle-evaporation that besides desired structures also unwanted structures form due to the undercut. Thus, we design (see Fig. 4.3(a)) the central Al line with as little undercut as possible to avoid parallel Pd lines, which would connect the Pd contacts and consequently short circuit the whole device. This is the most crucial point, which lowered the yield of working

devices considerably. Closely related to this problem is the distance L, see Fig. 4.3(a), which also leads, once wrongly chosen, to either no junction or short circuits. To enhance the yield and to enable distance-dependent measurements, we implemented six NIS junctions.

4.4 The new molecular beam epitaxy system and Aluminum evaporation

One of the decisive parameters for the observation of CAR is the coherence length of the superconductor, in our case Al. It is more probable to measure a nonlocal process like CAR or EC if we increase the coherence length by improving the structural and electronic properties of Al. It also increases the magnitude of the measured nonlocal signal, which is crucial as the signals are usually very small and close to the detection limit. An improved quality of Al can be obtained by reducing the Aluminumoxid AlO_x content in the Al layers and by evaporating Al onto a cold substrate. Therefore, the Al quality is mainly determined during the preparation process by the vacuum, the deposition rate and the sample cooling and thus is closely related to the evaporation system. Our new MBE system, which we installed and extended considerably, serves on the one hand to improve the Al quality and on the other hand for the preparation of ferromagnetic materials. Both, Al and ferromagnetic materials, need ultra-high vacuum (UHV), a criterion which is met by our new MBE system with a typical base pressure $< 5 \cdot 10^{-10}$ mbar. Moreover it allows better substrate cooling (-50 °C) and a nearly unlimited range of tilting and rotation possibilities for angle-evaporation.

The MBE system consists of the process chamber and the load lock, see Fig. 4.4(a). The latter allows one to load a sample without breaking the UHV in the process chamber. We included the possibility for sample oxidation and integrated a sputter gun into the load lock e.g. for surface cleaning. A lamp for heating is used either for removing adsorbates from the surface or to heat up cold samples coming out of the process chamber.

The process chamber presently contains five effusion cells and an e-gun with four separate pockets. Both evaporation methods combined in one chamber gives the opportunity of evaporating very different materials. By cooling the chamber walls down to liquid nitrogen temperatures, they act as cryogenic pumps and improve the UHV considerably. The substrate holder can be cooled to -50 °C. For both cooling cycles we set up a fully automated system, that cools down with an optimized nitrogen usage and protects the evaporator from getting air inside the cold system once a dewar is empty. The substrate holder can be tilted by $\pm 60°$ and rotated completely around the main axis and $\pm 180°$ around the normal of the substrate surface giving
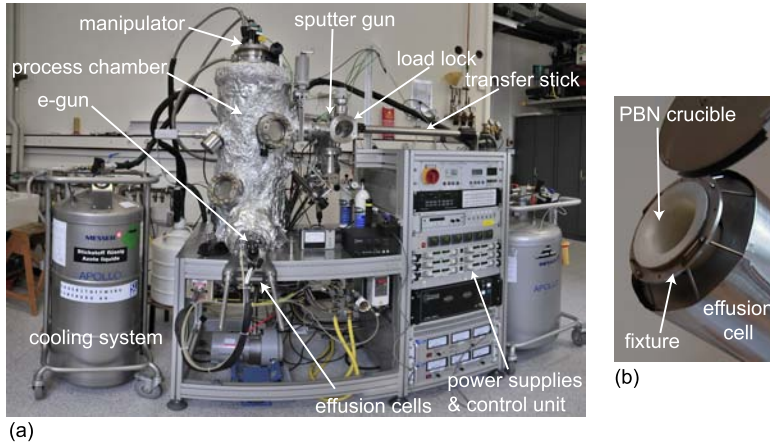
(a)

(b)

Figure 4.4: (a) Our new MBE system consisting of a load lock and a process chamber. Integrated in the MBE system are five effusion cells (not visible), one sputter gun, one e-gun, a nearly complete rotatable and tiltable substrate holder and separated automated cooling of the process chamber and the substrate holder. (b) Cold-lip effusion cell with a fixture to lift the pyrolytic Bornitrid (PBN) crucible to increase the temperature gradient.

nearly complete freedom for angle-evaporation.

When evaporating Al with a MBE system, there are certain problems that require the appropriate precautions. In an effusion cell the vapor pressure of Al is very low if T is below the melting temperature T_{m}, leading to an exceedingly small deposition rate. Instead of sublimation it is possible to raise the deposition rate by heating Al above T_{m}. An upper limit for increasing T and therefore the deposition rate is given by the fact that Al tends to creep out of the crucible, an effect which is more distinct for higher T. Once Al creeps over the rim of the crucible, it can cause a short in the Tantalum filament of the effusion cell. For this reason, we only fill the crucible to 1/3. Additionally, we have installed a cold-lip effusion cell, which is cooled at the orifice of the cell to establish a temperature gradient and stop the Al creeping. In order to obtain an acceptable evaporation rate of $170\,\mathrm{mÅ/s}$ at $T = 1100\,^{\circ}\mathrm{C}$ for Al, this temperature gradient turned out to be too small. We increased this gradient by constructing a fixture to lift the crucible approximately $1\,\mathrm{cm}$ out of the effusion cell, as shown in Fig. 4.4(b), which solved the creep problem.

Another problem represents the melting of Al. If Al solidifies the crucible

can break when cooling it below T_m due to the different linear expansion coefficients[2] of Al and the crucible material pyrolytic Bornitrid (PBN)[3]. At operating temperature of $T > T_m$ the crucible is expanded and the extra space filled by the molten Al. When the heater is switched off the Al shrinks less than PBN leading to tensions and to a possible breaking of the crucible. For this reason, we keep Al at $T > T_m = 660\,°C$, in our case at $710\,°C$. As a precaution, we installed a power back-up system in case of power failures to avoid an uncontrolled cooling of the effusion cell. For a controlled cool-down the manufacturer advises a rate of 1-2 K/min and an exchange of the crucible [73]. Since the latter is very expensive we found a way to reuse the crucibles by unhinging the Al with a 1 molar Copper(II) chloride dihydrate ($CuCl_2 + 2H_2O$) solution diluted with 5% hydrochloric acid (HCl). The detailed procedure is described in Appendix B. After this procedure ($\approx$2 weeks), the crucible requires a thorough examination with an optical miscroscope for possible cracks.

4.5 Fabrication process

This chapter gives a detailed description of the fabrication process to facilitate a reproduction of similar devices. The preparation process described ideally takes two days.

For all samples we used undoped Silicon (Si) wafers with 100 nm thermal oxide as substrate, which we first cut into $1 \times 1\,cm^2$ pieces. After sonicating the substrates in acetone and isopropanol (10 min each), we used an ozone cleaner (10 min) and finally the plasma etcher (process pressure=0.025 Torr O_2, RF power=200 W, t=30 s) to remove all organic remains on the SiO_2 surface. Afterwards we used a spinner (4000 rpm, t=40 s, ramp=4 s) to obtain a 900 nm thick, homogeneous PMMA layer (1:5 mixture of chlorobenzene and PMMA for dilution) which needed a bake out ($175\,°C$/45 min) in the oven to harden it and remove the solvents.

We prepared four independent $2 \times 2\,mm^2$ structures in the e-beam lithography. Since the angle-evaporation technique requires only a single lithography step, we had to write the big structures (contact pads) and the small nanoscale contacts at once. In order to save time and avoid e-beam shifts, we only used one acceleration voltage of 10 kV. Furthermore, we avoided shifts by writing each sample structure completely (small and big structures) be-

---

[2]The linear expansion coefficient of Al is $\alpha = 23.8 \cdot 10^{-6}\,K^{-1}$ and of pyrolytic Bornitrid $\alpha_a = 3.1 \cdot 10^{-6}\,K^{-1}$ and $\alpha_c = 36 \cdot 10^{-6}\,K^{-1}$ with a being in the direction parallel to the crucible walls and c perpendicular.

[3]PBN turned out to be the best suited crucible material being relatively resistive against cooling below T_m and due to an acceptable creeping behavior of Al.

fore moving the stage to write another pattern[4].

After the lithography, we cut the substrate to $2 \times 2\,mm^2$ pieces that fit into a chip carrier. This was done before the development step in order to avoid contamination and damage of the fine structures by Si dust from the cutting. The PMMA was developed for 1 min in a 1:3 mixture of 4-methyl-2-pentanone (MIBK) and isopropanol. Immediately afterwards we put the sample into isopropanol to terminate the developing process. If the structures looked promising under the light microscope, a short, weak cleaning in the plasma etcher (process pressure=0.3 Torr O_2, RF power=30 W, t=50-65 s) was necessary to remove all PMMA residues on the developed areas.

For the evaporation process it was important to align the substrate exactly on the substrate holder. For the thermal evaporation of Al the substrate was cooled to -50 °C in the process chamber. After the evaporation of 40-50 nm Al ($\alpha = 0\,°$) at 1100 °C with typical rates of 170 mÅ/s, the sample was left in the chamber for approximately 15 h to warm up. The sample was then transferred into the load lock for the preparation of the tunneling barrier, heated for 60 min with a heating lamp ($I = 1.7\,A$, $U = 2.4\,V$) to roughly 80 °C and finally oxidized between 2 to 30 min in a pure oxygen atmosphere of 8-13 mbar while keeping T at $\sim 80\,°C$[5]. Following, the sample was transferred back into the process chamber and cooled to -50 °C. Finally, a 40 nm Palladium (Pd) layer is evaporated twice, once with a tilting angle of $\alpha = 40\,°$ and once with $\alpha = -40\,°$ at $T = 1510\,°C$ and 50 mÅ/s.

In the following lift-off process the samples were rinsed in warm (50 °C) acetone for approximately one hour. To avoid contamination of the sample surface with leftovers from the removed PMMA and metal, the acetone bath is changed three times before ending the lift-off process in an isopropanol bath. Now, the sample structures were checked[6] with a scanning electron microscope (SEM).

In the last step, the sample was glued into a chip carrier with PMMA. In the following bonding procedure, we created a macroscopic electrical connection between the contact pads of the chip carrier with the ones on the sample. We bonded the contacts in such a way that adjacent contacts were not connected with the same twisted pair of the cryostat wiring in order to minimize possible crosstalk. During bonding, but also for all other following steps, it was extremely important to prevent currents due to unwanted charging that can destroy the sample and/or the tunneling barriers.

---

[4]It turned out to be an efficient way of preparing samples to automatize the whole lithography process with a writing protocol in the Elphy-software.

[5]Most samples were oxidized with this procedure. For further details see chapter 5.2.

[6]In order to avoid a possible change or destruction of the tunneling barrier, we tried to minimize the scanning time.

4.6 Measurement setup

4.6.1 Low temperatures and filtering

The experiments are performed at cryogenic temperatures. This is necessary since we measure nonlocal effects related to superconductivity, that inevitably needs temperatures below T_C, which is $1.19\,$K in the case of bulk Al. As we study local and nonlocal subgap transport, the characteristic energy scale of our measurements is set by the superconducting energy gap of Al, $\Delta \approx 0.2\,$meV. Therefore, the thermal energy $k_B T$ and applied bias energies eU need to be considerably smaller than Δ to avoid washed out features. As we measure at a base temperature of $0.23\,$K, which corresponds to a thermal energy of $20\,\mu$eV and an applied ac bias of $\sim 10\,\mu$eV, the above criterion is fulfilled.

We reach these low temperatures with the help of a ^{3}He-cryostat[7]. Its outer part decouples the cryostat from room temperature with an isolation vacuum. Further inside liquid nitrogen precools the system to $77\,$K. In the core of the cryostat $4.2\,$K is reached with liquid ^{4}He. Reducing the vapor pressure of the liquid ^{4}He by pumping on the system decreases the boiling point to $1.3\,$K. This leads to cooling of the so-called 1 K pot by the enhanced evaporation of ^{4}He. As ^{3}He is very expensive, it is stored in a closed system separated from ^{4}He. Due to thermal contact of the ^{3}He-system with the 1 K pot, ^{3}He gas condenses below $2\,$K. The liquid ^{3}He is collected in the so-called ^{3}He pot (in thermal contact with the sample holder) and by pumping on it, the base temperature of $0.23\,$K can be reached. For a schematic of a ^{3}He-cryostat, we refer to [74].

Measuring at cryogenic temperatures necessarily includes adequate filtering to avoid heating and electronic noise by the environment. At room temperature we use for every wire commercially available LC low-pass filters (π-filters), which show a damping of 40-60 dB for frequencies larger than $0.3\,$MHz [75]. At cryogenic temperatures we use so-called tape worm filters [76], which were built in-house and show an estimated attenuation of $60\,$dB at $1\,$GHz and a dc resistance of $64\,\Omega$ [77]. These RLC low pass filters consist of twisted pairs[8] wrapped in a Copper tape to form a lossy transmission line. Due to the skin effect high frequency currents flow close to the surface of the conductor and thus face a higher resistive environment along the wire while the capacitive coupling to the Copper tape acts as a ground for them.

---

[7]The ^{3}He-cryostat is an *Oxford Instruments Heliox VL* system.

[8]The wires consist of isotan, a CuNi alloy, with a core diameter of $80\,\mu$m and a $10\,\mu$m insulating varnish on the basis of polyurethane.

4.6.2 Measurement scheme

In our experiments we distinguish between local and nonlocal measurements. All measurements are local except those which measure voltage out of the current path, which we refer to as nonlocal. We use standard lock-in technique[9] and perform either two-terminal local measurements to determine the bias dependent local differential conductance G of the NIS junctions or four-terminal nonlocal measurements to examine the bias dependent nonlocal differential resistance R_{nl}. We use the local two-terminal measurements to characterize the NIS junctions, whereas with the nonlocal results we study transport processes like CAR, EC and CI. The measurement scheme is shown in Fig. 4.5 and the electronic setup is displayed in Fig. 4.6.
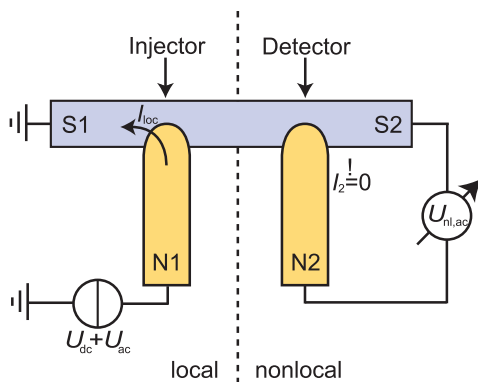
Figure 4.5: Schematic of the measurement setup. In this four-terminal nonlocal measurements the detector needs to be out of the local current path which sets the boundary condition $I_2 = 0$.

The junction is voltage-biased with an applied bias $U = U_{dc} + U_{ac}$ between the normal metal contact N1 (injector) and the grounded superconductor lead S1 causing a local current $I_{loc} = I_{dc} + I_{ac} = I_1$ as shown in Fig. 4.5. The dc bias U_{dc} enables us to set and sweep the potential at the injecting NIS junction[10]. A small ac bias U_{ac} (small compared to Δ) modulates U_{dc} allowing the use of lock-in technique. We measure both, I_{loc} and the nonlocal potential difference $U_{nl,ac} = U_2$ between the normal contact N2 (detector) and the second superconducting contact S2. I_{loc} is determined by a volt-

---

[9]We use *Stanford Research Systems SR830 DSP* lock-in amplifiers.
[10]A *Yokogawa 7651* is used as dc voltage source.
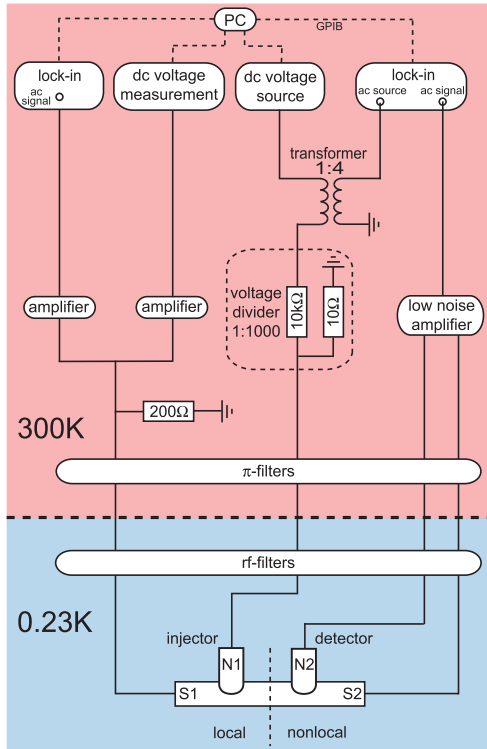
Figure 4.6: Electronic setup for our local and nonlocal measurements at cryogenic temperatures.

age measurement over a load resistor of $200\,\Omega$. Since we know I_{loc} and the resistances along the current path, we can determine the local voltage drop $U_{\mathrm{loc}} = U_1$ over the injecting NIS junction[11](not shown in Fig. 4.5). Our measurement setup enables us to determine either the local differential conductance $G = dI_{\mathrm{loc}}/dU_{\mathrm{loc}} \approx I_1^{\mathrm{ac}}/U_1^{\mathrm{ac}}$ or the nonlocal differential resistance $R_{\mathrm{nl}} = dU_{\mathrm{nl}}/dI_{\mathrm{loc}} \approx U_2^{\mathrm{ac}}/I_1^{\mathrm{ac}}$ for a given U_{dc}.

We measure nonlocal effects like CAR and EC in a nonlocal measurement

---

[11]The local ac voltage is first amplified with a *NF Electronic Instruments LI75A low noise preamplifier* and then measured with the lock-in amplifier. The local dc voltage is amplified with a *Stanford Research Systems SR560 low noise preamplifier* and then measured with a *Keithley Multimeter Model 2000*.

setup. This is advantageous since all *local* processes like Andreev reflection do not have an influence on U_{nl} at the detector. Otherwise, much larger local signals would mask the considerably smaller signals of the nonlocal processes. To ensure nonlocal measurements the detector needs to be out of the current path, which sets a boundary condition of a voltage measurement, namely $I_2 = 0$, see Fig. 4.5. To fulfill this, we incorporate on the detector a high input impedance of $1\,\mathrm{G}\Omega$ into our ultra-low noise preamplifier[12]. A very noise reduced preamplifier is needed to measure in the nV regime.

Possible spurious signals from effects like capacitive cross-talk, leakage currents into the detector or inhomogeneous current paths will be discussed in chapter 6.3.

---

[12] We use a *NF Electronic Instruments LI75A low noise preamplifier* where we changed in-house the input impedance from $100\,\mathrm{M}\Omega$ to $1\,\mathrm{G}\Omega$.

Chapter 5

Local measurements

5.1 Introduction

In this chapter we discuss measurements of the local two-terminal resistance and of the bias-dependent differential conductance of NIS hybrid junctions that differ in their tunneling barriers due to varying oxidation times. These local measurements allow the characterization of the tunnel junctions which will be of importance for the analysis of the nonlocal measurements discussed in chapter 6.

In earlier experiments on nonlocal subgap transport it was shown that crossed Andreev reflection (CAR) is dominated by elastic cotunneling (EC) and charge imbalance (CI) in samples without tunneling barriers [7; 9], whereas the transport characteristics of samples with low-transparent barriers can exhibit CAR in certain bias ranges [8; 10]. As the high-transparent case and the simple tunneling regime have been already investigated, we want to prepare and study intermediate transparent junctions. We will show in chapter 6 that junctions in the intermediate transparency regime with resistance area products (RA) of $\sim 10 - 100\,\Omega\mu\mathrm{m}^2$ allow to measure CAR and other interesting nonlocal processes. Another general reason for the implementation of a tunnel barrier is a suppression of the inverse proximity effect. This reduces a weakening of the superconducting properties (see chapter 2.1).

An ideal tunneling barrier is a thin (some nm) insulating layer between two metallic electrodes causing tunneling to be the only charge transport mechanism from one electrode to the other. However, in case of an inhomogeneous barrier direct connections between the electrodes can occur through

so called pinholes. Depending on their lateral size, these pinholes can change the characteristics from tunneling- to metallic-like transport with increased current density at these pinholes and thus result in an inhomogeneous current injection into the superconductor.

The chance of having tunneling barriers without pinholes is higher with thicker insulating layers (low-transparent samples). This, however, leads to small current injection into the superconductor due to the high junction resistance causing only small nonlocal signals easily below the detection limit (see chapter 6). Hence, reducing the thickness and thus the resistance of the barrier leads to more current injection, but also to an increased chance of having pinholes. This is the intermediate regime which we will study.

Here, we will first discuss the challenging preparation of the tunnel barriers and summarize the results of differently prepared junctions. In a second step we compare the differential conductance measurements of different tunnel junctions and discuss the fitting to the BTK model.

5.2 Preparation of tunneling barriers

Aluminum is chosen as the superconducting material in our devices because of its relatively high superconducting transition temperature T_C, its small spin-orbit coupling and because of the simplicity of implementing a tunneling barrier by oxidation[1]. Here, we summarize three different procedures of the oxidation process. They all have in common that they are performed either at room temperature or at roughly $80\,^\circ$C. The higher T could in principle lead to a reduction of the number of pinholes due to thermally oxidized diffusion. Within each oxidation procedure we keep T and the oxygen pressure p fix and only vary the oxidation time t_{ox}.

Most barriers are prepared with procedure 1 (black squares in Fig. 5.1) as follows: After the evaporation of Al at a substrate temperature of -50 °C, we leave the samples in UHV to warm up for approximately 15 h. Then we heat the samples for one hour with the lamp heater ($I = 1.7\,$A and $U = 2.4\,$V) to roughly $80\,^\circ$C in the load lock. Subsequently, we oxidize the Al for a time t_{ox} in pure oxygen at $p = 8$-$13\,$mbar while continuing heating.

In the second procedure (black triangle in Fig. 5.1) Al is oxidized at $p = 5 \cdot 10^{-3}\,$mbar without heating the sample, i.e. at room temperature.

The third procedure (red stars in Fig. 5.1) is equivalent to the second, but with oxidation in air.

In order to evaluate the quality of the barriers three so-called Rowell criteria exist to determine whether the transport through the insulating layer is mainly dominated by tunneling or by pinholes [78; 79]. Åkerman *et al.*

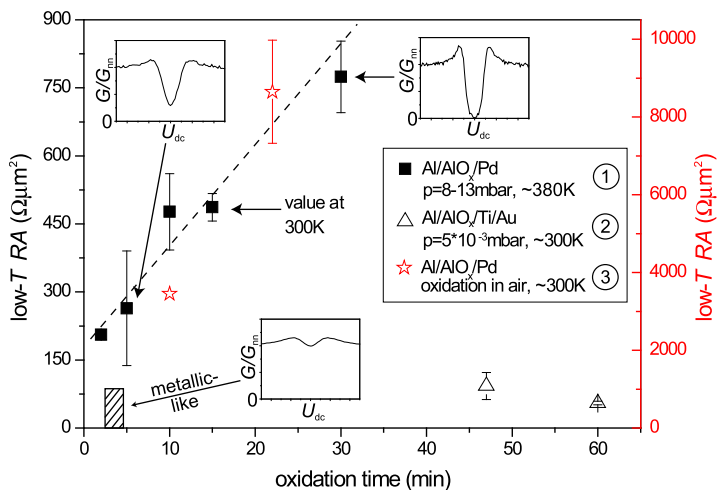[1]Al oxidizes to the insulator Aluminumoxid AlO_x.

Figure 5.1: Low temperature normal state resistance-area product RA vs. oxidation time for three different oxidation parameters. Only those junctions are chosen exhibiting insulator-like temperature dependence. For $t_{ox} = 15\,\text{min}$ only measurements at $300\,\text{K}$ were performed. The numbering in the caption refers to the preparation procedure introduced in the text. The dashed line is a guide to the eye. The black striped area shows the RA range of metallic-like barriers prepared with procedure 1. The insets show normalized differential conductance vs. bias measurements at $0.24\,\text{K}$.

show that the first two criteria, namely the exponential thickness dependence of the resistance and the non-linear current-voltage characteristics are necessary, but not sufficient criteria. However the third one, the weak insulator-like temperature dependence of the resistance, is still a sufficient criterion to rule out pinhole-dominated transport [79].

In order to test and classify the prepared junctions, we measure their resistance R at room temperature and at $1.6\,\text{K}$. Some junction resistances increase and some decrease with cooling the sample. For Fig. 5.1 we choose only those junctions showing tunneling dominated transport according to [79], namely those with insulating-like temperature dependence between 1.6 and $300\,\text{K}$. To account for different junction areas A, we determine their low-temperature $(1.6\,\text{K})$ normal state resistance area product RA. In Fig. 5.1 we plot the low-temperature RA vs. oxidation time for the three different preparation procedures. However, most samples for which we present non-

local data in chapter 6 have metallic-like junctions. Therefore, Fig. 5.1 also indicates for comparison the range of RA of these junctions which were prepared with procedure 1 (sample A and B in chapter 6.4). Besides, normalized differential conductance vs. bias measurements of samples with different oxidation times are included in Fig. 5.1 as insets. These measurements are discussed in detail in chapter 5.3.

In Fig. 5.1 we see for procedure 1 and 3 an increase of RA with oxidation time, whereas procedure 2 shows a slight decrease. The RA values of procedure 2 are two orders of magnitude smaller than 3 even though oxidizing 3-4 times longer. In the same range of t_{ox} procedure 1 exhibits one order of magnitude smaller RA than 3. As indicated with the dashed line in Fig. 5.1, we obtain for procedure 1 a linear increase of the RA with the oxidation time for $t_{ox} > 2 \, \mathrm{min}$.

In the discussion of these results we interpret the larger RA with longer t_{ox} for procedures 1 and 3 in such a way that a thicker insulating AlO_x can form. As RA is basically a measure of the mean transparency[2] of a junction, a thicker insulating layer leads to less transparent tunnel junctions. Since in procedure 2 the oxygen pressure is 6 orders of magnitude smaller than in 3, samples oxidized at such low pressures probably need longer oxidation times to achieve a considerable change of RA and therefore in the transparency. We conclude that the oxygen pressure is a parameter that accelerates the oxidation process and leads to less transparent tunnel junctions.

From Fig. 5.1 we cannot draw conclusions about the influence of the sample heating on the oxidation since also p varies significantly between different procedures. However, we want to mention for completeness that we have also prepared barriers with $10 \, \mathrm{min}$ oxidation time at low T, namely at a sample temperature of $-50 \, °\mathrm{C}$ and $p = 0.5 \, \mathrm{mbar}$ (not shown in Fig. 5.1). As all junctions exhibited low barrier resistances, we did not cool them to test if they show insulating-like temperature dependence of the resistance.

The transport of the metallic-like junctions shown in Fig. 5.1 is dominated by pinholes. Thus, these barriers exhibit considerably lower RA values than the corresponding insulating-like junctions.

5.3 Barrier characterization

In the last chapter we have discussed different procedures to prepare tunnel barriers and how to classify them into insulator- and metallic-like junctions. For a more detailed characterization of the junctions we perform superconducting tunneling spectroscopy (STS) as discussed in chapter 1.2 and 4.6.

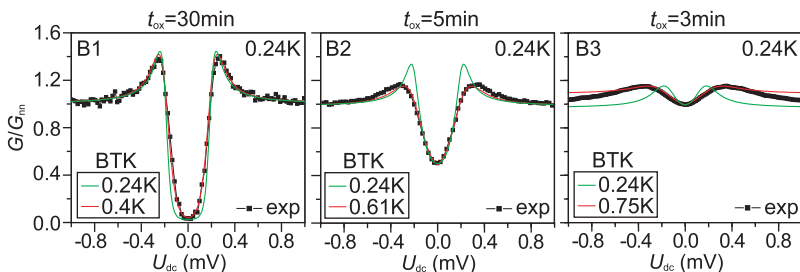[2]Higher RA values indicate less transparent junctions.

Figure 5.2: Comparison of normalized conductance vs. bias measurements of three tunnel junctions B1, B2 and B3 at 0.24 K. The barriers were prepared with different oxidation times t_{ox} indicated in the figure. Each measurement is fitted twice (red and green) to the BTK model with additional broadening. In green T is fixed, whereas in red T is a fitting variable. For parameter details see Table 5.1.

We have learned from Fig. 5.1 that RA increases with longer oxidation time when keeping all other parameters fix. In order to understand the influence of the oxidation we study in Fig. 5.2 the bias dependent normalized differential conductance at 0.24 K for three typical barriers prepared with procedure 1 (see chapter 5.2) and oxidation times of 3, 5 and 30 min. Junction B1 with $t_{ox} = 30$ min exhibits a well resolved superconducting density of states (see chapter 1.2) with nearly no subgap conductance and conductance peaks at $U_{dc} = \pm 0.25$ mV. With shorter oxidation time (B2 and B3) the subgap conductance increases successively. Moreover, the conductance peaks broaden with their maximum at higher bias voltages, see Fig. 5.2.

Fitting the results of the G/G_{nn} vs. bias characteristics to the BTK model (see [26] and chapter 2.1) gives further insights into the barrier properties e.g. with the barrier strength Z. For the fits of Fig. 5.2 we included an additional broadening parameter Δ_2 [80; 81] into the BTK model such that the gap parameter Δ is replaced by $\Delta - i\Delta_2$. Physically, the parameter Δ_2 describes the quasiparticle lifetime broadening [80]. In Fig. 5.2 we always perform two fittings (green and red). In both cases we use the barrier strength Z and the broadening Δ_2 as fit parameter while keeping the energy gap Δ and the resistance R constant. In the green fitting we fix the temperature at 0.24 K, whereas in the red case T is an additional fitting parameter. For details see Table 5.1. It is apparent in Fig. 5.2 that the red fittings coincide better with the experimental data than the green ones. When comparing the fitting parameters successively from B1 to B3 (see Table 5.1), we find with shorter oxidation time smaller Z and larger broadening Δ_2 and in case of the red

Table 5.1: Supplementary data to the BTK fits in Fig. 5.2 with T: temperature; Z: BTK barrier strength; Δ: superconducting energy gap; Δ_2: broadening parameter; R: normal state resistance at 1.6 K. Fitting parameters of green: Z, Δ_2. Fitting parameters of red: Z, Δ_2 and T. The other parameters are fixed.

	B1		B2		B3	
	green	red	green	red	green	red
T [K]	0.24	0.4	0.24	0.61	0.24	0.75
Z	4.5	4.5	0.94	1.05	0.55	0.62
Δ [μeV]	190	190	190	190	190	190
Δ_2 [μeV]	30	0	30	30	80	100
R [kΩ]	13.1	13.1	2.64	2.64	1.29	1.15

fitting larger T.

   From the results presented above we conclude that shorter oxidation times lead to thinner insulating layers. This causes lower barrier resistances R (see Table 5.1 and chapter 5.2) assuming similar junction areas. We exhibit that B1 with longest t_{ox} is a low-transparent junction as it has a large barrier strength ($Z = 4.5$) and low subgap conductance. From the insulator-like characteristics we conclude tunneling dominated transport and a negligible amount of pinholes (chapter 5.2).

   With shorter t_{ox} (B2 and B3), we obtain thinner AlO$_x$ layers and enter the intermediate transparency regime in which B2 and B3 show metallic-like behavior. This indicates inhomogeneous insulating layers possibly with pinholes. The inhomogeneities lead to higher transparent areas in the barrier which dominate the transport behavior across the junction. In the following we refer to these higher transparent barrier regions as pinholes. These pinholes allow more Andreev reflection that leads to an enhanced subgap conductance and lower barrier strengths Z (see chapter 2.1) as observed in experiments (see Fig. 5.2) and theory (see Table 5.1). As the junction resistance decreases with thinner barriers, the current density increases leading to more possible heating of the superconductor. The heating might be locally enhanced as the current density is largest at the pinholes. However, heating due to thinner insulating layers might explain why the red fittings with using an increased T coincide better with the experimental data than green (see Fig. 5.2). The variable T increases successively from B1 to B3 (see Table 5.1) thus indicating a thinner insulating layer with possibly more pinholes in B3. Heating effects might explain the broadened features in Fig. 5.2 and the larger values of the broadening parameter (Table 5.1) for B2 and B3. This is consistent with Dynes *et al.* [80] where higher T leads to larger broadening parameters. However, the better fitting of red might not have

a physical reason, but could be simply based on the fact that red has three instead of two fitting parameters. Naturally this allows better fitting.

It is important to note that we do not see a reduction of the superconducting energy gap Δ (see Table 5.1) even though the barriers contain pinholes in the intermediate transparency regime (B2 and B3). We observe for Δ the expected Al bulk value of $190\,\mu$eV. Hence, the pinholes do not alter the superconducting properties considerably by the inverse proximity effect or by possible current induced heating. This is supported by the fact that we do not see a reduction of T_C in contrast to what is reported in similar devices with high-transparent junctions [9].

5.4 Summary and conclusion

We have shown that it is possible to prepare tunnel barriers by oxidation of Al. We have studied different preparation procedures with the oxidation time, oxygen pressure and substrate temperature as variable parameters and classified the prepared junctions by temperature dependent normal state resistance measurements into insulator- and metallic-like samples. This indicates on the basis of the third Rowell criteria [78; 79] whether the transport across the junction is tunneling or pinhole dominated. We find for those junctions exhibiting tunneling dominated transport a linear dependence of the oxidation time and the resistance area product (RA). Hence, longer oxidation leads to thicker insulating layers and thus to larger RA corresponding to less transparent junctions.

As we want to study the nonlocal transport in the intermediate transparency regime, we find that in our junctions the transport might be pinhole dominated due to thinner and inhomogeneous insulating layers. Pinhole dominated transport is indicated by metallic-like behavior and a RA ($\sim 10-100\,\Omega\mu$m^2) considerably lower than those of tunneling dominated junctions.

For a more detailed barrier characterization we performed superconducting tunneling spectroscopy. These results show that with shorter oxidation time and therefore thinner barriers the resistance decreases, the subgap conductance increases and the conductance peaks at the gap edges broaden. Fitting to the BTK model gives equivalent results. Shorter oxidation times lead to smaller barrier strengths Z and larger broadening parameters Δ_2. This is the case especially for pinhole dominated junctions. We obtain better fits to our experimental data if we assume higher temperatures. This might indicate current induced heating due to the higher current density in higher-transparent junctions. However, this possible heating does not lead to considerable changes in the superconducting properties as we do not see

changes in the gap parameter and in the critical temperature.

The goal are tunneling dominated junctions in the intermediate transparency regime. Then, due to the absence of pinholes the current injection into the superconductor is homogeneous. This simplifies a theoretical description as local heating and possible local changes in the superconducting properties are reduced. To increase the yield of these homogeneous junctions, the next step could be to lengthen the oxidation time and coincidentally reduce the oxygen pressure to give the AlO_x barrier more time to form a homogeneous layer. A decreased substrate temperature will most likely achieve the same, but the oxygen atoms would have less energy to diffuse and find a potential minimum which would be unfavorable. Further investigation is needed for an optimized barrier fabrication process.

Chapter 6

Nonlocal measurements

In this chapter we will discuss our results obtained with nonlocal measurements on multi-terminal NIS hybrid devices. First, a literature overview on nonlocal measurements of crossed Andreev reflection (CAR), elastic cotunneling (EC) and nonlocal charge imbalance (CI) is given. Then, we will discuss how to distinguish these possible nonlocal processes in such structures. Since spurious effects can resemble the expected nonlocal characteristics, we will also present a set of necessary measurements to rule out false interpretations.

The discussion of our results will be separated in three parts. The first part will focus on CAR and EC and the dependence on the contact resistances. The second will deal with the magnetic field dependence of CAR and nonlocal CI. In the last part we will only focus on nonlocal CI and will present a universal nonlocal resistance independent of the contact resistances.

6.1 Current status of experiments on crossed Andreev reflection, elastic cotunneling and nonlocal charge imbalance

This chapter gives a literature review on the current experimental status on CAR, EC and CI in metallic hybrid structures. The experiments similar to those presented in this thesis can be divided into two groups, namely those with high-transparent NS contacts and those with low transparent NIS tunnel junctions.

After the first experimental report of CAR in 1995 by Byers and Flatté [6],

Beckmann *et al.* published in 2004 their work on nonlocal, high-transparent metallic spin-valve samples in a similar geometry as shown in Fig. 4.5 [7]. With Al as superconductor and Fe as ferromagnetic injector and detector, Beckmann *et al.* observed nonlocal subgap transport and were able to distinguish CAR and EC by spin-selective contacts. They measured the nonlocal resistance R_{nl} with parallel and antiparallel magnetization alignment of the ferromagnetic electrodes and concluded from $\Delta R_{\mathrm{nl}} = R_{\mathrm{nl}}^{(\uparrow\uparrow)} - R_{\mathrm{nl}}^{(\uparrow\downarrow)} > 0$ that EC dominates over CAR for all temperatures and biases. The fact that the dependence of ΔR_{nl} on the injector-detector distance d was different for $T < T_C$ and $T > T_C$ and that at base temperature the magnitude of ΔR_{nl} decays on a length scale of ξ let them conclude to have measured nonlocal, coherent second order processes CAR and EC. However, due to the high transparency of the contacts, the small signals due to CAR and EC were superimposed on a much larger charge imbalance (CI) signal.

Cadden-Zimansky *et al.* studied nonlocal correlations in NS hybrid systems comparable to the ones shown in Fig. 4.5 with high-transparent Au/Al-interfaces [9]. They showed that it is possible to distinguish EC and CAR from CI by the different characteristic decay lengths. The authors could extract the decay lengths of CAR and EC, which is different to the one of CI. As in [7] EC was the dominant subgap transport mechanism in the high-transparent devices.

Very recently Cadden-Zimansky *et al.* published experimental evidence for the coherent, nonlocal coupling of two electrons spatially separated in two normal leads [11]. This coupling is mediated by CAR and EC processes in the superconductor. The measurement is based on a high-transparent NSN device similar to the one shown schematically in Fig. 4.5 with an injector-detector distance $d \leq \xi$, but with an additional hybrid NS loop (Andreev interferometer) attached to the injector. By changing the magnetic flux through this loop, the phase of the electrons in the normal metal of the injector and therefore the resistance of the Andreev interferometer changed periodically with the superconducting flux quantum $\Phi_0 = h/2e$. Cadden-Zimansky *et al.* showed that these differential resistance oscillations also appear in the nonlocal differential resistance R_{nl} at the detector, which could only be mediated by phase-coherent processes like CAR or EC. This interpretation is supported by the fact that the magnitude of R_{nl} was considerably attenuated at the detector which is expected for nonlocal signals like CAR and EC.

Russo *et al.* investigated 3-terminal vertical Nb/Al multilayer structures with low-transparent barriers [8]. In contrast to other experiments in this field, they used a different geometry with large area tunnel junctions ($4 \times 8\,\mu\mathrm{m}^2$) and Nb as superconductor instead of Al. They could show that the occurrence of EC and CAR is energy dependent with EC dominating

at low and CAR at high subgap bias. The crossover energy is interpreted as given by the Thouless energy $E_T = \hbar D/d^2$, an indicator for phase coherence across the sample. In these experiments the nonlocal signals decayed with temperature, injector-detector distance and applied magnetic field. For this special geometry the results were modeled by Levy Yeyati *et al.* [47]. The authors include electron-electron interactions by charging effects on the small junctions and an electromagnetic coupling between the contacts and obtain a reasonable agreement with the experimental results of [8].

In 2007 Beckmann *et al.* published results of four-terminal, local measurements obtained on spin-valve samples with low-transparent interfaces [10]. Two of three different Fe/Al structures with antiparallel magnetization alignment of the injector and detector electrode showed that CAR is dominant for subgap energies. For the other sample Beckmann *et al.* obtained similar results as Russo *et al.* [8] with EC dominant at low bias and CAR dominant at higher bias.

In summary, we can group the experiments into two categories: EC and CI dominate the subgap transport in devices with highly transparent contacts [7; 9], whereas CAR is more prominent in samples with lower transparencies. This CAR dominance is dependent on the bias [8; 10]. These individual findings suggest that the contact resistance plays a significant role in determining which process is dominant.

In this thesis we demonstrate the strong dependence of CAR on the contact resistance. We discuss dynamical Coulomb blockade (DCB) as possible source of these findings as it is an important mechanism that lifts the balance between CAR and EC. In contrast to [10] we do not use ferromagnets, but normal metal contacts. This denotes a simpler system as we can neglect the influence of the relative magnetization alignment, possible spurious magnetic stray fields and spin accumulation. Furthermore, we show the characteristics of our injector and detector and give the R_{nl} values for all samples to allow a comparison.

6.2 The distinction of different nonlocal processes

It was discussed in chapter 2 and shown in experiments [7; 8; 9; 10] on NS and NIS structures similar to those investigated in this thesis, that CAR, EC and nonlocal CI can contribute to U_{nl} with similar strength. Thus, it is necessary to establish a procedure to distinguish these processes. The different possibilities are summarized in Table 6.1 and will be discussed below.

In a CAR process a particle is injected from N1 and one of opposite charge is generated in N2. In Fig. 6.1(a) such a process is shown schematically for
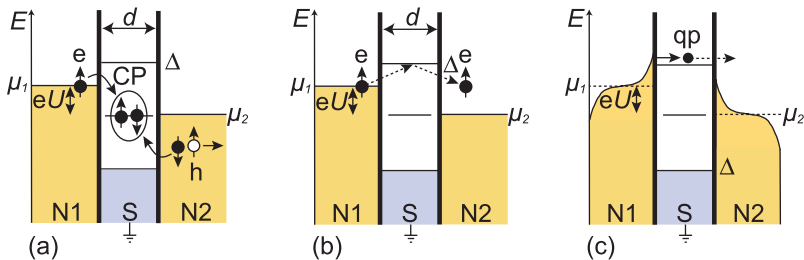
Figure 6.1: Schematic of (a) crossed Andreev reflection; (b) elastic cotunneling and (c) charge imbalance

$U < 0$, where electrons are injected from N1 and holes are created in N2. For each U a potential of *opposite* sign builds up on N2 to ensure the zero current boundary condition ($I_2 = 0$) of an ideal voltage measurement. In EC and CI processes, however, the charges on the injector and detector have the same sign (see Fig. 6.1(b) and Fig. 6.1(c)) and U_{nl} has the same polarity as the bias. This means that for an applied bias $U < 0$ the nonlocal resistance R_{nl} is negative for CAR and positive for EC and CI. As a negative R_{nl} is unique, this is the most important indication for CAR dominated subgap transport, see Table 6.1.

Theoretically predicted and experimentally shown, the probability of CAR and EC decreases with rising T due to thermal smearing of the Fermi function (CAR: $dR_{\mathrm{nl}}/dT > 0$; EC: $dR_{\mathrm{nl}}/dT < 0$) [7; 8; 47]. Nonlocal CI signals, however, increase with rising T ($dR_{\mathrm{nl}}/dT > 0$) [7; 9] due to a reduced superconducting energy gap $\Delta(T)$ and a broadened thermal distribution and exhibit a characteristic peak at T_{C}.

As was suggested in [7; 9], distance dependent measurements allow to distinguish CAR and EC from CI. This is based on the prediction that CAR and EC decay on length scales given by the superconducting coherence length ξ, while charge imbalance decays on the scale of the considerably larger CI length Λ^{*}[1].

In case of ferromagnetic contacts the relative alignment of the magnetization orientation allows a distinction between CAR and EC. As is explained in chapter 2.2.1, parallel magnetization alignment favors EC while the antiparallel case favors CAR [7; 27].

---

[1] The charge imbalance length Λ^{*} refers to quasiparticles propagating above the gap. However, quasiparticles can also enter the superconductor at subgap energies into evanescent states which decay on a length scale of the superconducting coherence length ξ.

Table 6.1: Summary of possible parameters enabling to distinguish crossed Andreev reflection (CAR), elastic cotunneling (EC) and nonlocal charge imbalance (CI).

	sign of R_{nl}	T-dep	decay length of $U_{nl}(d)$	spin sensitive	$H_{\|\|}$-field dep. for $H << H_C$
CAR	< 0	$\frac{dR_{nl}}{dT} > 0$	ξ	$\uparrow\downarrow$	no
EC	> 0	$\frac{dR_{nl}}{dT} < 0$	ξ	$\uparrow\uparrow$	no
CI	> 0	$\frac{dR_{nl}}{dT} > 0$, peak at T_C	$\Lambda^* >> \xi$	no	$\frac{dR_{nl}}{dH} < 0$

A novel tool to distinguish CAR and EC from CI is a magnetic field applied in-plane and parallel to the superconducting wire. CI decreases with applied magnetic fields considerably smaller than the critical field H_C, whereas CAR and EC are robust in this magnetic field regime. For details of this surprising result see chapter 6.5.

The first two criteria, namely the sign of R_{nl} and its temperature dependence, are sufficient to distinguish the three processes and will be used for the interpretation of our measurements.

Other possible sources for nonlocal signals e.g. leakage currents or inhomogeneous current paths will be discussed and excluded in the following chapter.

6.3 The exclusion of spurious nonlocal signals

We perform nonlocal ac measurements using lock-in amplifiers at a frequency of ∼10 Hz. Since the junction resistances vary strongly with the applied bias, leakage currents and capacitive cross-talk e.g. between the injecting and detecting contact or between the structure and the substrate can produce spurious nonlocal signals which might resemble the expected characteristics. As the injector and detector are only 50-200 nm apart, inhomogeneous current paths (schematically shown in Fig. 6.3(b)) and generally leakage currents into the detector can also cause nonlocal signals. Consequently, it is necessary to discuss these spurious effects and find a way to prevent and distinguish them from the signals of CAR, EC and CI. For trustworthy nonlocal measurements one should consider the following:

- We minimize dc leakage currents into the detector N2 by using a voltage amplifier with $1\,G\Omega$ input impedance. To neglect dc leakage, it is

necessary to show for each device that changing the input impedance to $100\,\mathrm{M\Omega}$ has no effect on the results.

- We test each device for ac leakage currents by changing the measurement frequency. In case of considerable cross-talk and thus large ac leakage currents, U_{nl} changes with frequency. In good samples as shown in Fig. 6.2(a) the in-phase part of U_{nl} does not change with frequency, while the capacitive part Y_{nl} is constant and considerably smaller than U_{nl}. Moreover, it is possible to check for ac leakage by measuring U_{nl} simultaneously in a dc configuration. Since dc measurements ideally do not exhibit cross-talk, the nonlocal voltage obtained in ac- and dc-configuration can only coincide if cross-talk is negligible for the ac-measurement. This is the case for our results, e.g. shown in Fig. 6.2(b) for sample A (see chapter 6.4). For Fig. 6.2(b) we measure U_{nl} in a dc configuration with $10\,\mathrm{s}$ delay between points, determine the slope and finally calculate R_{nl}. However, a disadvantage of the dc-measurements is the worse signal-to-noise ratio. A way to model capacitive cross-talk is shown in Appendix A.

- For all devices the nonlocal signals should vanish for $T > T_{\mathrm{C}}$, see Fig. 6.3, implying that they are related to the superconductor and not to the measurement setup or inhomogeneous current paths. As we do not expect the latter to be related to T_{C}, we can exclude this spurious effect.

During this thesis several samples have exhibited spurious effects mentioned above. Therefore it is required for nonlocal measurements to care-
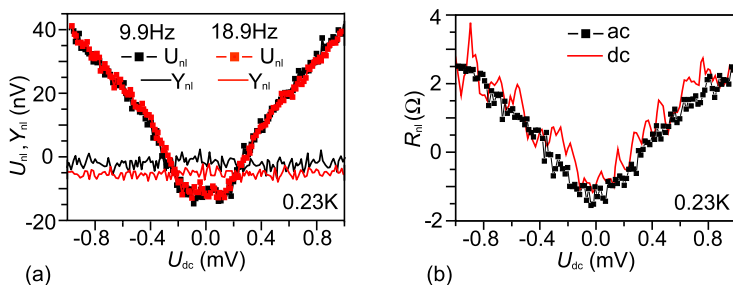

Figure 6.2: (a) Frequency dependence of the in-phase nonlocal signal U_{nl} and the capacitive part Y_{nl} at $0.23\,\mathrm{K}$ (b) Comparison between R_{nl} vs. bias results measured in ac- and dc-configuration at $0.23\,\mathrm{K}$.
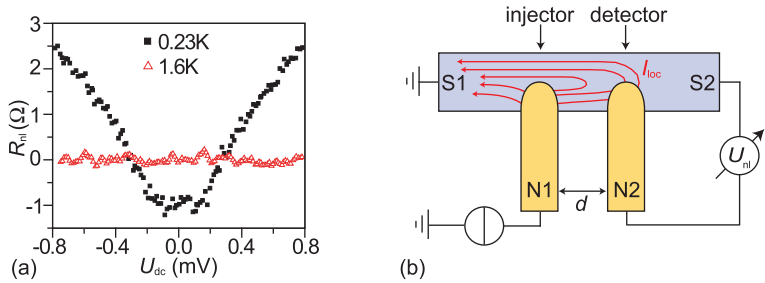
Figure 6.3: (a) R_{nl} vs. bias measurement below and above T_C. Above T_C all nonlocal signals vanish. (b) Schematic of inhomogeneous current paths possibly causing nonlocal voltages.

fully check each device for leakage currents and capacitive cross-talk. In summary, in order to trust nonlocal results the in-phase part of U_{nl} should be independent of frequency with a comparably small and constant quadrature part. Additionally, the nonlocal signals should vanish above T_C and should not show a dependence on varying high-ohmic input impedances on the detector. For all samples shown in this thesis these criteria are fulfilled.

6.4 Contact resistance dependence of crossed Andreev reflection

6.4.1 Introduction

In this chapter we will present four-terminal nonlocal experiments on three samples of similar geometry but with injecting and detecting NIS junctions of different resistances. We will demonstrate that in a small window of contact resistances CAR can dominate the nonlocal transport for all subgap bias voltages at low temperatures, and that CAR is suppressed for larger barrier resistances, leading to a qualitative change of the shape of the nonlocal transport characteristics. We will interpret our results qualitatively in terms of dynamical Coulomb blockade (DCB).

6.4.2 Sample characterization

The results of this chapter are obtained on three planar multi-terminal hybrid devices A, B and C. Before discussing and comparing the nonlocal re-
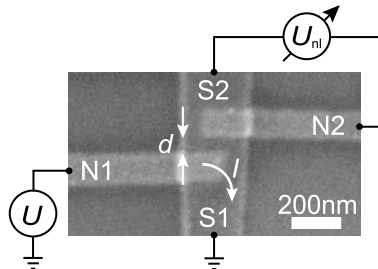
Figure 6.4: SEM image of a typical sample. A current I is applied between normal contact N1 and the superconducting contact S1, while the nonlocal voltage U_{nl} is detected between N2 and S2.

sults of each sample, it is necessary to characterize each sample thoroughly to allow conclusions on possible parameters influencing the nonlocal transport behavior. Sample A, B and C are different due to variations in the barrier preparation, which we briefly discuss at the beginning, followed by a characterization of the superconducting Al from which we e.g. extract the superconducting coherence length.

The devices discussed here are $Pd(30\text{-}40\,nm)/AlO_x/Al(50\,nm)$ samples, see Fig. 6.4 and are prepared on thermally oxidized Si wafers by e-beam lithography and angle-evaporation in ultra-high vacuum with a base pressure of $< 5 \cdot 10^{-10}$ mbar. For details of the fabrication process we refer to chapter 4.5. Sample A, B and C differ in the oxidation time of the Al. In order to have devices with varying barrier transparency (see chapter 5.2), we oxidize sample A and B for 3 min and C for 5 min with a sample temperature of approximately 80 °C in an oxygen atmosphere of 12 mbar. This leads to different normal resistances of the injecting (i) and detecting (d) junction, R_i and R_d, at 1.5 K and the corresponding resistance area products $R_i A_i$ and $R_d A_d{}^2$. We find an increase of R and RA from sample A to C as summarized in Table 6.3.

We determine several electronic Al properties in each sample by resistance measurements and find consistently a superconducting transition temperature $T_C \approx 1.2\,K$ and a resistivity $\rho_{Al} = 1.2 - 2.6\,\mu\Omega cm$ of the Al strip at $T = 4.2\,K$. With $N_{Al} = 2.4 \cdot 10^{28}\,1/eVm^3$ as density of states of Al at the Fermi energy and σ_{Al} the conductivity of the Al strip, we calculate the electron diffusion constant $D = \sigma_{Al}/e^2 N_{Al}$. For samples A-C we find $D = 9.9 - 21.7 \cdot 10^{-3}\,m^2/s$ at 4.2 K, which corresponds to an elastic mean free

---

[2]The junction area A is estimated from scanning electron microscope images.

Table 6.2: Aluminum properties of sample A, B and C. t_{ox}: oxidation time; ρ_{Al}: specific resistance of Al at 4.2 K; D: diffusion constant at 4.2 K; ℓ_{el}: elastic mean free path of the Al strip at 4.2 K; ξ: superconducting coherence length; Δ^*: characteristic energy of the injector

	t_{ox} [min]	ρ_{Al} [$\mu\Omega$cm]	D x10^{-3} [m^2/s]	ℓ_{el} [nm]	ξ [nm]	Δ^* [meV]
A	3	2.6	9.9	23	184	0.29
B	3	2.5	10.5	24	189	0.26
C	5	1.2	21.7	50	273	0.32

path of $\ell_{el} = 3D/v_F \approx 20 - 50$ nm ($v_F = 1.3 \cdot 10^6$ m/s). Furthermore, we use the BCS coherence length $\xi_0 = \hbar v_F / \pi \Delta(0)$ to extract the superconducting coherence length of a superconductor in the dirty limit ($\ell_{el} << \xi_0$) with the relation $\xi \cong \sqrt{\xi_0 \ell_{el}}$. We get $\xi \approx 180 - 270$ nm at cryogenic temperatures. We define the characteristic energy Δ^* which denotes the bias potential of maximum conductance of the injector contact, see Fig. 6.5(c), 6.6(b), 6.7(b). We note that $\Delta^* \neq \Delta_{BCS}$. The details of the Al properties of each device are summarized in Table 6.2.

In our Pd/AlO$_x$/Al-samples we obtain edge-to-edge distances d between the injecting and detecting electrodes of $\sim 50 - 220$ nm and junction areas of $\sim 0.03\,\mu$m^2, which corresponds to ~ 0.5 fF junction capacitance in a plate capacitor model[3] and results in a single electron charging energy $E_C = e^2/2C \approx 0.13$ meV. As discussed in chapter 2.2 the nonlocal signal theoretically decays $\propto e^{-d/\xi}$. As for all discussed samples $d < \xi$ (see Table 6.3), we conclude that our devices are theoretically in a regime where we are able to measure nonlocal signals of CAR and EC.

An SEM image of a typical sample with a schematics of the measurement is shown in Fig. 6.4. In our four-terminal nonlocal measurement we inject a current I from the normal contact N1 to the superconducting contact S1 while detecting the nonlocal voltage U_{nl} between N2 and S2. The details of our measurement setup are discussed in chapter 4.6.

On the basis of chapter 6.3 we have tested sample A, B and C for spurious nonlocal signals due to leakage currents, capacitive cross-talk and inhomogeneous current paths. We conclude that in these samples spurious nonlocal signals are negligible.

---

[3] We use for the plate capacitor model $C = \epsilon_0 \epsilon_r \frac{A}{d_c}$ with the relative permittivity $\epsilon_r = 7$ for AlO$_x$, junction area $A = 0.03\mu$m^2 and an estimated AlO$_x$ thickness $d_c = 3$ nm.

6.4.3 Results

As the data of the three samples A, B and C show a systematic change, we will describe first all data sets before discussing them. The Al properties of each sample are given in Table 6.2, whereas Table 6.3 summarizes parameters related to the NIS junctions.

Sample A

Figure 6.5(a) shows for sample A R_{nl} as a function of the bias voltage U_{dc} at various temperatures with N1 as injector and N2 as detector. At base temperature we observe a negative nonlocal resistance R_{nl} for all subgap volt-

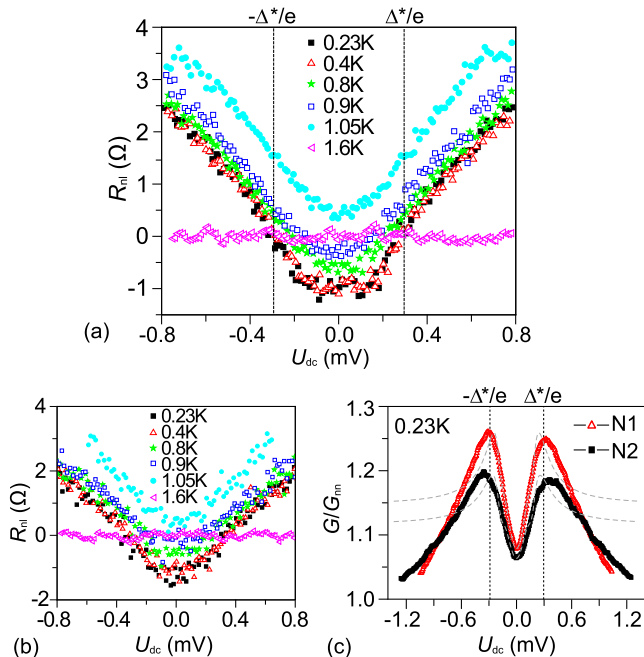**Figure 6.5:** Results of sample A. (a) R_{nl} vs. bias for various temperatures with N1 as injector and N2 as detector. (b) Temperature dependent R_{nl} vs. bias measurements with N2 as injector and N1 as detector. (c) STS characterization of contacts N1 and N2 at 0.23 K. The grey dashed lines are fits to the BTK model. The black dashed lines label the bias corresponding to Δ^* of the injector N1.

Table 6.3: Properties of samples A, B and C. ξ: superconducting coherence length; R_i, R_d: injector and detector barrier resistance at $T = 1.5\,\text{K}$; Z_i, Z_d: BTK barrier strength of the injector and detector; d: injector-detector distance; $R_i A_i$, $R_d A_d$: normal state resistance area product of the injector and detector; asymmetry $\alpha = (R_d A_d - R_i A_i)/(R_d A_d + R_i A_i)$.

	ξ [nm]	R_i [kΩ]	R_d [kΩ]	Z_i	Z_d	d [nm]	$R_i A_i$ [$\Omega\mu m^2$]	$R_d A_d$ [$\Omega\mu m^2$]	α
A	184	0.4	0.5	0.59	0.59	55	8.5	16.9	0.33
B	189	0.8	5.5	0.60	0.68	155	22.1	93.5	0.62
C	273	2.6	11.2	0.94	1.45	220	116.6	365.4	0.52

ages with $R_{nl} \approx -1.0\,\Omega$. This value does not change with temperature up to $T \approx 0.5\,\text{K}$. When increasing T further R_{nl} increases and becomes positive for $T \geq 1.05\,\text{K}$. For voltages larger than Δ^*/e, R_{nl} is positive at all temperatures and increases with T. At $1.6\,\text{K}$, i.e. for $T > T_C$, $R_{nl} \approx 0$ for all biases. For the results of Fig. 6.5(b) we swap the contacts, using N2 as injector and N1 as detector[4] and measure temperature dependent R_{nl} as a function of the bias voltage U_{dc}. The results are very similar to those of Fig. 6.5(a) with the same negative R_{nl} value at zero bias which increase with T and becomes positive above $1.05\,\text{K}$. For large bias R_{nl} exhibits slightly smaller values compared to the other injector-detector configuration. The contact characterization of sample A at base temperature is shown in Fig. 6.5(c) and exhibits a significant subgap conductance for both, N1 and N2. The dashed lines represent the bias corresponding to the energy Δ^* of the injector N1, which coincides with the sign change of R_{nl}, see Fig. 6.5(a). Also in the swapped configuration for N2 as injector the bias Δ^*/e of maximum conductance (not indicated in Fig. 6.5(c)) coincides with the R_{nl} sign change in Fig. 6.5(b). Within the energy gap both barriers exhibit nearly the same normalized conductance values and both contacts have similar resistances above T_c, $0.4\,\text{k}\Omega$ and $0.5\,\text{k}\Omega$. In addition Fig. 6.5(c) shows fits of the BTK model [26] to the conductance spectra including an additional broadening parameter [80; 81] as discussed in chapter 5.3. We use the barrier strength Z (given in Table 6.3) and the broadening parameter for fitting while keeping T and Δ constant. We find good agreement with the BTK model for energies below the gap Δ. For larger applied potentials the data are not well reproduced.

---

[4]When swapping N1 and N2, also contact S1 and S2 are swapped.

Sample B

In Fig. 6.6(a) the bias dependence of R_{nl} of sample B is plotted for several temperatures with N1 as injector and N2 as detector. The shape and amplitudes of the curves are very similar to those of sample A in Fig. 6.5(a) and (b), as is the temperature dependence. However, in sample B at base temperature we observe a local maximum for $U_{dc} \approx 0$ with $R_{nl} \approx 0$, whereas for finite subgap biases we find $R_{nl} < 0$ with two minima of $R_{nl} \approx -1.1\,\Omega$ at $U_{dc} \approx \pm 0.135\,\text{mV}$. Above T_C the nonlocal signals vanish for all bias voltages. Figure 6.6(b) shows the STS characterization of the individual contacts at 0.23 K. In contrast to sample A, the normalized injector and detector conductances differ considerably in the gap and are smaller than in sample A ($R_i = 0.8\,\text{k}\Omega$ and $R_d = 5.5\,\text{k}\Omega$). The fitting to the BTK model shows good agreement within the superconducting gap, but differs for larger bias. We have also swapped the injector and detector and measured the nonlocal voltage. Due to the large injector resistance of N2 the injected current and thus the nonlocal signals were too small.
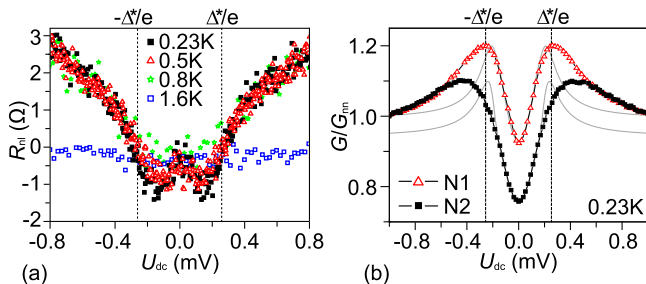

Figure 6.6: Results of sample B. (a) R_{nl} vs. bias at various T with N1 as injector and N2 as detector. (b) STS characterization of N1 and N2 at 0.23 K. The grey lines are fits to the BTK model. The dashed lines indicate the bias corresponding to Δ^* of the injector.

Sample C

Bias dependent measurements for sample C are shown in Fig. 6.7(a). At base temperature a prominent local maximum in the middle of the superconducting gap develops with a *positive* maximum of $R_{nl} \approx 30\,\Omega$. For $0.13\,\text{mV} \leq |U_{dc}| \leq \Delta^*/e$ with $\Delta^* \approx 0.31\,\text{meV}$, R_{nl} is negative with minima at $\pm 0.23\,\text{mV}$ with $R_{nl} \approx -13\,\Omega$. The sign changes at $U_{dc} \approx \pm 0.13\,\text{mV}$, inde-
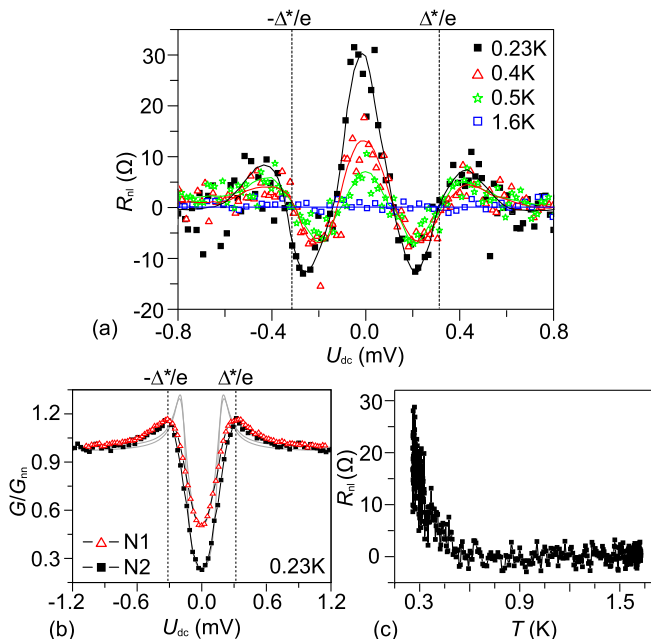
Figure 6.7: Results of sample C. (a) R_{nl} vs. bias for various T with N1 as injector and N2 as detector. The solid lines are guides to the eye and the dashed lines show the voltage corresponding to Δ^* of the injector. (b) STS-measurements of contact N1 and N2 at $0.23\,$K. The grey lines are fits to the BTK model. (c) R_{nl} at zero bias as a function of T.

pendently of temperature. For $|U_{dc}| > \Delta^*/e$ the signal is positive and tends to zero for increasing bias, in contrast to samples A and B. With increasing temperature all nonlocal signals tend to zero, independently of the bias, with $R_{nl} \approx 0$ for $T > T_C$. At zero bias the signal decreases monotonically with increasing T and vanishes already for $T > 0.5\,$K, see Fig. 6.7(c). A finite nonlocal signal only develops for T well below T_C. From the STS measurements shown in Fig. 6.7(b) we find that the two contact resistances are quite different and much larger than in the previous samples ($R_i = 2.6\,$kΩ and $R_d = 11.2\,$kΩ). The fitting to the BTK model coincides well within the energy gap and at large bias, but deviates for bias potentials around the gap value. As for sample B we have also measured the nonlocal voltage with
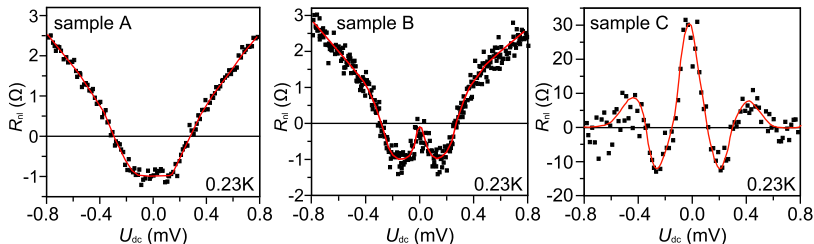
Figure 6.8: Comparison of the R_{nl} vs. bias characteristics of sample A, B and C at $0.23\,K$. The red line is a guide to the eye.

swapped injector-detector configuration. Due to the large injector resistance of N2 the nonlocal signals were too small.

For comparison we summarize the R_{nl} vs. bias characteristics at base temperature for sample A, B and C in Fig. 6.8. In the midgap regime a systematic increase to a positive maximum of the nonlocal signal is clearly visible.

6.4.4 Discussion

In the discussion of the presented data we will mainly focus on the systematic evolution of R_{nl} at zero bias from sample A to C. First we will identify which processes are dominant depending on the bias. Afterwards we will discuss the parameters that might determine the successive change in R_{nl}. Based on this, we will suggest a qualitative explanation.

As was discussed in chapter 6.2 we interpret $R_{nl} < 0$ in the superconducting energy gap as CAR being the dominant process, while $R_{nl} > 0$ is attributed to EC or CI. The latter two processes can be distinguished by the temperature dependence of R_{nl} at a given bias. EC and CAR are reduced with increasing temperature [8; 47], while CI increases strongly up to T_C due to the decreased superconducting energy gap and the broadened thermal distribution, and vanishes for $T > T_C$ [9]. At zero bias and low enough temperatures CI can be neglected.

For sample A we conclude that CAR is the dominant nonlocal transport process at base temperature and at all subgap biases. From the characteristic strong increase of R_{nl} to positive values with T, we conclude that nonlocal CI becomes important for $T > 0.5\,K$. These findings also apply for sample B, except around zero bias, where CAR and EC approximately compensate

each other at low temperatures. At finite subgap bias, EC is weakened as reported in [8] and the characteristics become similar to sample A. In sample C, EC not only compensates CAR, but even dominates the nonlocal midgap transport. As in A and B, CAR dominates at finite subgap bias. In all samples CI dominates for bias potentials above the energy gap. In contrast to the first two samples, CI is strongly suppressed in sample C for $|U_{\mathrm{dc}}| >> \Delta^*/e$.

Our experimental results on samples A, B and C allow us to examine which of the following device parameters might determine the R_{nl} characteristics: 1) the distance d between injector and detector 2) the resistance of the injector and detector contacts 3) the resistance-area product RA of the contacts, and 4) the RA asymmetry α between injector and detector. These parameters are summarized for each sample in Table 6.3. First, it is well established, both theoretically and experimentally, that all nonlocal subgap signals at low bias are reduced monotonically with d [7; 8; 9; 27]. Since the junction separation is largest in sample C, which exhibits the largest nonlocal signals, we conclude that in our samples d is not the crucial parameter and its effect is masked by the influence of another parameter. This is supported by the experimental finding that by changing d the characteristic shape of the R_{nl}-curve is not changed [8], whereas here the shape of the curves strongly change from sample A to C. Our results suggest that larger resistances of the injector and detector contacts suppress CAR and leave EC essentially unaffected, thus explaining our measurements at zero bias. However, Russo *et al.* [8] obtained similar results as those of sample C with larger junction areas ($4 \times 8\,\mu\mathrm{m}^2$) and much lower normal state contact resistances ($R_{\mathrm{N}} \sim 5\,\Omega$) [82]. If we use RA as the relevant parameter, Russo *et al.* measure $RA = 153.6\,\Omega\mu\mathrm{m}^2$ [82], thus being in the same range as sample C, see Table 6.3. This is remarkable since in [8] the geometry and materials are very different. Also a comparison with Beckmann *et al.* [10] shows similar nonlocal data for RA ($R_{\mathrm{i}}A_{\mathrm{i}} \approx 105\,\Omega\mu\mathrm{m}^2$ and $R_{\mathrm{d}}A_{\mathrm{d}} \approx 27\,\Omega\mu\mathrm{m}^2$ estimated from [10]) as sample B. In contrast to RA, we find no correlation between the RA asymmetry $\alpha = (R_{\mathrm{d}}A_{\mathrm{d}} - R_{\mathrm{i}}A_{\mathrm{i}})/(R_{\mathrm{d}}A_{\mathrm{d}} + R_{\mathrm{i}}A_{\mathrm{i}})$ and the systematic evolution of our data from sample A to C, see Table 6.3. Based on this discussion we conclude that the shape of the R_{nl} curves of our samples around zero bias is determined by RA.

We suggest a qualitative explanation for the contact resistance dependence of the subgap transport based on charging effects on the small contact capacitances known as dynamical Coulomb blockade (DCB) [47; 70], see chapter 3. Intuitively, CAR is suppressed because the transfer of a Cooper pair charge, $-2e$, to the superconductor is blocked by DCB. In contrast to CAR, no net charge is added to the superconductor for EC. Therefore EC is essentially unaffected by the blockade and dominates the subgap transport

for low transparencies around zero bias. Since for CI a net charge is transferred to the superconductor, the DCB picture is also consistent with the suppression of CI in low-transparent samples at zero bias (see sample C).

Are our samples in a regime where DCB can influence the charge transport across the NIS junctions? Generally, our tunneling contacts have a junction capacitance of $\sim 0.5\,\mathrm{fF}$ and a charging energy of $\sim 0.13\,\mathrm{meV}$. Thus, in principle, DCB effects are possible, see chapter 3. DCB depends strongly on the environmental impedance [70] and on the tunneling resistance, R_T, of the finite area contacts [66]. One usually expects DCB to become important for $R_\mathrm{T} > h/2e^2 \approx 12\,\mathrm{k}\Omega$ [70]. However, it was shown for finite area contacts that DCB can occur also for $R_\mathrm{T} < h/2e^2$ and that decreasing R_T leads to a reduction of the DCB effects [66].

RA is the natural parameter to characterize a finite area tunnel junction with many parallel channels. RA is inversely proportional to the mean transparency of a junction and scales with the average channel resistance ($RA \propto \rho_\mathrm{channel}$). A large number of weakly transmitting channels may lead to a small tunneling resistance while retaining DCB for each channel [66].

To model a real experiment it is not sufficient to describe the environment by only two lumped circuit elements, but by a transmission line [69]. On a sample different to A, B and C, we have measured a zero bias anomaly at base temperature with applied $H > H_\mathrm{C}$ as shown in Fig. 3.3. This decreased conductance around zero bias is due to DCB and can be modeled assuming an infinite LC transmission line with an external impedance $Z = 70\,\Omega$. As the calculations (see Fig. 3.3) show, the zero bias anomaly is small and already strongly thermally smeared at $T = 1.6\,\mathrm{K}$. As this device[5] exhibits a similar local and nonlocal behavior as sample B, we also expect DCB effects for sample A, B and C. Due to thermal smearing we do not see a zero bias anomaly in these devices at $1.6\,\mathrm{K}$.

As these charging effects depend on the environmental impedance and on the tunneling resistance, DCB varies in sample A, B and C due to their different injector and detector RA. The systematic change of the measured nonlocal resistance vs. bias characteristics in our samples as summarized in Fig. 6.8 can thus be understood as follows: the contacts of sample A have the lowest RA and thus the smallest contact charging, which allows CI and CAR to develop. For sample B with slightly larger injector and detector RA, DCB sets in and weakens CAR around zero bias relative to EC leading to a positive peak in nonlocal resistance. With resistances of a few kΩ (RA=117 and $365\,\Omega\mu\mathrm{m}^2$) as in sample C, DCB becomes strong and inhibits CAR relative to EC leading to a pronounced positive R_nl signal. Since charge is also transferred to the superconductor in case of CI, the DCB picture is also

---

[5]For the exact sample characterization we refer to junction N6 in chapter 6.5.

consistent with the suppression of CI in sample C at zero bias.

In the subgap regime we find a characteristic energy for sample B and C, namely the R_{nl}-minima at ± 0.135 meV in B and the R_{nl} sign change at $\sim \pm 0.13$ meV in C. The model of Levy Yeyati *et al.* [47] might explain these results as it qualitatively describes the measurements and therefore the sign reversal of the nonlocal signal in [8]. Due to DCB tunneling electrons excite electromagnetic modes which couple the injecting and detecting contact. Depending on whether the coupling is symmetric or antisymmetric, CAR or EC is the dominant subgap transport process. Since these symmetric and antisymmetric coupling modes have different frequencies, they dominate at different energies. Depending on which coupling mode is prominent at a certain energy, this decides whether CAR or EC dominates, hence explaining the crossover energy.

Another possible explanation brought up in [8; 10] is the phase-coherent motion of electrons in disordered metals. This introduces the Thouless energy $E_{\text{T}} = \hbar D/l_c^2$ as relevant energy scale with l_c as characteristic length of the sample and D as electron diffusion constant. In similar experiments but different geometry [8], the sign reversal of R_{nl} was suggested to be related to E_{T}. In our experiments E_{T} cannot be determined exactly. This is due to the fact that the injector-detector distance, the characteristic length scale l_c of our samples, cannot be determined unambiguously due to the spatial extend of the contacts. This allows distance variations for which we get E_{T} ranging from 0.05 meV to 0.29 meV. The characteristic energy measured in B and C could also be due to the charging energy of our junctions ($E_{\text{C}} \approx 0.13$ meV). For an applied bias $|U| > E_{\text{C}}/e$ the electrons have enough energy to overcome the Coulomb blockade and enter the superconductor. For these energies the blockade of CAR is lifted and R_{nl} can become negative. Nevertheless, as E_{C} and E_{T} are only estimates a final conclusion cannot be drawn.

For our results DCB gives an explanation for the successively increasing dominance of EC around zero bias with increasing RA of the contacts. However, our intuitive DCB picture cannot explain the appearance of negative R_{nl} values for low contact resistances and CAR as the dominant process. The exact origin is unclear. In most theoretical predictions CAR and EC cancel exactly or CAR is dominated by EC [12; 27; 36; 37; 40; 41; 43]. A possible explanation for the CAR dominated subgap transport in our measurements is given in the model of [47], which includes dynamical Coulomb blockade and electromagnetic coupling of the injector and detector junction. Currently, Levy Yeyati *et al.* are working on a simpler model including the contact resistances. This approach might reproduce our results. However, the contact resistance dependence of R_{nl} still remains an open theoretical problem.

In the following we discuss some additional results based on the presented data. In Fig. 6.5(c), 6.6(b) and 6.7(b) we characterize the injecting and detecting tunnel contact by bias-dependent differential conductance measurements and fitting to the BTK model including an additional broadening. As this is already discussed in chapter 5, we only briefly discuss the barrier characterization. All three devices exhibit a non-vanishing subgap conductance, which is even enhanced for A. This is most likely due to Andreev processes discussed in chapter 2.1. The considerable subgap conductance indicates weaker spots in the oxide barrier due to inhomogeneities in the insulating AlO_x layer. As device A and B exhibit in the normal state a metallic-like temperature dependence of the contact resistances R, we conclude pinhole-dominated transport. This is not surprising considering the short oxidation time for sample A and B (see chapter 5). Due to the longer oxidation time for sample C, it shows the smallest subgap conductance of the three samples and exhibits an insulating-like T-dependence of R, which indicates, following the Rowell criteria (see chapter 5.2), tunneling dominated transport. However, the inhomogeneities of all three barriers cannot consist of a too large portion of very high transparent regions since we still observe a tunneling characteristic in the superconducting state, namely a decrease of the zero bias conductance with lowering temperature. This is the case for sample A, B and C.

As discussed above, small RA are favorable for CAR dominated subgap transport. As a consequence only a small window of contact resistances is advantageous for a domination of CAR around zero bias. If the contacts resistances are very low (small RA), it was shown experimentally that EC and CI dominate the subgap transport [7; 9], whereas in low-transparent samples (large RA) EC dominates in the midgap regime (see sample C and [8]). In addition, samples in the strong tunneling regime only inject very small currents to the superconductor that only cause very small nonlocal signals easily out of the detection limit. Therefore the window for suitable contact resistances is small. As we learn from sample A and B, this resistance window is in the intermediate transparency regime, where the chance for pinholes and thus inhomogeneous current injection is large.

Since thinner insulating layers or pinholes result in higher current densities, this can lead to (local) heating and thus to changes of the superconducting properties. As the energy gap in the BTK fits and the critical temperature are not changed we conclude that this effect is not crucial. We further neglect inhomogeneous current paths as all nonlocal signals vanish above T_C, see chapter 6.3. In addition, we exhibit for sample A nearly no changes in the nonlocal behavior when swapping the injector and detector, see Fig. 6.5(a) and (b). Since current injection through pinholes and inhomogeneous current paths are dependent on the injecting contact, one would

expect a considerable change with a different injector. Experimentally this is not observed for sample A. However, in case these effects cause a spurious nonlocal signal, this signal will be positive (equivalent to EC and CI) and thus can not be mistaken as a dominant CAR process.

6.4.5 Summary and conclusion

By analyzing the sign and the temperature dependence of the nonlocal signals, we can distinguish CAR, EC and CI and identify them as competing subgap transport mechanisms in our four-terminal nonlocal measurements. We show that for small resistance area products CAR can dominate the nonlocal transport for all energies below the superconducting gap. In comparison with different devices we demonstrate a systematic change of the nonlocal resistance vs. bias characteristics with increasing RA. For samples with higher resistance area product, CAR is weakened relative to EC in the midgap regime. The reason why CAR is the dominant transport process (e.g. in sample A for all subgap biases) is unclear. Nevertheless, we qualitatively explain the suppression of CAR for higher RA by dynamical Coulomb blockade, which depends crucially on the RA. These findings add a new view to the understanding of the transport mechanisms in such devices. Our results show that for the detection of CAR it is more favorable to prepare devices with low RA values as higher RA most likely suppress CAR due to DCB. Only a small window of suitable RA values exists. If the RA of the contacts are too small, EC and CI dominate, whereas the nonlocal signals become vanishingly small for too large RA values.

6.5 Magnetic field dependence of crossed Andreev reflection and nonlocal charge imbalance

6.5.1 Introduction

In the last chapter we have reported that it is possible to have CAR as dominant transport process for all subgap energies. However, earlier experiments on these systems have shown that nonlocal CI masks CAR and EC in high-transparent samples. As we conclude from chapter 6.4 it is favorable to prepare NIS hybrid devices with lower junction resistances in order to minimize DCB effects suppressing CAR. With low RA junctions CI inevitably comes more into play, thus complicating the detection of CAR. Hence, further means to distinguish these processes are desirable. In this chapter we examine the behavior of nonlocal CI and CAR with an applied in-plane magnetic field and find a different dependence for both processes, thus providing a new tool to distinguish these processes. We further show

that the magnetic field behavior of CI can be understood by a generalization of the standard description of CI to nonlocal experiments.

6.5.2 Sample characterization

The sample preparation, characterization and the measurement setup are similar as discussed in chapter 4.5, 4.6 and 6.4.2. Here we only summarize important properties of the sample used for the presented data.

We discuss results of a $Pd(30\,nm)/AlO_x/Al(50\,nm)$ sample which we refer to as sample D. The tunneling barrier of sample D is prepared by oxidation in $0.1\,mbar$ oxygen atmosphere for $15\,min$ with cold substrate[6]. We characterize the Al by resistance measurements at $1.6\,K$ and obtain $\rho = 7.03\,\mu\Omega cm$, $D = 3.70 \cdot 10^{-3}\,m^2/s$, $\ell_{el} = 8.5\,nm$ and $\xi = 111\,nm$. Thus, Al is in the "dirty limit" of superconductivity. The edge-to-edge distances between the important contacts are $d_{45} = 105\,nm$, $d_{56} = 140\,nm$ and $d_{46} = 375\,nm$. As ξ is of the order of the edge-to-edge injector-detector distance d, we expect that it is possible to measure CAR and EC processes. Furthermore, we find a superconducting transition temperature $T_C \approx 1.3\,K$ and a critical magnetic field $H_C \approx 230\,mT$. We extract the latter from Fig. 6.9(b) and 6.10(c): In Fig. 6.9(b) we measure the resistance of the Al strip depending on an applied in-plane magnetic field at $0.24\,K$. Below the critical field H_C Al is superconducting, thus $R = 0$. For $H > H_C$ the Al strip becomes resistive as Al is normal conducting. In Fig. 6.9(b) the resistance starts rising at $160\,mT$ and saturates at $240\,mT$. We infer a more precise value of $H_C \approx 230\,mT$ from the zero bias R_{nl} vs. magnetic field measurements at base temperature shown in Fig. 6.10(c) and discussed in chapter 6.5.4.

6.5.3 Results

The results presented here are obtained on three junctions N4, N5 and N6 as shown in Fig. 6.9(a). For the nonlocal measurements we combine these contacts forming several different injector-detector pairs. In temperature dependent resistance measurements we find that all three tunnel junctions show metallic-like behavior with barrier resistance R and resistance area product RA given in Table 6.4 suggesting inhomogeneous tunneling barriers with pinholes. We further characterize the junctions by bias dependent differential conductance measurements, see Fig. 6.9(c). Junction N5 and N6 exhibit similar local transport behavior, whereas N4 shows more than fives times larger differential conductance values. All three barriers have in common that they exhibit a significant subgap conductance. The fitting to the

---

[6]At that time we were not able to measure the substrate temperature. We roughly estimate a temperature range of -10 to -40 °C.

BTK model as discussed in chapter 5.3 includes an additional broadening parameter. We use the barrier strength Z (given in Table 6.4) and a broadening parameter for fitting while keeping $\Delta = 0.19\,\text{meV}$ and $T = 0.24\,\text{K}$ constant. The parameter for the normal state resistance is only slightly adjusted for N4. We find acceptable agreement with the BTK model for energies below the gap Δ. For larger applied potentials the data are not well reproduced.

Before describing the data of our nonlocal measurements, we note that all injector-detector configurations show a very small, constant negative offset between -0.05 and -0.19 Ω in R_{nl} for $T > T_{\text{C}}$ and $H > H_{\text{C}}$. This might be either due to a small cross-talk effect or to a simple offset given by the amplifiers. However, the signals do not change upon doubling of the measurement frequency. For consistency, this offset is subtracted for all
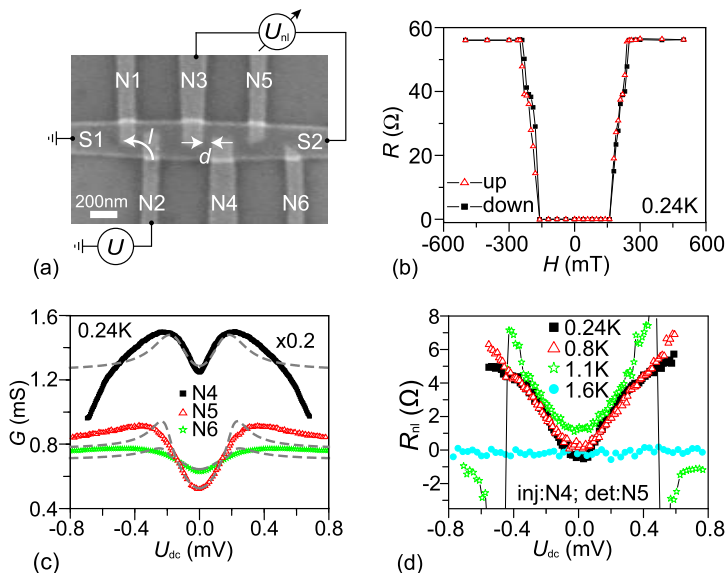

Figure 6.9: (a) SEM image of sample D with a schematic of the measurement. (b) Resistance of the Al strip vs. applied magnetic field at 0.24 K. The magnetic field is applied in the sample plane and parallel to the Al strip. (c) Differential junction conductance vs. bias for N4, N5 and N6 at 0.24 K. The gray dashed lines are fits to the BTK model with additional broadening. (d) Temperature dependent R_{nl} vs. bias measurements for N4 as injector and N5 as detector.

Table 6.4: Contact properties of sample D. R: normal state barrier resistance at 1.6 K; A: junction area; RA: normal state resistance area product at 1.6 K; Z: BTK barrier strength; $g_{NS} = G_{NS}/G_{NN}$: normalized tunneling conductance at zero bias and 1.1 K.

contact	R	A	RA	Z	g_{NS}
	[kΩ]	[μm^2]	[$\Omega\mu m^2$]		[@ 1.1 K]
N4	0.20	0.032	6.4	0.55	1.30
N5	1.28	0.021	26.9	0.77	0.95
N6	1.40	0.007	10.4	0.61	1.01

given R_{nl} values throughout this chapter.

Figure 6.9(d) and Fig. 6.10 focus on measurements with injector N4 and detector N5 where we study the temperature and magnetic field dependence of R_{nl}. In the subgap regime shown in Fig. 6.9(d) R_{nl} increases with T from negative values ($R_{nl} \approx -0.17\,\Omega$) at base T to positive values and vanishes above T_C for all biases. For bias voltages larger Δ/e the nonlocal resistance is positive. At 1.1 K and $U_{dc} \approx \pm 0.47$ mV R_{nl} abruptly turns negative and tends to zero for larger biases. In Figure 6.10(a) CI is generated with T close to T_C (see chapter 6.4). We exhibit that at 1.1 K the magnitude of R_{nl} decreases with increasing magnetic field for all biases. Close to H_C[7], at 115 mT, $R_{nl} = 0.4\,\Omega$ for $|U| < 100$ mV and approximately zero for larger bias. Above H_C all nonlocal signals vanish. At large bias we also observe an abrupt R_{nl} sign change that occurs at lower bias potentials with small applied in-plane magnetic field. In order to generate CI at base temperature we set in Fig. 6.10(b) a constant bias of $U_{dc} = 0.2$ mV (0.3 mV). We then study the magnetic field dependence of R_{nl}. The R_{nl} vs. H characteristics is similar for both biases as R_{nl} decreases with increasing H between 0-60 mT. R_{nl} stays constant at a positive value and starts increasing again for $U_{dc} = 0.2$ mV (0.3 mV) at $H \approx 180$ mT (150 mT). R_{nl} peaks at 203 mT (184 mT) and changes sign abruptly. Above 230 mT the nonlocal signals vanish. The temperature dependence of the R_{nl} vs. H characteristics at zero bias is shown in Fig. 6.10(c) and exhibits at 1.1 K a similar behavior as shown for finite bias (see Fig. 6.10(b)), namely a decrease of the positive R_{nl} with increasing magnetic field between 0 and 60 mT and a R_{nl} peak at 115 mT. For larger H-fields the nonlocal resistance is zero. The green, blue and violet lines are calculations based on a model discussed in chapter 6.5.4. At base temperature the R_{nl} vs. H behavior is different. We observe for $H < 200$ mT a constant negative R_{nl} of -0.19 Ω as indicated in Fig. 6.10(c) by the black dashed line. When increasing the magnetic field above 200 mT, R_{nl} increases, becomes positive, has a maximum at 230 mT and becomes

---

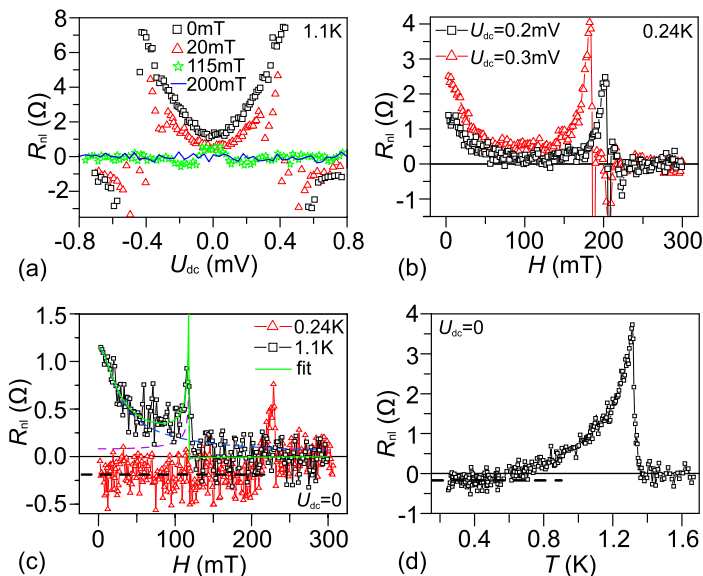[7]At 1.1 K the energy gap Δ is reduced and therefore H_C.

Figure 6.10: Magnetic field and temperature dependence of sample D with N4 as injector and N5 as detector. All magnetic fields are applied in-plane and parallel to the Al strip. For (b-d) a small negative R_{nl} offset was subtracted. (a) R_{nl} vs. bias for various magnetic fields at $1.1\,$K. (b) R_{nl} vs. H at $0.24\,$K at a fixed bias $U_{dc} = 0.2\,$mV and $0.3\,$mV. (c) Zero bias R_{nl} vs. H at $0.24\,$K and $1.1\,$K. The green line is a calculation based on a model described in chapter 6.5.4. In this context the blue dashed line displays a calculation with Δ=const and the violet one with τ_s=const. The black dashed line is a guide to the eye showing the constant negative R_{nl}. (d) Zero bias R_{nl} vs. T. The black dashed line again indicates the constant negative R_{nl}.

zero for larger H-fields. In R_{nl}-T measurements at zero bias we also observe in Fig. 6.10(d) a negative nonlocal resistance with $R_{nl} = -0.17\,\Omega$ for $T <$ $0.55\,$K. As already shown in Fig. 6.9(d), R_{nl} increases with T, changes sign at $0.6\,$K and peaks at $1.31\,$K. For higher T the nonlocal signal vanishes.

In Fig. 6.11 we study the R_{nl} vs. bias behavior for different T and for various applied in-plane magnetic fields in changed configuration, namely with N6 as injector and N5 as detector. In Fig. 6.11(a) this injector-detector (inj-det) configuration with $R_i A_i = 10.4\,\Omega\mu$m^2 and $R_d A_d = 26.9\,\Omega\mu$m^2 exhibits a very similar R_{nl} vs. bias characteristics as sample B (see Fig. 6.6)
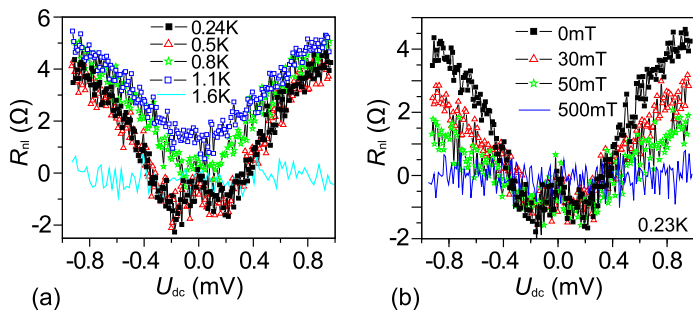
Figure 6.11: Nonlocal results of sample D with N6 as injector and N5 as detector. R_{nl} vs. bias for (a) different temperatures and (b) different in-plane magnetic fields parallel to the Al strip at $0.23\,\mathrm{K}$.

in chapter 6.4. At base T we observe in Fig. 6.11(a) a local maximum at $U_{dc} \approx 0$ with $R_{nl} \approx 0$ and at finite subgap bias $U_{dc} \approx \pm 0.18\,\mathrm{mV}$ two minima with negative nonlocal resistance of $\sim -1.3\,\Omega$. As in sample B the nonlocal signals are constant up to temperatures of $\sim 0.5\,\mathrm{K}$. With rising T above $0.5\,\mathrm{K}$ the negative R_{nl} changes sign and tends to larger positive values. At $T = 1.6\,\mathrm{K}$, i.e. for $T > T_C$, the nonlocal signal is zero for all bias. For voltages larger than $0.33\,\mathrm{mV}$, R_{nl} is positive at all T. The influence of a magnetic field applied in-plane at base temperature is studied in Fig. 6.11(b) and exhibits a bias dependence. For $|U| > 0.33\,\mathrm{mV}$, R_{nl} decreases with increasing magnetic field, whereas R_{nl} is not changing for $|U| < 0.33\,\mathrm{mV}$. At $500\,\mathrm{mT}$, i.e. above H_C, the nonlocal signals vanish for all bias voltages. Qualitatively, the temperature and magnetic field dependence of the R_{nl} vs. bias characteristics is similar in the swapped inj-det configuration with N5 as injector and N6 as detector (not shown).

6.5.4 Discussion

The barrier characterizations exhibit a behavior similar to sample A and B in chapter 6.4 and thus will be discussed only briefly. We conclude from the metallic-like temperature dependence of the normal state contact resistances of N4, N5 and N6 on the basis of the third Rowell criterion [78; 79] (see chapter 5.2) that the transport across the junction is dominated by pinholes or inhomogeneities in the tunneling distance. However, the portion of very high transparent regions is small, since we still observe a tunneling characteristics in the superconducting state, namely a reduction of the

zero bias conductance with decreasing temperature (not shown). The non-vanishing subgap conductance of N4, N5 and N6 is reflected in the fitting to the BTK model by rather low barrier strength values Z between 0.55 and 0.77, see Table 6.4. As we obtain reasonable fits for subgap energies by using Z and a broadening parameter as fitting parameters and leaving $T = 0.24\,\mathrm{K}$ and $\Delta = 0.19\,\mathrm{meV}$ fixed, we conclude to have a negligible shrinking of the superconducting energy gap. This is supported by the fact that in our samples T_C is not reduced, see Fig. 6.12(d). In contrast, similar devices with high-transparent junctions exhibit for Al a reduction of T_C to $0.6\,\mathrm{K}$ by the inverse proximity effect [9].

For the discussion of the nonlocal results we first need to identify the dominant processes for a given bias, temperature and magnetic field. In a second step we will discuss the influence of an applied magnetic field on the dominant nonlocal process for each inj-det pair. The identification of the predominant process is possible on the basis of chapter 6.2. The temperature dependence and the sign of R_nl are the indicators we use here, see Table 6.1. We have studied the inj-det pairs N4-N5 and N6-N5 in Fig. 6.9(d), 6.10 and 6.11. Regarding N4-N5, we observe in the subgap regime $R_\mathrm{nl} < 0$ at base temperature which tends to zero and becomes positive with rising T, see Fig. 6.9(d) and 6.10(d). Thus, we interpret CAR as being dominant around zero bias for $T < 0.6\,\mathrm{K}$, whereas CI dominates for higher T and generally for $|U_\mathrm{dc}| > \Delta/e$.

The temperature dependent R_nl vs. bias characteristics of inj-det N6-N5 (Fig. 6.11(a)) resembles sample B of chapter 6.4. Around zero bias CAR and EC approximately compensate each other at base temperature, whereas for finite subgap bias CAR dominates as reported in [8]. We attribute $R_\mathrm{nl} > 0$ at elevated temperatures ($T > 0.6\,\mathrm{K}$) to nonlocal CI. The same holds for $|U_\mathrm{dc}| > \Delta/e$.

As we have identified the relevant processes, we now discuss their magnetic field dependence and begin with nonlocal CI. Unlike CAR, it is possible to set the external parameters of a system in such a way that nonlocal CI is the dominant transport process. In Fig. 6.10(a-c) we use temperature and bias as parameters to let CI dominate the nonlocal transport and study its magnetic field dependence. In Fig. 6.10(a) and (c) we fix T close to T_C at $1.1\,\mathrm{K}$. Consequently, CI is the dominant subgap process for two reasons. On the one hand CAR and EC decrease with increasing T [47; 8] and on the other hand a thermally broadened Fermi distribution combined with a thermally shrinked energy gap allows more quasiparticles to be injected above the superconducting energy gap. To create CI at base temperature we fix in Fig. 6.10(b) the bias potential to energies larger than Δ which automatically leads to quasiparticle injection above the gap. As we can generate nonlocal CI, we will now discuss its magnetic field dependence. The

R_{nl} vs. H characteristics show that R_{nl} and thus CI decays on a magnetic field scale between 0 and $60\,\mathrm{mT}$, stays constant on a low level and increases again for magnetic fields close to H_{C}. This observation is similar for both, bias generated (Fig. 6.10(b)) and temperature generated (Fig. 6.10(c)) CI. We obtain equivalent results in the R_{nl} vs. bias measurements. For inj-det pair N4-N5 we see at $1.1\,\mathrm{K}$ a CI decrease with increasing H for all biases (Fig. 6.10(a)). At $115\,\mathrm{mT}$ we also observe small positive R_{nl} values around zero bias equivalent to the R_{nl} peak at $1.1\,\mathrm{K}$ in Fig. 6.10(c). As noticed in other inj-det pairs, N6-N5 exhibits for large bias a CI reduction with increasing H (Fig. 6.11(b)) . For subgap energies, however, we observe at base temperature a different behavior as it is related to CAR. This is discussed further below.

It is possible to model the magnetic field dependence of local CI. The connection to nonlocal CI is discussed in chapter 2.3. An applied magnetic field changes the CI relaxation time τ_{Q^*} and thus the CI length $\Lambda_{Q^*} = \sqrt{D\tau_{Q^*}}$. This is described on the basis of [48]. The charge imbalance relaxation time τ_{Q^*} indicates the decay time of CI within the superconductor and is given by [48]

$$\tau_{Q^*} = \frac{4k_{\mathrm{B}}T}{\pi\Delta(T,H)}\sqrt{\frac{\tau_E}{2\Gamma}} \qquad (6.1)$$

including inelastic scattering events via the corresponding time τ_E and spin-flip scattering and effects due to orbital pair breaking such as magnetic fields via τ_S. The latter is included in the parameter Γ given by

$$\Gamma = \frac{1}{\tau_S} + \frac{1}{2\tau_E} \qquad (6.2)$$

neglecting the effects due to spatial variation of the superconducting gap and due to pair breaking by the supercurrent. In [83] the magnetic field dependence of τ_S is given by

$$\tau_S(T,H) = \frac{\hbar}{\Delta(0,0)}\frac{H_{\mathrm{C}}^2(0)}{H^2}. \qquad (6.3)$$

With eq. (6.3) an increase in magnetic field enlarges Γ and consequently decreases the CI relaxation time τ_{Q^*}, thus describing our experimentally observed decay of nonlocal CI with magnetic fields. However, a decay is only described for small magnetic fields where changes in $\Delta(T,H) = \Delta(T)\left[1 - H^2/H_{\mathrm{C}}^2(T)\right]^{1/2}$ [83] are small too. Close to H_{C} the decrease of $\Delta(T,H)$ dominates eq. (6.1) and τ_{Q^*} increases. Again, this describes our experimental finding that R_{nl} and thus nonlocal CI increases close to H_{C} as seen in Fig. 6.10(b) at 184 and $203\,\mathrm{mT}$ and in Fig. 6.10(c) at 115 and $230\,\mathrm{mT}$.

This can intuitively be understood in such a way that a considerable decrease of Δ with increasing magnetic field allows more quasiparticle injection above the gap. This leads to the characteristic peaks at T_C and H_C in the T- and H-dependence. The R_{nl}-peaks close to H_C are temperature dependent and occur with higher temperatures at lower magnetic fields, see Fig. 6.10(c). At higher T the superconducting gap is already reduced resulting in a smaller H_C.

As we have an expression for the magnetic field dependence of τ_{Q^*} and Λ_{Q^*} (see eq. (6.1), (6.2) and (6.3)), we can now determine the magnetic field dependent nonlocal resistance with eq. (2.10). Thus, we obtain a zero-bias R_{nl} vs. H characteristics at 1.1 K shown as green line in Fig. 6.10(c). We use $T = 1.1\,\mathrm{K}$, $\Delta(0) = 0.19\,\mathrm{meV}$ and the experimentally obtained $g_{\mathrm{NS},2} = 0.95$ at 1.1 K. As injection volume Ω we assume the volume of the superconductor below the injecting contact and estimate $1.5 \cdot 10^{-21}\,\mathrm{m}^3$. We obtain an excellent agreement with the experimental result, see green line in Fig. 6.10(c), with the fitting parameters $\tau_E = 0.25\,\mathrm{ns}$ and $F^* = 0.05$. From this follows a charge imbalance length $\Lambda_{Q^*}(H = 0) = 1\,\mu\mathrm{m}$ at 1.1 K. As expected, $F^* << 1$ since the total current at zero bias is dominated by Andreev reflection. The relaxation time is considerably smaller than reported for thick ($\sim 12\,\mathrm{ns}$) and thin films ($\sim 4\,\mathrm{ns}$) [84], but consistent with the reduced charge imbalance length found in other experiments on superconducting Al wires [9; 10]. The reduction of τ_E for thin films was attributed to enhanced electron-electron scattering for films of thickness smaller than $\sqrt{\hbar D/k_{\mathrm{B}}T}$ [84], which we estimate to approximately 160 nm at $T = 1.1\,\mathrm{K}$ for our structures. We expect a similar additional suppression in thin wires. In addition to the R_{nl} vs. H fitting, Fig. 6.10(c) also shows the blue and the violet dashed line which are supposed to clarify the contribution of Δ and τ_S with changing H. Thus, we set either Δ=const (blue) or $\tau_S = \tau_S(H_C)$ =const (violet).

The finite bias experiments shown in Fig. 6.10(b) were performed at base temperature, which leads to a larger energy gap and a characteristic increase of CI at a larger magnetic field compared to Fig. 6.10(c). In addition, the finite supercurrent at an increased bias leads to a reduction of the energy gap and we expect a reduction of the QP relaxation time due to additional pair breaking. The latter effect is strong only for large currents near H_C, so that we can attribute the increase of R_{nl} with bias at $H = 0$ to a change of F^*: for a larger bias a larger fraction of the total current is generated by QP injection.

The magnetic field dependence of CAR is different to CI. In Fig. 6.10(c) and 6.11(b) we identify CAR as the dominant subgap transport mechanism at base temperature. The inj-det pair N4-N5 shows that CAR is not altered with magnetic fields up to 200 mT. With further increasing H the energy

gap shrinks and CI becomes dominant. A R_{nl} peak develops at H_C. The same holds for the inj-det pair N6-N5. The cancellation between CAR and EC around zero bias and the dominance of CAR at finite subgap bias is unchanged with magnetic fields up to 50 mT, see Fig. 6.11(b). Above H_C, at 500 mT, the signals vanish. As the cancellation between CAR and EC around zero bias does not change with magnetic field, we conclude that CAR *and* EC are robust with applied magnetic fields. This is in contrast to the results of Russo *et al.* [8] that show a weakening of CAR and EC with applied in-plane magnetic field. In [8] CAR and EC vanish already for H considerably smaller than H_C. Russo *et al.* argue that the magnetic field breaks the time reversal symmetry for the electron-hole wave injected into the superconductor. This is apparently not the case for our results. As the orientation of the magnetic field is similar, possible reasons for the different field dependence might be related to the varying coherence lengths in the materials used for the superconducting wire (Nb in case of [8]) and normal metal contacts or to the different sample geometries. The magnetic flux through the cross-sectional area of our superconducting Al wire is one flux quantum Φ_0 at 200 mT, the maximum H-field in which CAR and EC stay robust. To our knowledge there are no theoretical predictions on the behavior of CAR with parallel magnetic field. Our data shows that CAR and nonlocal CI have a different dependence on an applied magnetic field, which offers another possibility to distinguish these two processes. However, we note that in contrast to our experiments discussed in chapter 6.4, the out-of-phase part of the low-temperature signal in Fig. 6.10(c) has a similar amplitude as the in-phase signal, so that the results on the magnetic field dependence of CAR have to be considered as preliminary.

We attribute the abrupt R_{nl} sign change observed in Fig. 6.9(d) and Fig. 6.10(a) (and also in other samples not shown) to the onset of normal conductivity in the superconducting Al strip. It is important to note that in our experiments we identify the bias where this phenomenon appears. All our observations are well below this bias. Similar abrupt R_{nl} sign changes have been reported in [50] and were assigned to the critical current I_C and the transition between the superconducting and normal state. In our samples we consistently observe these sign changes for dc currents in the range between 2.3-2.7 μA. Moreover, we only see this effect at higher T. Since the energy gap is proportional to the critical current [85], elevated temperatures reduce $\Delta(T, H)$ and thus I_C. At base temperature the critical current of our Al strip is larger than 12 μA. Generally, the transition to the normal state does not happen homogeneously, but on a range of currents as the onset starts with a series of discrete, spatially localized dissipative regions, possibly related to phase-slip centers [83]. These might explain in Fig. 6.10(b) the additional smaller R_{nl} peaks above 184 and 203 mT, respectively.

6.5.5 Summary and conclusion

On a multi-terminal normal metal/insulator/superconductor device we have studied CAR and nonlocal CI with a special emphasis on the dependence on an applied in-plane magnetic field. On this sample we have used three contacts that show pinhole dominated transport, low BTK barrier strengths Z and resistance area product values comparable to those of sample A and B of chapter 6.4. For $T < 0.5\,\text{K}$ these junctions allowed in configuration N4-N5 to measure CAR dominated transport around zero bias (as sample A) and in configuration N6-N5 a similar nonlocal characteristics as sample B, namely $R_{\text{nl}} \approx 0$ at zero bias due to a cancellation of CAR and EC and $R_{\text{nl}} < 0$ at finite subgap bias due to CAR domination. We find CAR dominated subgap transport to be robust upon an applied in-plane magnetic field parallel to the superconducting Al strip up to magnetic fields close to H_{C}. This is in contrast to experimental results of [8] showing a decay of CAR and EC with applied in-plane magnetic field. The reason for this different result is unclear so far, but might be related to the different sample geometry or the superconducting material used.

We generated nonlocal CI either with temperatures close to T_{C} or with an applied bias and find that this process decays with increasing magnetic field in a range between 0 and $60\,\text{mT}$ for all biases. Above $\sim 60\,\text{mT}$ nonlocal CI is small and stays constant up to a magnetic field value close to H_{C}. In this magnetic field regime the superconducting energy gap decreases strongly with increasing magnetic field, thus allowing more quasiparticle tunneling across the junction leading to an increase of R_{nl}. The nonlocal resistance peaks at H_{C} and vanishes for $H > H_{\text{C}}$. As the transition between superconducting and normal state is not homogeneously, possible small R_{nl} fluctuations can happen even for magnetic fields slightly above H_{C} possibly due to phase-slip centers. The peak in R_{nl} is temperature dependent. At higher T the gap and thereby H_{C} is reduced, thus shifting the R_{nl} peak to lower H. The magnetic field dependence of CI is related to the charge imbalance relaxation time τ_{Q^*}, including inelastic scattering, but also spin-flip scattering and effects due to orbital pair breaking such as magnetic fields [48]. With the τ_{Q^*} vs. H characteristics we calculate the magnetic field dependence of R_{nl} on the basis of the "classical" local charge imbalance theory and extract a charge imbalance length $\Lambda_{Q^*}(H = 0) = 1\,\mu\text{m}$ consistent with literature. We find a very good agreement between theory and experimental results.

As nonlocal CI and CAR depend differently on applied magnetic fields, this gives another possibility to distinguish these two processes.

6.6 Contact resistance dependence of nonlocal charge imbalance

6.6.1 Introduction

As already explained in the introduction of chapter 6.5, we will focus in the following on nonlocal charge imbalance and study its dependence on the injecting and detecting contacts. Thus, we investigate the temperature- and bias-dependence of R_{nl} for various different injector-detector pairs. We find variations in the contact resistance dependence of nonlocal CI depending on the bias. In the low bias regime we show that it is possible to reproduce our results quantitatively with a new, recently published model.

The experiments were performed on the same sample using contacts N4, N5 and N6 as in chapter 6.5. Therefore, we refer for the sample and contact characterization to chapter 6.5 and begin directly with the presentation of our results.

6.6.2 Results

In the following our results deal with nonlocal charge imbalance measurements and study the nonlocal behavior for various injector-detector pairs. We focus on the three junctions N4, N5 and N6 and combine them to the six possible inj-det configurations. As N4, N5 and N6 have different barrier characteristics, this allows us to study the influence of the injector and detector contact resistance on nonlocal CI. When referring to an injector-detector pair, e.g. N4-N5, the first always refers to the injector and the second to the detector.

The U_{nl} vs. bias and R_{nl} vs. bias characteristics of all six inj-det pairs at 1.1 K are shown in Fig. 6.12(a) and (c), respectively. In both figures the nonlocal signals are positive for all pairs in the whole bias regime with a minimum value around zero bias. With increasing bias potential U_{nl} and R_{nl} enlarge. Those pairs with N4 as injector show an abrupt sign change at $U_{dc} \approx \pm 0.47$ mV as already observed in Fig. 6.9(d). In Fig. 6.12(a) and (c) it is peculiar that those pairs with the same injector exhibit very similar U_{nl} and R_{nl} vs. bias characteristics in the complete bias range. This holds best for N4 and N5 as injector. The characteristics of those pairs with injector N6, namely N6-N5 and N6-N4, are slightly different. For U_{nl} the curves of pairs with injector N4 do not coincide for any bias with those of other pairs,
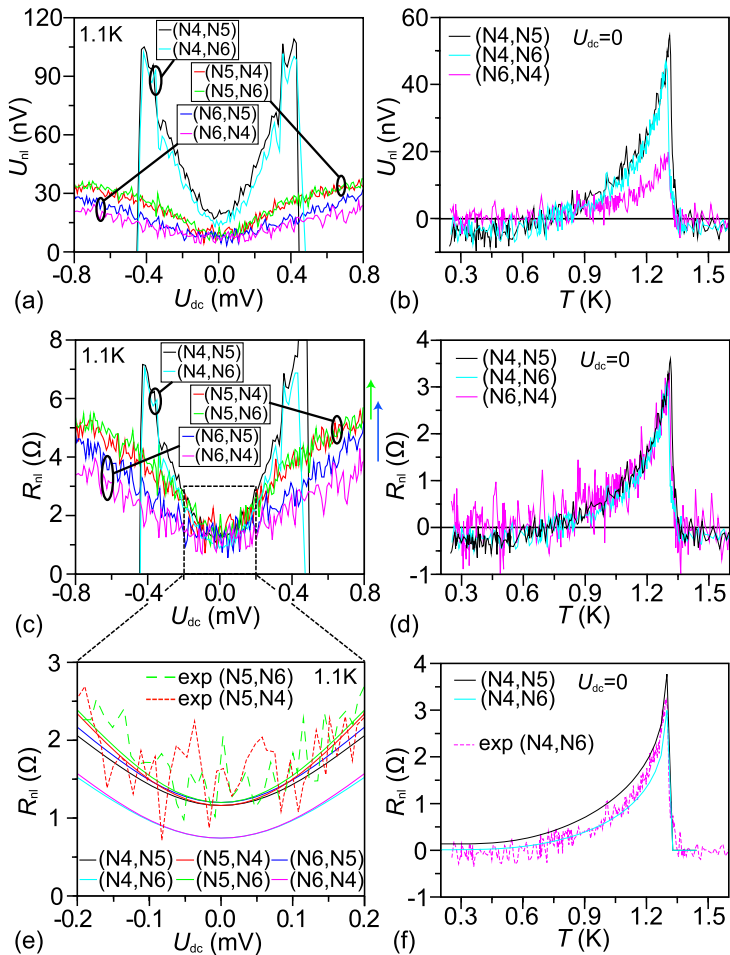
Figure 6.12: Results of sample D with various injector-detector pairs. (a) U_{nl} vs. bias at 1.1 K. (b) Zero bias U_{nl} vs. T. (c) R_{nl} vs. bias at 1.1 K. (d) Zero bias R_{nl} vs. T. (e+f) Calculations to (c+d) on the basis of [35] with $T_C = 1.3$ K, $\Delta = 0.197$ meV and a charge imbalance length $\Lambda^* = 1\,\mu$m for $T < T_C$ and $\Lambda^* = 0$ for $T > T_C$.

see Fig. 6.12(a). This is different for R_{nl} shown in Fig. 6.12(c) where the R_{nl} of all inj-det pairs coincide within the noise level approximately for all subgap biases. This is not the case for bias potentials larger than Δ/e.

To study further the dependence of the subgap characteristics on the contact resistances we measure U_{nl} and R_{nl} vs. temperature at zero bias for the pairs N4-N5, N4-N6 and N6-N4, see Fig. 6.12(b) and (d). At base temperature the nonlocal signals vanish (N6-N4) or are slightly negative (N4-N5 and N4-N6, see Fig. 6.10(d)). With rising T all nonlocal signals increase monotonically and peak at $T \approx 1.31\,\mathrm{K}$. For $T > 1.31\,\mathrm{K}$ all nonlocal signals are zero. For temperatures close to T_C N6-N4 clearly shows smaller U_{nl} values, see Fig 6.12(b), but exactly coincides with the R_{nl} vs. T characteristics of the other two inj-det pairs as shown in Fig 6.12(d). We have also observed this behavior in another sample not shown here.

6.6.3 Discussion

In order to study the contact resistance dependence of nonlocal charge imbalance, we measure the U_{nl} and R_{nl} vs. bias characteristics (Fig. 6.12(a) and (c)) close to T_C at $1.1\,\mathrm{K}$ to generate CI. As already discussed for inj-det pair N4-N5 and N6-N5 in chapter 6.5 (Fig.6.9(d) and Fig. 6.11(a)), CI is the dominant transport process for all biases at $1.1\,\mathrm{K}$. The same holds for all other inj-det pairs shown in Fig. 6.12, confirmed by T-dependent R_{nl} vs. bias measurements (T-dependence not shown).

Comparing the U_{nl} vs. bias characteristics of the various inj-det pairs, see Fig. 6.12(a), we find that U_{nl} is determined by the injecting and *not* by the detecting contact. This is best seen with N5 as injector and N4 and N6 as detector, respectively. Even though the contact resistances of N4 and N6 differ for all bias potentials by more than a factor of five, see Fig. 6.9(c) and Table 6.4, U_{nl} coincides at all biases for N5-N4 and N5-N6. The other pairs, namely N4-N5, N4-N6 and N6-N5, N6-N4, show a similar behavior. However, the pairs N4-N6 and N6-N4 exhibit slightly smaller nonlocal signals possibly due to the larger contact distance d.

While U_{nl} depends on the injector contact (Fig. 6.12(a)) at all biases, the R_{nl} vs. bias characteristics (Fig. 6.12(c)) exhibits a different behavior. For bias potentials larger than the energy gap we find the same dependence on the injector as is the case for U_{nl} of Fig. 6.12(a). Thus, with swapping the injector and detector contact of a pair with different conductances, e.g. N4 and N6, the injecting contact with the higher conductance leads to larger U_{nl} and R_{nl} values. For subgap energies, however, swapping the contacts of an inj-det pair does not change the nonlocal resistance. In this bias regime R_{nl} becomes the same for all contact pairs and thus seemingly independent of the contact resistances. This finding is in accordance with Fig. 6.12(d) where

at zero bias the R_{nl} of different inj-det pairs coincide for the CI dominated temperature regime close to T_{C}[8].

First we compare our data with the standard theory of CI described by eq. (2.10) and investigate the relative change between two curves. For the measurements with the same injector, F^* and the injection volume Ω are identical and we expect that only the distance between the contacts and the normalized conductance $g_{\mathrm{NS,det}}$ of the detector are relevant. As an example, using the experimentally determined $g_{\mathrm{NS,det}}$ at $T = 1.1\,\mathrm{K}$, see Table 6.4, and the CI length obtained in chapter 6.5, we expect a factor of ~ 1.3 between data points from the pairs N5-N4 and N5-N6 at the same bias. In Fig. 6.12(e) these two curves are replotted on a smaller scale. We obtain a factor 1.0 ± 0.3 between these two curves at zero bias. The standard deviation is even larger for the other pairs. We therefore conclude that the deviation from the standard description of CI is not significant due to the low signal-to-noise ratio. At higher bias the deviation from eq. (2.10) is more pronounced, as shown in Fig. 6.12(c), where the expected nonlocal resistance at $U_{\mathrm{dc}} = 0.8\,\mathrm{mV}$ is indicated by a green and a blue arrow for the pairs N5-N6 and N6-N5, based on the values of the pairs N5-N4 and N6-N4, respectively. However, in this regime an appreciable supercurrent is flowing in the device and we do not expect eq. (2.10) to hold exactly.

Swapping the injector and detector contacts allows one to compare signals independent of the contact distance. In this scheme, however, it is necessary to estimate F^* and the injection volume, each introducing considerable errors. For example, by assuming that F^* is similar for two contacts (e.g. for large bias $F^* \approx 1$) one finds a factor of ~ 3.5 between the curves with swapped contacts N4-N6 and N6-N4. This is not supported by our data, see Fig. 6.12(c). This consequently means that F^* varies between the contacts even at zero bias, see Fig. 6.12(d).

Our experimental results can be understood quantitatively by the model put forward in reference [35]. In a collaboration D. Golubev and A. Zaikin adapted their model slightly so that the experimentally determined junction parameters in Table 6.4 can be used. The nonlocal resistance of our device in terms of conductances reads

$$R_{\mathrm{nl}}(U_{\mathrm{dc}}) = \frac{G_{\mathrm{nl}}(U_{\mathrm{dc}})}{G_{\mathrm{det}}(0)G_{\mathrm{inj}}(U_{\mathrm{dc}}) - G_{\mathrm{nl}}^2(U_{\mathrm{dc}})}, \tag{6.4}$$

---

[8]The zero bias R_{nl}-T behavior of N6-N4 (Fig. 6.12(d)) is considerably more noisy, because the injected local current is smaller due to the higher contact resistance of N6.

where

$$G_\alpha(U_\alpha) = \frac{1}{R_\alpha} \int dE \frac{g_\alpha(E)}{4k_\mathrm{B}T \cosh^2 \frac{E - eU_\alpha}{2k_\mathrm{B}T}} \tag{6.5}$$

($\alpha = $inj, det) is the local conductance of the injector and detector and $g_\alpha(E)$ are the energy dependent spectral conductances of the NS barriers [26]:

$$\begin{aligned} g_\alpha(E) &= \frac{2\theta(\Delta - |E|)(1 + Z_\alpha^2)\Delta^2}{E^2 + (\Delta^2 - E^2)(1 + 2Z_\alpha^2)^2} \\ &+ \frac{2\theta(|E| - \Delta)(1 + Z_\alpha^2)|E|}{|E| + \sqrt{E^2 - \Delta^2}(1 + 2Z_\alpha^2)}. \end{aligned} \tag{6.6}$$

with θ the Heaviside function and Z_α the BTK barrier strength. The general expression for the nonlocal conductance $G_\mathrm{nl}(U_\mathrm{dc})$ is presented in reference [35]. Provided the charge imbalance length Λ_{Q^*} is shorter than the length of a superconducting wire (which is the case in our experiments), we find

$$\begin{aligned} G_\mathrm{nl}(U_\mathrm{dc}) &= \frac{1}{4e^2 NDSR_\mathrm{inj}R_\mathrm{det}} \\ &\times \int\limits_{|E|<\Delta} dE \frac{g_\mathrm{inj}(E)g_\mathrm{det}(E)}{4k_\mathrm{B}T \cosh^2 \frac{E - eU_\mathrm{dc}}{2k_\mathrm{B}T}} \frac{\Delta^2 - E^2}{\Delta^2} \frac{e^{-k(E)|x|}}{k(E)} \\ &+ \frac{\Lambda_{Q^*}e^{-|x|/\Lambda_{Q^*}}}{4e^2 NDSR_\mathrm{inj}R_\mathrm{det}} \\ &\times \int\limits_{|E|>\Delta} dE \frac{g_\mathrm{inj}(E)g_\mathrm{det}(E)}{4k_\mathrm{B}T \cosh^2 \frac{E - eU_\mathrm{dc}}{2k_\mathrm{B}T}} \frac{E^2 - \Delta^2}{E^2}, \end{aligned} \tag{6.7}$$

where $k(E) = \sqrt{2\sqrt{\Delta^2 - E^2}/D + 1/\Lambda_{Q^*}^2}$, N the density of states of the normal state Al, D the electron diffusion constant in Al and S is the superconducting wire cross-section. Note that at zero bias and in the limit $\Delta \ll k_\mathrm{B}T$, i.e. close to the critical temperature or the critical magnetic field, eq. (6.4) reduces to eq. (2.10) with $F^* = \Omega/2S\Lambda_{Q^*}$. One can see that for $G_\alpha \gg G_\mathrm{nl}$ the resistances of the NS barriers cancel out and do not enter the expression for the nonlocal resistance, which depends on the barrier properties only through the BTK parameters Z_α. Furthermore, in both limits of high and low temperatures also these factors drop out and one arrives at the following simple expressions for the nonlocal resistance

$$R_\mathrm{nl}(0) = \begin{cases} (r_{\Lambda_{Q^*}}/2)\, e^{-|x|/\Lambda_{Q^*}}, & T_\mathrm{C} - T \ll T_\mathrm{C}, \\ (r_\xi/2)\, e^{-|x|/\xi}, & k_\mathrm{B}T \ll \Delta, \end{cases} \tag{6.8}$$

where $r_{\Lambda_{Q^*}}$ and r_ξ are the normal state resistances of the superconducting wire segments of lengths Λ_{Q^*} and ξ, respectively. Thus, we find that the nonlocal resistance in these limits only depends on the distance between the junctions and the properties of the superconducting wire, but not on the properties of the NS barriers. This changes for $U > \Delta/e$ as CI generation becomes the main transport process across the junction. Then, the assumption $G_\alpha \gg G_{\mathrm{nl}}$ does not hold anymore for close enough contacts and the resistances of the NS barriers do not cancel out. This results in a nonlocal resistance not independent of the contact resistances.

In Fig. 6.12(e), numerically calculated R_{nl} curves based on the above equations are shown for $T = 1.1\,\mathrm{K}$, with material and contact characteristics from the experiments, including $\Lambda_{\mathrm{Q}*} = 1\,\mu\mathrm{m}$ from the magnetic field dependence. We stress that no fit parameters are used for these plots. We find that the calculations quantitatively reproduce our data. The two curves with larger contact separation (N4-N6 and N6-N4) exhibit a reduced nonlocal resistance compared to the other curves ($\sim 0.5\,\Omega$ smaller in (e)), which could not be resolved in the experiment. Figure 6.12(f) shows calculated temperature sweeps, which compare very well to the experimental curves. For this comparison we have subtracted a small constant from the data, because the model does not consider electron interactions and thus does not account for negative nonlocal resistance. In this model, the swapping of the injector and detector results in identical curves, also in agreement with our data.

6.6.4 Summary and conclusion

We have studied systematically the contact resistance dependence of nonlocal CI on six different inj-det pairs. We find that within the superconducting energy gap the nonlocal resistances of the various pairs are very similar even though the contact resistances differ. At large bias the R_{nl} curves are not identical and depend mainly on the injector resistance. To generate CI, we chose a rather high temperature at which the superconducting and the normal junction resistances differ only weakly. Thus, the curves display only small differences within the gap. For bias potentials larger than the energy gap an appreciable supercurrent is flowing. Therefore the "classical" CI theory of Tinkham [19; 52] does not hold exactly in this bias regime. However, our measurements suggest that around zero bias the contact resistances influence the nonlocal CI only weakly. This finding is reproduced in a theoretical model [35] adapted to incorporate experimentally accessible parameters. This model does not require additional parameters and agrees quantitatively with our data.

Chapter 7

Summary and outlook

We have used the angle-evaporation technique to prepare multi-terminal NIS hybrid devices with minimum contact distances of $\sim 50\,\mathrm{nm}$. On these samples we performed local measurements for junction characterizations and nonlocal measurements to study crossed Andreev reflection (CAR), elastic cotunneling (EC) and nonlocal charge imbalance (CI).

In nonlocal measurements we found that spurious effects like capacitive cross-talk, leakage currents or inhomogeneous currents paths can cause nonlocal signals in the detector possibly resembling expected nonlocal characteristics. Thus, we introduced criteria and control measurements for trustworthy nonlocal results.

For the detection of nonlocal processes we measured the nonlocal resistance R_{nl} as a function of bias, temperature T and applied magnetic field H. In our results we distinguished the competing nonlocal processes, namely crossed Andreev reflection, elastic cotunneling and nonlocal charge imbalance, by their sign of R_{nl} and by their T-dependence.

We find that in a small window of contact resistances CAR dominates the nonlocal subgap transport. This window is small as in the lower limit, namely in high-transparent samples, EC and CI dominate the transport at subgap energies as confirmed by theory and experiments [7; 9; 12]. Our results and [8] give the upper limit as they show that in low-transparent devices with resistance area products (RA) approximately larger than $100\,\Omega\mu\mathrm{m}^2$ EC dominates around zero bias.

Based on these findings we studied the contact resistance dependence of CAR on three different samples and find a successive change of the midgap R_{nl} characteristics with increasing injector and detector contact resistance.

Our results show that for low resistance area products (RA) and low temperatures $T < 0.5$ K CAR can dominate the nonlocal transport for all subgap biases, whereas for higher T and for bias potentials larger than the superconducting energy gap Δ nonlocal CI dominates. With increasing resistance area product CAR weakens and EC becomes prominent around zero bias. The contact resistance dependence of the subgap transport can qualitatively be understood based on charging effects on the small contact capacitances known as dynamical Coulomb blockade (DCB). However, the origin of the CAR dominance at low RA ($\sim 10 - 20\,\Omega\mu\text{m}^2$) remains unclear.

For a further understanding of the interplay between the competing nonlocal processes, we investigated their dependence of a magnetic field applied in-plane of the device. For $H << H_\text{C}$ CAR and EC are independent of the magnetic field. Close to H_C where the superconducting gap is strongly reduced, CI starts to dominate. CI, however, is already suppressed for low magnetic fields due to orbital pair breaking. We fit the CI results to the local CI theory and extract an inelastic quasiparticle relaxation time of 0.25 ns, considerably smaller as reported for thick and thin films, but in agreement with CI lengths obtained in recent experiments on superconducting Al wires in other groups. We attribute the reduced relaxation time to an enhanced electron-electron scattering. In contrast to CI, CAR is independent of H for low fields, which opens a novel possibility to distinguish these processes.

As we have studied the contact resistance dependence of CAR and EC, the same is necessary for nonlocal CI since a deeper understanding allows a better control over these processes. We find that for bias potentials larger than the superconducting energy gap the nonlocal resistance and thus nonlocal CI is determined by the injector and not the detector. This is in contrast to the "standard" theory of CI most likely due to an appreciable supercurrent flowing in the device in this bias regime. For subgap energies, however, different injector-detector pairs exhibit within noise similar nonlocal resistances. With a recently published theoretical model [35] it was possible to reproduce quantitatively this very weak dependence of nonlocal CI on the injecting and detecting contact resistance. In collaboration with D. Golubev and A. Zaikin we adapted this model in such a way that it only incorporates experimentally accessible parameters.

Tunnel contacts in the intermediate transparency regime are favorable for CAR dominated subgap transport. However, in this regime the barriers are most susceptible to inhomogeneities of the barrier strength. In future experiments an improved barrier preparation process is necessary to ensure more homogeneous and reproducible junctions. This might be achieved with longer oxidation times, lower temperatures and lower oxygen pressure. Concerning further studies on CAR, the next step is to understand our result on the magnetic field dependence of CAR and EC. Thus, applying mag-

netic fields from various directions might give further insights. In future experiments ferromagnetic contacts and a comparison with normal metal electrodes would be interesting as well. A new and different approach on investigating CAR and EC on multi-terminal devices are current-current correlations [86]. Besides such noise measurements further studies on DCB and its influence on lifting the balance between CAR and EC are needed in order to understand the origin of the CAR dominance. One approach could be different sample geometries which might influence the excited electromagnetic modes coupling the injector and detector [47] and thus change the nonlocal transport characteristics.

To sum up, this work demonstrated the dependence of crossed Andreev reflection on the contact resistance. This is an important finding as it gives a potential control on the nonlocal processes which is of high interest for the development of a solid-state entangler.

List of Figures

List of Tables

Bibliography

[1] G. E. Moore, Electronics **38**, 8 (1965).

[2] H. Buhrman, R. Cleve, and W. van Dam, SIAM J. Comput. **30**, 1829 (2001).

[3] G. B. Lesovik, T. MArtin, and G. Blatter, Eur. Phys. J. B **24**, 287 (2001).

[4] P. Recher, E. V. Sukhorukov, and D. Loss, Phys. Rev. B **63**, 165314 (2001).

[5] G. Deutscher and D. Feinberg, Appl. Phys. Lett. **76**, 487 (2000).

[6] J. M. Byers and M. E. Flatté, Phys. Rev. Lett. **74**, 306 (1995).

[7] D. Beckmann, H. B. Weber, and H. v. Löhneysen, Phys. Rev. Lett. **93**, 197003 (2004).

[8] S. Russo, M. Kroug, T. M. Klapwijk, and A. F. Morpurgo, Phys. Rev. Lett. **95**, 027002 (2005).

[9] P. Cadden-Zimansky and V. Chandrasekhar, Phys. Rev. Lett. **97**, 237003 (2006).

[10] D. Beckmann and H. v. Löhneysen, Appl. Phys. A **89**, 603 (2007).

[11] P. Cadden-Zimansky, J. Wei, and V. Chandrasekhar, Nature Phys. **5**, 393 (2009).

[12] M. S. Kalenkov and A. D. Zaikin, Phys. Rev. B **75**, 172503 (2007).

[13] W. Meissner and R. Ochsenfeld, Naturwissenschaften **21**, 787 (1933).

[14] H. K. Onnes, Leiden Comm. **120b, 122b, 124c** (1911).

[15] V. L. Ginzburg and L. D. Landau, Zh. Eksperim. i Teor. Fiz. **20**, 1064 (1950).

[16] J. Bardeen, L. N. Cooper, and J. R. Schrieffer, Phys. Rev. **108**, 1175 (1957).

[17] L. P. Gor'kov, Zh. Eksperim. i Teor. Fiz. **36**, 1918 (1959).

[18] L. N. Cooper, Phys. Rev. **104**, 1189 (1956).

[19] M. Tinkham, *Introduction to Superconductivity*, McGraw-Hill Book Co., New York, 2nd edition, 1996.

[20] W. Buckel and R. Kleiner, *Supraleitung: Grundlagen und Anwendungen*, WILEY-VCH Verlag GmbH & Co. KGaA, 6 edition, 2004.

[21] I. Giaever, Phys. Rev. Lett. **5**, 147 (1960).

[22] R. Meservey and P. M. Tedrow, Phys. Rep. **238**, 173 (1994).

[23] B. Pannetier and H. Courtois, J. Low Temp. Phys. **118**, 599 (2000).

[24] P. G. de Gennes, *Superconductivity of Metals and Alloys*, Addison-Wesley Publishing Company, Inc., 1966.

[25] T. M. Klapwijk, Journal of Superconductivity **17**, 593 (2004).

[26] G. E. Blonder, M. Tinkham, and T. M. Klapwijk, Phys. Rev. B **25**, 4515 (1982).

[27] G. Falci, D. Feinberg, and F. W. J. Hekking, Europhys. Lett. **54**, 255 (2001).

[28] D. Loss and D. P. DiVincenzo, Phys. Rev. A **57**, 120 (1998).

[29] G. Burkard, D. Loss, and E. V. Sukhorukov, Phys. Rev. B **61**, R16303 (2000).

[30] D. Loss and E. V. Sukhorukov, Phys Rev. Lett. **84**, 1035 (2000).

[31] A. Aspect, J. Dalibard, and G. Roger, Phys Rev. Lett. **49**, 1804 (1982).

[32] P. Recher and D. Loss, Phys. Rev. Lett. **91**, 267003 (2003).

[33] A. Galindo and M. A. Martin-Delgado, Rev. Mod. Phys. **74**, 347 (2002).

[34] N. Gisin, G. Ribordy, W. Tittel, and H. Zbinden, Rev. Mod. Phys. **74**, 145 (2002).

[35] D. S. Golubev, M. S. Kalenkov, and A. D. Zaikin, Phys. Rev. Lett. **103**, 067006 (2009).

[36] M. S. Kalenkov and A. D. Zaikin, Phys. Rev. B **76**, 224506 (2007).

[37] J. P. Morten, A. Brataas, and W. Belzig, Phys. Rev. B **74**, 214510 (2006).

[38] A. Brinkman and A. A. Golubov, Phys. Rev. B **74**, 214512 (2006).

[39] R. Mélin, F. S. Bergeret, and A. L. Yeyati, arXiv , 0811.3874v1 (2008).

[40] S. Duhot and R. Mélin, Phys. Rev. B **75**, 184531 (2007).

[41] D. S. Golubev and A. D. Zaikin, Phys.Rev. B **76**, 184510 (2007).

[42] G. Deutscher, Journal of Superconductivity **15**, 43 (2002).

[43] R. Mélin and D. Feinberg, Phys. Rev. B **70**, 174509 (2004).

[44] D. Feinberg, Eur. Phys. J. B **36**, 419 (2003).

[45] W. J. Herrera, A. L. Yeyati, and A. Martin-Rodero, Phys. Rev. B **79**, 014520 (2009).

[46] D. S. Golubev and A. D. Zaikin, Europhys. Lett. **86**, 37009 (2009).

[47] A. L. Yeyati, F. S. Bergeret, A. Martin-Rodero, and T. M. Klapwijk, Nature Phys. **3**, 455 (2007).

[48] A. Schmid and G. Schön, J. Low Temp. Phys. **20**, 207 (1975).

[49] J. Clarke, Phys. Rev. Lett. **28**, 1363 (1972).

[50] P. Cadden-Zimansky, Z. Jiang, and V. Chandrasekhar, New J. Phys. **9**, 116 (2007).

[51] M. Tinkham and J. Clarke, Phys. Rev. Lett. **28**, 1366 (1972).

[52] M. Tinkham, Phys. Rev. B **6**, 1747 (1972).

[53] J. Clarke, U. E. adn A. Schmid, G. Schön, and M. Tinkham, Phys. Rev. B **20**, 3933 (1979).

[54] R. E. Cavicchi and R. H. Silsbee, Phys. Rev. Lett. **52**, 1453 (1984).

[55] A. E. White, R. C. Dynes, and J. P. Garno, Phys. Rev. Lett. **56**, 532 (1986).

[56] J. Lambe and R. C. Jaklevic, Phys. Rev. Lett. **22**, 1371 (1969).

[57] T. A. Fulton and G. J. Dolan, Phys. Rev. Lett. **59**, 109 (1987).

[58] J. B. Barner and S. T. Ruggiero, Phys. Rev. Lett. **59**, 807 (1987).

[59] L. S. Kuzmin, P. Delsing, T. Claeson, and K. K. Likharev, Phys Rev. Lett. **62**, 2539 (1989).

[60] R. Wilkins, E. Ben-Jacob, and R. C. Jaklevic, Phys. Rev. Lett. **63**, 801 (1989).

[61] A. N. Cleland, J. M. Schmidt, and J. Clarke, Phys. Rev. Lett. **64**, 1565 (1990).

[62] P. Delsing, K. K. Likharev, L. S. Kuzmin, and T. Claeson, Phys. Rev. Lett. **63**, 1180 (1989).

[63] P. J. M. van Bentum, H. van Kempen, L. E. C. van de Leemput, and P. A. A. Teunissen, Phys. Rev. Lett. **60**, 369 (1988).

[64] S. Gregory, Phys. Rev. B **44**, 12868 (1991).

[65] A. N. Cleland, J. M. Schmidt, and J. Clarke, Phys. Rev. B **45**, 2950 (1992).

[66] P. Joyez, D. Esteve, and M. H. Devoret, Phys. Rev. Lett. **80**, 1956 (1998).

[67] E. Ben-Jacob, E. Mottola, and G. Schön, Phys. Rev. Lett. **22**, 2064 (1983).

[68] T.-L. Ho, Phys. Rev. Lett. **51**, 2060 (1983).

[69] G.-L. Ingold and Y. V. Nazarov, *Single Charge Tunneling*, chapter 2, pages 21–107, Plenum Press, New York, 1992.

[70] M. H. Devoret et al., Phys. Rev. Lett. **64**, 1824 (1990).

[71] S. M. Girvin, L. I. Glazman, M. Jonson, D. R. Penn, and M. D. Stiles, Phys. Rev. Lett. **64**, 3184 (1990).

[72] R. Waser, editor, *Nanoelectronics and Information Technology*, WILEY-VCH, 2003.

[73] CreaTec Fischer & Co. GmbH, *Manual of the Cold-Lip-Effusion-Cell CLC-40-10-200-SHP*.

[74] T. Heinzel, *Mesoscopic Electronics in Solid State Nanostructures*, WILEY-VCH GmbH & Co. KGaA, Weinheim, 2003.

[75] S. Oberholzer, *Fluctuation Phenomena in Low-Dimensional Conductors*, PhD thesis, University of Basel, 2001.

[76] H. Bluhm and K. A. Moler, Rev. Sci. Instrum. **79**, 014703 (2008).

[77] K. Montavon, B. Heimann, and M. Steinacher, in-house construction at the Department of Physics of the University of Basel.

[78] J. M. Rowell, *Tunneling Phenomena in Solids*, Plenum Press, New York, 1969.

[79] J. J. Akerman et al., J. Magn. Magn. Mater. **240**, 86 (2002).

[80] R. C. Dynes, V. Narayanamurti, and J. P. Garno, Phys Rev. Lett. **41**, 1509 (1978).

[81] B. Mitrovic and L. A. Rozema, J. Phys.: Condens. Matter **20**, 015215 (2008).

[82] S. Russo, *Crossed Andreev reflection and electron transport in ferromagnetic hybrid structures*, PhD thesis, Delft University of Technology, 2007.

[83] A. M. Kadin, W. J. Skocpol, and M. Tinkham, J. Low Temp. Phys. **33**, 481 (1978).

[84] M. Stuivinga, C. L. G. Ham, T. M. Klapwijk, and J. E. Mooij, J. Low Temp. Phys. **53**, 633 (1983).

[85] H. Ibach and H. Lüth, *Solid-State Physics*, Springer-Verlag, 2 edition, 1995.

[86] G. Bignon, M. Houzet, F. Pistolesi, and F. W. J. Hekking, Europhys. Lett. **67**, 110 (2004).

Appendix A

Capacitive cross-talk

In chapter 6.3 we discuss the influence of capacitive cross-talk on nonlocal signals in our devices. With lumped circuit elements it is possible to model this coupling as shown in Fig. A.1. In this simplified model the tunnel contacts of the injector and detector are represented by the tunneling resistance R_{T} and the junction capacitance in parallel. The lead resistances are labeled as R_{lead} and the resistances of the Al strip segments as R_{Al}. The capacitive coupling between consecutive leads and between leads or the Al strip and ground are represented by capacitances. As the leakage resistances are in the GΩ-regime, they are neglected here. Figure A.1 illustrates the local current I_{loc}, a mixture of a dc current with a small ac modulation, and an ac leakage current $I_{\mathrm{ac,leakage}}$ caused by capacitive cross-talk. The current is driven by a voltage on the injector and ideally does not pass by the detecting contact due to the $1\,\mathrm{G}\Omega$ input impedance at the detector. Leakage currents caused by capacitive coupling e.g. by the coupling to ground of the Al strip can pass by the detector, see Fig. A.1. This can cause classical phase-shifted "nonlocal" voltages. These "nonlocal" signals change with frequency ω because the capacitive impedance is given by $(i\omega C)^{-1}$. This model allows the simulation of these spurious nonlocal signals depending on the frequency and the capacitive coupling. However, it should be noted that simulations remain only an estimate as it is hard to include all details of capacitive cross-talk. Here, the model is simplified as, for example, it neglects the capacitive coupling of all measurement leads and all wires inside the cryostat to each other and to ground.
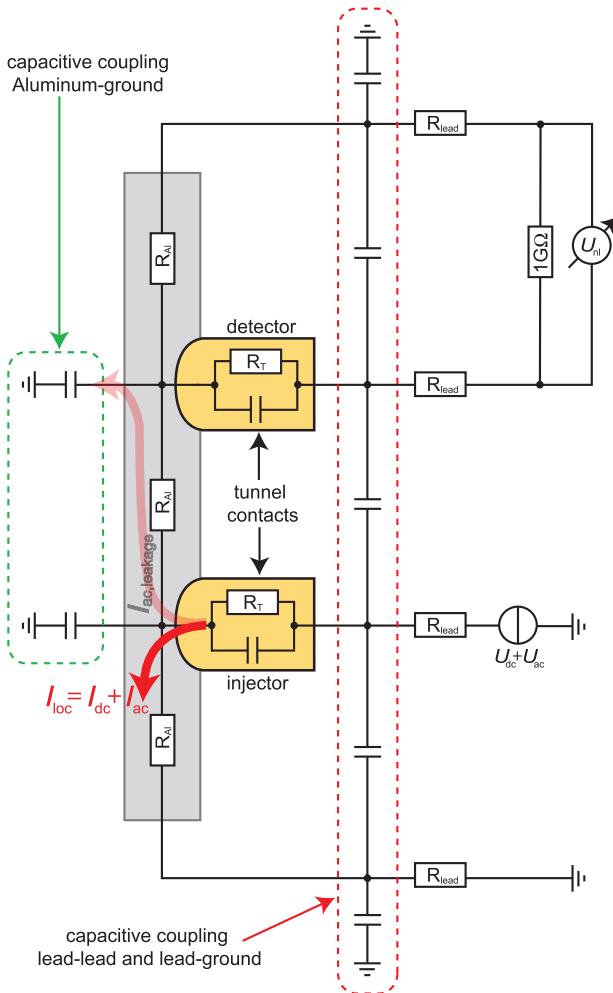
Figure A.1: A simplified model describing the capacitive coupling of a typical device and setup studied in this thesis. It illustrates exemplarily the possibility of ac leakage currents passing by the detector causing spurious nonlocal signals due to coupling between the Aluminum and ground.

Appendix B

Cleaning procedure for PBN crucibles

If liquid Al solidifies in a pyrolytic Bornitrid (PBN) crucible, the Al needs to be removed from the crucible for a possible reuse. At the beginning we kept the crucible for two weeks in a 20-50% sulfuric acid (H_2SO_4) in water solution with only little success. A better way turned out to be a 1 molar copper(II) chloride dihydrate ($CuCl_2 + 2H_2O$) in water solution with added 5% hydrochloric acid (HCl) in water. This solution is filled inside the crucible and exchanged every three hours. In an exothermic redox reaction Cu is reduced and Al oxidized at the Al surface. Al dissolves and Cu as leftover needs to be scratched away when exchanging the solution. In the possible case that even with a fresh solution the reaction is only weak, nitrohydrochloric acid (ratio 3:1 of HCl and HNO_3) accelerates the original reaction again. After 1-2 weeks the rest of the solidified Al piece is removable. Bathing the crucible in nitric acid (HNO_3) for 3 min removes remaining Cu leftovers. Inside the crucible a black thin layer remains which is resistive against several strong acids. We expect this film to be a form of aluminumoxid (AlO_x), which does not disturb when reusing the the crucible, because of its considerably higher melting and evaporating temperature. In a final cleaning step the crucible is bathed for 5 min in 35% hydrogen peroxide (H_2O_2), afterwards cleaned with demineralized water in an ultrasonic bath for 10 min and finally baked in an oven for 2 h at 200 °C. It is very important to check the crucible thoroughly with an optical microscope for possible cracks. In our experience these cleaning cycles can only be performed a limited number of times. Two crucibles broke in the third cleaning procedure. It is unclear if this was due to the cleaning or due to the mechanical stress which they were exposed to by uncontrolled cooling inside the effusion cell.

Publications

Articles

- *Electronic phase separation in $LaMnO_{3+\delta}$-layers: Usable as a tunneling barrier?*
  A. Kleine, Y. Luo and K. Samwer, Europhys. Lett. **76**, 135, (2006).

- *Contact resistance dependence of crossed Andreev reflection.*
  A. Kleine, A. Baumgartner, J. Trbovic and C. Schönenberger, Europhys. Lett. **78**, 27011 (2009).

- *Magnetic field and contact resistance dependence of non-local charge imbalance.*
  A. Kleine, A. Baumgartner, J. Trbovic, D.S. Golubev, A.D. Zaikin and C. Schönenberger, accepted in Nanotechnology.

Poster contributions

- *Properties of thin $LaMnO_3$ layers and its characterization as a tunneling barrier.*
  A. Kleine, Y. Luo and K. Samwer.
  Poster at the annual meeting of the Deutsche Physikalische Gesellschaft (DPG), Berlin, Germany, March 4th - 9th, 2005.

- *Non-local measurements on normal metal - superconductor hybrid structures: the quest for crossed Andreev reflection.*
  A. Kleine, J. Trbovic and C. Schönenberger.
  Poster at the International Workshop "Frontiers in Nanoscale Science and Technology" FNST 2008, Basel, January 6th - 8th, 2008.

- *Non-local measurements on normal metal - superconductor hybrid structures: the quest for crossed Andreev reflection.*

A. Kleine, J. Trbovic and C. Schönenberger.
Poster at the annual meeting of the Swiss Physical Society, Geneva, March 26th - 27th, 2008.

- *Non-local measurements on normal metal - superconductor hybrid structures: the quest for crossed Andreev reflection.*
  A. Kleine, J. Trbovic and C. Schönenberger.
  Poster at the NCCR Review meeting, Basel, April 14th, 2008.

- *Non-local measurements on normal metal - superconductor hybrid structures: the quest for crossed Andreev reflection.*
  A. Kleine, J. Trbovic and C. Schönenberger.
  Poster at the International Workshop "Global Challenges and How Nanotechnology can help", San Servolo, Italy, April 21th - 24th, 2008.

- *Crossed Andreev reflection dominated subgap transport in normal metal / superconductor hybrid structures.*
  A. Kleine, A. Baumgartner, J. Trbovic and C. Schönenberger.
  Poster at the 420. International WE-Heraeus-Workshop "Unconventional Proximity Effects in Novel Materials", Bad Honnef, Germany, October 13th - 15th, 2008.

Talks

- *Properties of thin $LaMnO_3$-layers and its characterization as a tunneling barrier.*
  Talk at the DFG project meeting, Göttingen, Germany, 2004.

- *Strukturelle und magnetische Untersuchungen an LMO-Einzellagen und LCMO/LMO-Multilagen.*
  Talk at the DFG project meeting, Konstanz, Germany, 2004.

- *The quest for a solid-state entangler.*
  Talk at the International Workshop "Global Challenges and How Nanotechnology can help", San Servolo, Italy, April 21th - 24th, 2008.

- *Contact resistance dependence of crossed Andreev reflection.*
  Talk at the Swiss Nano 2009 conference, Basel, June 11th - 12th, 2009.

Awards

- Poster award of the 420. International WE-Heraeus-Workshop "Unconventional Proximity Effects in Novel Materials", Bad Honnef, Germany, October 13th - 15th, 2008.

Curriculum vitae

Andreas Kleine

- January 5 1979
  born in Bremen, Germany

- 1991-1998
  Cato Bontjes van Beek-Gymnasium Achim, Germany, "Abitur"

- 1998-1999
  Civil service as paramedic at DRK Achim, Germany

- 1999-2001
  University of Göttingen, Germany, "Vordiplom" in physics

- 2001-2002
  University of California, San Diego, USA
  Scholarship of the Education Abroad Program (EAP)

- 2002-2005
  University of Göttingen, Germany, "Diplom" in physics

- 2004-2005
  Diploma thesis with Prof. K. Samwer
  Thesis title: *"Herstellung und Eigenschaften dünner LaMnO$_3$-Schichten und ihre Charakterisierung als Tunnelbarriere"*

- 2005-2009
  University of Basel, Switzerland
  PhD studies in experimental physics with Prof. C. Schönenberger
  Thesis title: *"Experiments on nonlocal processes in NS devices"*

- since 2003
  Teaching assistant for several lectures and lab courses

For valuable lectures and experimental guidance during my studies I am indebted to:

W. Felsch, H. C. Freyhardt, G. C. Hegerfeldt, F. Hellman, J. Hirsch, C. Hofsäss, C. Jooss, I. Kersten, H.-U. Krebs, Y. Luo, V. Meden, M. Münzenberg, K.-H. Rehren, A. Rizzi, H. W. Roesky, K. Samwer, C. Schönenberger, L. Sham, T. tom Dieck, R. G. Ulbrich, K. Winzer and A. Zippelius

Acknowledgements

I am indebted to many people as they have supported me with this work over the last years. Without them this thesis would have looked different.

First I want to express my gratitude to Christian Schönenberger, who gave me the chance to work with him and his group. With his great knowledge of physical processes and experimental setups he helped me many times! I am very grateful to have profited from this knowledge but also from his way of organizing the very well-run group. It is amazing to see how he always finds time to discuss results.

In the last two years of my thesis Andreas Baumgartner was in every respect of great help to me. With his experimental experience, his knowledge of physics and his love to find things out the project gained a lot! Not only that I learned a lot from him, but it was also great fun working together!

Moreover I would like to thank Jelena Trbovic for supporting me mainly during my first two years where we set up the cryostat and started the new project.

I am very glad and grateful that I shared the office over the time with Alexander Eichler, Lukas Hofstetter, Hagen Aurich, Frank Freitag, Oren Knopfmacher, Szabolcs Csonka, Dino Keller and Jürg Furer. I really enjoyed the lively atmosphere with all the scientific and non-scientific discussions. Surely, also the other group members and visitors, namely Michel Calame, Markus Weiss, Wangyang Fu, Jon Agustsson, Toni Fröhlich, Alexey Tarasov, Jan Brunner, Erasmus Bieri, Gunnar Gunnarsson, Sense Jan van der Molen, Zheng-Ming Wu, Songmei Wu, Jianhui Liao, Teresa Gonzalez, Matthias Gräber, Laetitia Bernard, Stefan Oberholzer, Attila Geresdi, Peter Makk and Haichao Huang helped and made my time very enjoyable!

Besides Christian Schönenberger, Alberto Morpurgo and Hilbert von Löhn-

eysen were members of my committee. I want to thank them for spending their precious time with reading my thesis and coming to Basel for my defense.

As I performed experiments I acknowledge the help and advice from Michael Steinacher and Sascha Martin and their teams from the the electronic and mechanical workshop. Dominik Sifrig made the low temperature measurements possible as he provided us very reliably with liquid Helium.

My special gratitude goes to Daniel Sacker with whom I set up the new BesTec evaporator and kept it running over the last years.

I also like to thank our secretaries Barbara Kammermann and Astrid Kalt who were always very helpful and who were great guides through the administrative jungle.

Furthermore, I acknowledge the good collaboration with Dimitri Golubev and Andrei Zaikin and the fruitful scientific discussions with Christoph Bruder, Alexis Baratoff and Alfredo Levy Yeyati.

I am very much indebted to my family who supported me in every respect through all the different stages of my education. They made a lot of things possible. Thank you!

Last, but certainly not least I am deeply grateful to Vali, who had to suffer a lot during the last months of my PhD. She coped very well with my moods and my lack of time. I am very glad for her tremendous support and understanding!